nature neuroscience

Article

https://doi.org/10.1038/s41593-025-01872-y

Brain pericytes and perivascular fibroblasts are stromal progenitors with dual functions in cerebrovascular regeneration after stroke

Received: 14 January 2022

Accepted: 18 December 2024

Published online: 17 February 2025

Check for updates

Louis-Philippe Bernier[1,6] ✉, Jasmin K. Hefendehl[1,2,6], R. Wilder Scott[3,4], Lin Wei Tung[3], Coral-Ann Lewis[3], Hesham Soliman[3], Stefan Simm[5], Lasse Dissing-Olesen[1], Jan Hofmann[2], David Guo[3], Murphy DeMeglio[2], Fabio M. Rossi[3], T. Michael Underhill[3,4] & Brian A. MacVicar[1] ✉

Functional revascularization is key to stroke recovery and requires remodeling and regeneration of blood vessels around which is located the brain's only stromal compartment. Stromal progenitor cells (SPCs) are critical for tissue regeneration following injury in many organs, yet their identity in the brain remains elusive. Here we show that the perivascular niche of brain SPCs includes pericytes, venular smooth muscle cells and perivascular fibroblasts that together help cerebral microvasculature regenerate following experimental stroke. Ischemic injury triggers amplification of pericytes and perivascular fibroblasts in the infarct region where they associate with endothelial cells inside a reactive astrocyte border. Fate-tracking of *Hic1*$^{+}$ SPCs uncovered a transient functional and transcriptional phenotype of stroke-activated pericytes and perivascular fibroblasts. Both populations of these cells remained segregated, displaying distinct angiogenic and fibrogenic profiles. Therefore, pericytes and perivascular fibroblasts are distinct subpopulations of SPCs in the adult brain that coordinate revascularization and scar formation after injury.

Stroke is a leading cause of death and morbidity worldwide, with current therapeutic interventions mostly limited to acute thrombolytic treatment or thrombectomy, followed by long-term rehabilitation. Improving the brain's somewhat limited post-stroke repair mechanisms is an untapped therapeutic opportunity and is therefore of particular research interest[1,2]. The end objective, to promote functional recovery of the neural parenchyma, may involve endogenous neuronal plasticity, neurogenesis, and even exogenous stem cell-based therapies. Extensive research on brain repair has described the existence and activation of neural precursor cells following stroke[3–5]. However, the reestablishment of an adequate blood supply via post-ischemic revascularization and angiogenesis remains a major hurdle for neuronal implantation, survival and proper function in affected areas[6–8]. Along with proliferation of lumen-forming endothelial cells (ECs) and mobilization of endothelial precursor cells, angiogenesis implicates cell–cell communication with pericytes, extensive extracellular matrix (ECM) remodeling and basal lamina formation[9,10]. In the brain, connective tissue (stroma) is limited to the perivascular basal lamina, and cells lying within the basal lamina that play critical roles in the generation of a functional blood–brain barrier (BBB). Hence, the importance of stromal regeneration is

[1]University of British Columbia, Djavad Mowafaghian Centre for Brain Health, Vancouver, British Colombia, Canada. [2]Goethe University Frankfurt, Institute for Cell biology and Neuroscience, Buchmann Institute for Molecular Life Sciences, Frankfurt am Main, Germany. [3]University of British Columbia, Biomedical Research Centre, Vancouver, British Colombia, Canada. [4]Dept. of Cellular and Physiological Sciences, University of British Columbia, Vancouver, British Colombia, Canada. [5]University Medicine Greifswald, Institute for Bioinformatics, Greifswald, Germany. [6]These authors contributed equally: Louis-Philippe Bernier, Jasmin K. Hefendehl. ✉e-mail: lp.bernier@ubc.ca; bmacvicar@brain.ubc.ca

amplified in the CNS and a better understanding of the mechanisms governing regeneration of the stromal vascular compartment in the brain after injury is therefore imperative.

A subset of perivascular cells is believed to proliferate and promote the regeneration of stromal tissue following injury[11–16]. These populations form a functional grouping broadly termed stromal/mesenchymal progenitor cells (SPCs) due to their stromal location, expression of mesenchymal markers and ability to differentiate into various mesenchymal lineages[11,17–24]. In most organs, these populations mobilize after damage and coordinate tissue regeneration to provide trophic and structural support for subsequent reestablishment of parenchymal cells. The cellular identities within SPC populations are organ dependent, and may include fibroadipogenic progenitors, skeletogenic progenitors, fibroblasts and pericytes[14,15,17,25,26]. Our group recently showed that the hypermethylated in cancer 1 (*Hic1*) transcriptional repressor gene specifically marks and regulates the quiescence of SPC populations in skeletal muscle, heart and skin[14,15]. Lineage tracing of *Hic1*$^+$ SPCs and their progeny enabled the characterization of a complex tissue regenerative process, with subsets of SPCs of various cellular identities contributing to transient populations that supported functional tissue regeneration or stable fibrogenic scar formation[14,15]. However, in the CNS, where stromal tissue is limited to the vascular basement membrane and stromal regeneration is tightly intertwined with revascularization, the identity of brain-resident stromal precursor cells has remained elusive.

Multiple lines of evidence suggest brain pericytes share functional similarities with SPCs such as their stromal location and their in vitro differentiation potential[11,27–29]. Pericytes line cerebral vessels and exhibit discrete morphologies depending on their location along the arterio–capillary–venule axis[30–33]. Resting pericytes maintain BBB integrity and participate in the control of hemodynamic responses, among other vital functions[28,34–38]. During development, pericytes play an essential role in angiogenesis where they stabilize newly formed vessels and contribute to BBB formation[28,37,39]. Importantly, recent evidence describes a tight synchrony between pericytes and ECs in neonatal vascular development, with capillary angiogenesis originating from the venular side of the arterio–venular axis[40]. Following ischemic injury, it was recently shown that transplanting pericyte-like cells derived from human pluripotent stem cells improves recovery and that higher abundance of pericytes correlates with BBB restoration and revascularization[41–43].

Despite their angiogenic function during brain development and their potential to drive post-injury revascularization, recent studies have mainly suggested that pericytes drive scar formation after injury in the adult brain. For example, type A pericytes (defined in refs. 13,44 by their perivascular location and expression of glutamate aspartate transporter (GLAST)), type 1 pericytes (nestin$^-$/NG2$^+$) and PDGFRβ-expressing pericytes have been described as mainly fibrogenic after trauma[13,44–51]. However, the response of pericytes and other SPCs to trauma is unclear because their identification relies on a combination of morphology, location and expression of markers that are both nonspecific and transiently modulated by injury[52].

For example, recent data show that perivascular fibroblasts form a distinct collagen-expressing cell population, even though they share a perivascular location and several markers with pericytes[26,53,54]. Although fibroblasts are key players in the fibrogenic response in many organs through deposition of ECM components[55], the roles for brain-resident perivascular fibroblasts after stroke are unknown. CNS fibrosis may be beneficial (by maintaining structural integrity and limiting damage-induced necrosis); however, it may also be detrimental by inhibiting neuronal regeneration[56,57]. Regeneration following cerebrovascular damage likely relies on a balance between angiogenic and fibrogenic activity. It is therefore critical to define SPC populations in the CNS and to delineate their respective functions after injury.

Here, we describe the expression pattern of *Hic1* in the adult mouse brain and by tracking *Hic1*$^+$ cells and their progeny after stroke, we identify pericytes, venular smooth muscle cells (SMCs) and perivascular fibroblasts as the brain-resident *Hic1*$^+$ SPC subpopulations. Using transgenic tools to differentiate these three populations, we characterize their coordinated responses to ischemic injury and their respective contributions to post-stroke cerebrovascular regeneration. Our results demonstrate that bona fide pericytes undergo functional and transcriptional activation into a transient angiogenic profile that is distinct from the fibrotic program driven by perivascular fibroblasts. Revascularization represents a crucial step for parenchymal recovery in the injured CNS. Understanding the mechanisms governing the contribution of brain SPCs to the regeneration of cerebral blood vessels may be key to harnessing the brain's regenerative potential.

Results

Post-stroke revascularization and accumulation of *Hic1* lineage cells

To investigate the involvement of SPCs and their relation to functional revascularization in the brain following vascular injury, we first subjected adult mice to cortical photothrombotic stroke in the hindlimb region of the somatosensory cortex (Extended Data Fig. 1a). This experimental stroke model induced permanent blockade of blood flow with clear delineation between stroke core and unaffected tissue (Fig. 1a and Extended Data Fig. 1b). Continued observations for 21 days showed remarkable regeneration of the cerebrovasculature within the ischemic region (Fig. 1b,c and Extended Data Fig. 1c,d). Progressive revascularization and vascular reorganization were observed throughout the 21-day recovery process via longitudinal in vivo variance-based optical coherence tomography (OCT) angiography (Fig. 1b,c and Extended Data Fig. 1d). Reappearance of functional vessels was also seen when comparing cortical vascular beds in mice imaged using in vivo two-photon microscopy on either day 1 or day 21 after stroke (Extended Data Fig. 1e). The appearance of a revascularized, functional capillary bed was first observed around the rim of the lesioned area 1 week following stroke, which then progressed into the ischemic core over time, revealing a migrating zone of active angiogenesis (Fig. 1b,c and Extended Data Fig. 1d).

To investigate the identity and function of the brain stromal/mesenchymal precursor populations participating in the stromal regeneration and revascularization observed here, we hypothesized that *Hic1*, a transcriptional repressor shown to specifically mark mesenchymal progenitor populations in skeletal muscle, heart and skin[14,15,58], would also label SPCs in the CNS. We first assessed the presence and location of *Hic1*-expressing cells in the brain using a *Hic1* reporter mouse (*Hic1*$^{nLacZ/+}$). After X-gal staining, we observed *Hic1*-expressing cells

Fig. 1 | Post-stroke revascularization spatiotemporally correlates with *Hic1*-tdTomato$^+$ cell accumulation. a, 2,3,5-triphenyltetrazolium chloride (TTC) staining of the ischemic area 24 h following photothrombotic stroke. **b**, Optical coherence tomography (longitudinal imaging after stroke at indicated time points) showing partial functional revascularization of the ischemic area 7–21 days following stroke. **c**, Quantification of the size of the ischemic area over time following stroke, from images obtained with OCT imaging. Mean values are represented by the red line. **d**, In adult *Hic1*$^{nLacZ/+}$ mice, expression of LacZ is restricted to perivascular cells within the stromal compartment. *Hic1*-LacZ$^+$ nuclei are found within the laminin$^+$ basement membrane. **e**, Stroke induces accumulation of *Hic1*-LacZ$^+$ cells within the lesioned area, 7 days after injury. **f**, Following stroke, death of *Hic1*-tdTomato$^+$ cells is observed at 24 h. At days 7–21, intense accumulation of *Hic1*-tdTomato$^+$ cells (arrow) is observed within the ischemic lesion area. **g**, Quantification of *Hic1*-tdTomato$^+$ cell accumulation at days 1, 7 and 21 after stroke relative to the distance from the ischemic core center (ROI 1 to 3). tdTomato fluorescence intensity in each ROI was compared to an equivalent contralateral ROI from the same brain slice and shown as fold change (*$P < 0.05$; **$P < 0.01$; ***$P < 0.001$).

https://doi.org/10.1038/s41593-025-01872-y

in a perivascular location embedded within the laminin$^+$ basement membrane, therefore within the stromal compartment (Fig. 1d). When *Hic1*-LacZ mice were subjected to photothrombotic stroke, accumulations of *Hic1*$^+$ cells were observed in and around the lesion core 7 days following stroke (Fig. 1e), indicative of *Hic1*$^+$ cell expansion after stroke.

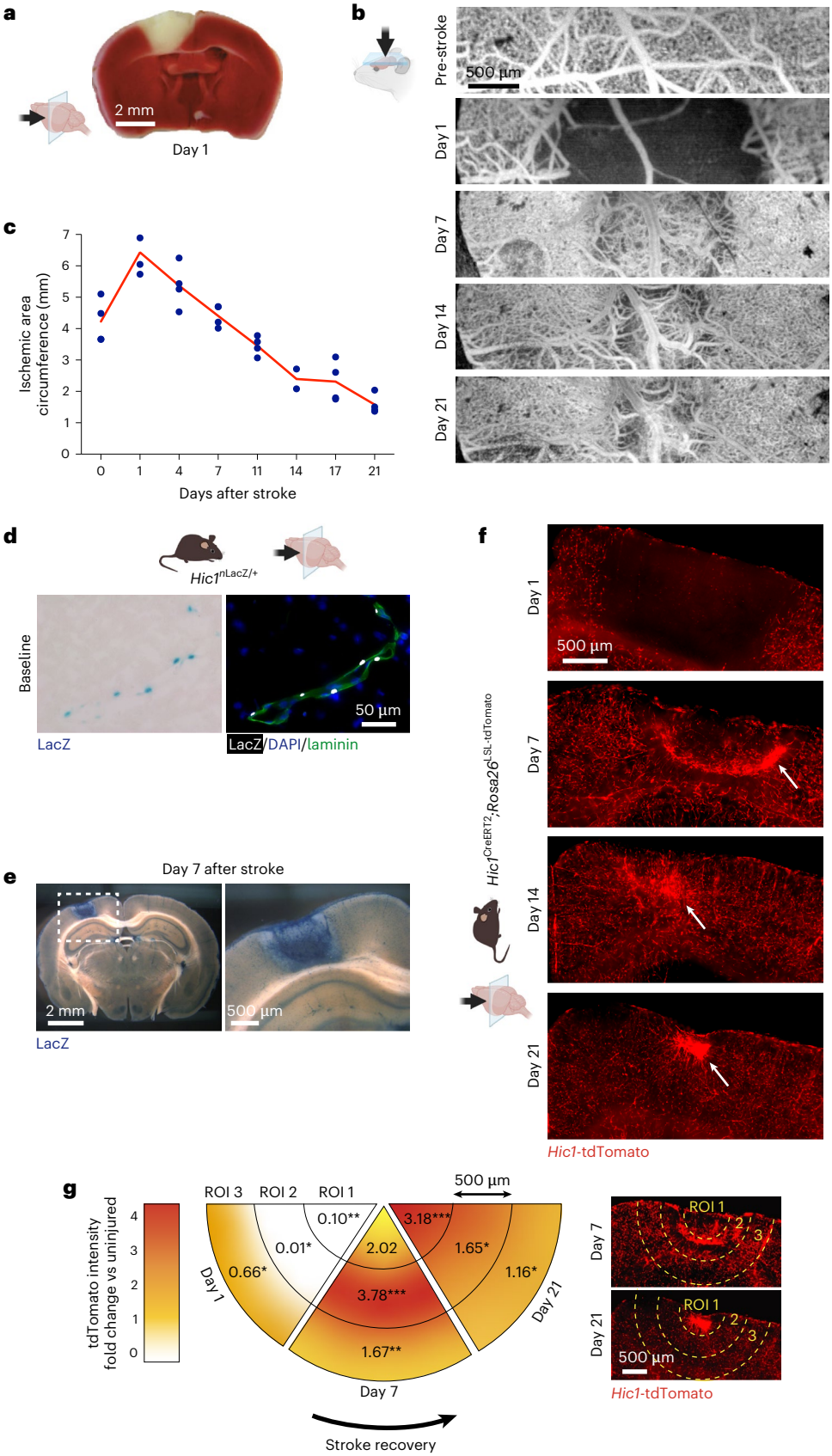

SPCs can proliferate after injury; therefore, we used a *Hic1* lineage tracing mouse with inducible, stable and indelible expression of tdTomato in cells expressing *Hic1*. The *Hic1*^{CreERT2};*Rosa26*$^{LSL\text{-}tdTomato}$ mouse (referred herein as *Hic1*-tdTomato; Extended Data Fig. 1f) allows fate mapping of brain *Hic1*$^+$ populations and their progeny following injury as reporter gene expression was induced by tamoxifen (TAM) injection 1 week before stroke onset. Permanent ischemia induced complete loss of tdTomato$^+$ cells within the ischemic area at 24 h (Fig. 1f)[36,59]. After 7 days, tdTomato$^+$ cells accumulated near the edge of the lesioned area (Fig. 1f). This was observed to coincide with the post-stroke revascularization both spatially and temporally, as the tdTomato$^+$ cells moved inward over 21 days as the size of the ischemic area diminished (Fig. 1f). Quantification of the densely packed *Hic1*-tdTomato$^+$ front over 21 days showed significant and gradual movement toward the core of the ischemic lesion (Fig. 1g). After up to 40 days, when a small core region with incomplete vascular regeneration remained (Extended Data Fig. 1g), the tdTomato$^+$ progeny of *Hic1*$^+$ cells still densely populated the residual lesion, possibly coinciding with areas where revascularization processes remain active, or where scar formation is taking place. The dynamic accumulation of tdTomato$^+$ cells at the front of the progressive revascularization boundary throughout stroke recovery suggested an active involvement of *Hic1*$^+$ cells, or their progeny, in vascular and stromal regeneration.

Hic1 labels pericytes, venular SMCs and perivascular fibroblasts

In peripheral organs, *Hic1* is a marker of SPCs, a population made up of multiple cell types, including pericytes and fibroblasts[14,15,26]. Considering this, we performed in-depth investigations into the identity of the brain-resident *Hic1*$^+$ population. Following TAM administration in the *Hic1*^{CreERT2};*Rosa26*$^{LSL\text{-}tdTomato}$ mouse, *Hic1*$^+$ cells in the adult unperturbed brain were found exclusively in a perivascular location as 99.3% ± 1.2% of tdTomato$^+$ cells associated with CD31$^+$ ECs while 98.9% ± 0.7% and 98.4% ± 0.4% of tdTomato$^+$ cells colocalized with vascular basement membrane components laminin and collagen type IV, respectively (Fig. 2a–c,g and Extended Data Fig. 2a). Cells were embedded inside the basement membrane of cerebral microvessels, within the stromal compartment of the brain and in close association to ECs and astrocytes of the neurovascular unit (Fig. 2c,g and Extended Data Fig. 2b–d). Mural cell marker PDGFRβ colocalized with tdTomato in the entire vascular bed (Fig. 2d,h; 99.7% ± 0.2%). NG2, another mural cell marker, colocalized with tdTomato in the capillary bed where thin-strand pericytes are found but not on arterioles where perivascular fibroblasts are located, which also express PDGFRα (Fig. 2f,h; capillary bed 85.1% ± 6.8%, arterioles 0% ± 0%). Additionally, the pericyte-specific dye NeuroTrace 500/525 labeled capillary tdTomato$^+$ cells (Fig. 2e,h; 99.6% ± 0.9% of *Hic1*-tdTomato$^+$ cells in the capillary bed were labeled by NeuroTrace 500/525) and no ectopic (nonperivascular) expression of the reporter was found (Fig. 2a–h and Extended Data Fig. 2e). The morphological and immunological similarity of brain *Hic1*$^+$ cells and pericytes was also confirmed functionally. Since pericytes are necessary for BBB maintenance at resting state, we used a transgenic model to ablate *Hic1*$^+$ cells (*Hic1*^{CreERT2}; *Rosa26*^{DTA}) and assessed BBB integrity (Extended Data Fig. 2f). Substantial leakage of the dye Evans blue was observed following the specific ablation of *Hic1*$^+$ cells, as was previously reported following PDGFRβ$^+$ pericyte loss[60]. Given the vast overlap with known pericyte markers, our data suggest that virtually all pericytes express *Hic1*; however, due to the lack of specificity of some pericyte markers, we explored the possibility that not all *Hic1*$^+$ cells are pericytes.

Accordingly, bulk RNA sequencing (bulk RNA-seq) of fluorescence-activated cell sorting (FACS)-sorted *Hic1*-tdTomato$^+$ cells showed elevated transcript levels of genes previously identified as enriched not only in pericytes, but also in perivascular fibroblasts (Extended Data Fig. 2g and Supplementary Data 1)[61–65]. Many of these genes are not specific to pericytes and perivascular fibroblasts, and morphological characterization of mural cell subsets has been controversial. Therefore, we performed comprehensive transcriptional profiling of whole-brain FACS-sorted *Hic1*-tdTomato$^+$ cells using droplet-based single-cell RNA sequencing (scRNA-seq; two separate experiments) on the 10x Genomics Chromium single-cell gene expression platform. Both datasets were integrated to correct for technical variations followed by unsupervised clustering, elucidating the presence of three distinct cell populations[66] (Fig. 2i and Extended Data Fig. 3a,b). As observed in the bulk RNA-seq, transcripts of mural cell genes such as *Pdgfrb*, *Vtn*, *Ifitm1* and others, were found throughout all *Hic1*$^+$ cell transcriptional clusters (Extended Data Fig. 3c).

When the transcriptional identity of individual clusters was investigated, the vast majority of brain *Hic1*$^+$ cells revealed a gene transcription signature reminiscent of pericytes, with specifically high levels of genes previously identified as pericyte markers, notably *Rgs5*, *Kcnj8*, *Notch3* and *Higd1b*, among others (Fig. 2l,n, Extended Data Fig. 3d and Supplementary Data 2). This population was further segregated in two subclusters, named pericytes (60.8% of *Hic1*$^+$ cells) and venular SMCs where transcripts of contractile machinery, albeit in low levels, could be found, such as *Acta2* and *Tagln* (21.4% of *Hic1*$^+$ cells; Extended Data Fig. 3e). We confirmed that these *Hic1*-expressing cells are not arterial or arteriolar smooth muscle cells (aSMCs or aaSMCs), as no transcripts of aSMC or aaSMC genes were found (Extended Data Fig. 3f).

Fig. 2 | Brain perivascular expression of *Hic1*, an SPC marker. a, In adult *Hic1*^{CreERT2};*Rosa26*$^{LSL\text{-}tdTomato}$ mice, *Hic1*-tdTomato$^+$ cells in the brain cortex are located along microvessels, observed with FITC-gelatin within the blood vessel lumen. **b**, *Hic1*-tdTomato$^+$ cells are found alongside CD31$^+$ ECs (*z*-depth on orthogonal view = 40 µm). **c**, *Hic1*-tdTomato$^+$ cells are embedded within the laminin$^+$ basement membrane (*z*-depth on orthogonal view = 40 µm). **d**, *Hic1*-tdTomato$^+$ cells express PDGFRβ in the entire vascular bed. PDGFRβ expression is also observed in nonperivascular cells. **e**, *Hic1*-tdTomato$^+$ cells on capillaries are labeled by NeuroTrace 500/525. **f**, *Hic1*-tdTomato$^+$ cells express NG2 in the capillary bed, whereas PDGFRβ$^+$ perivascular fibroblasts, located on arterioles, show no colocalization (arrowheads). NG2 expression is also observed in nonperivascular cells. **g**, Quantification of the colocalization/contact area of *Hic1*-tdTomato$^+$ cells with laminin, collagen type IV and CD31$^+$ cells. ($n = 5$, data are presented as mean values ± s.e.m., one-way analysis of variance (ANOVA)). **h**, Quantification of PDGFRβ$^+$, NG2$^+$ and NeuroTrace 500/525$^+$ positive cells in the *Hic1*-tdTomato$^+$ cell population in different locations along the vascular tree. ($n = 5$; data are presented as mean values ± s.e.m., one-way ANOVA). **i**, scRNA-seq analysis of brain *Hic1*-tdTomato$^+$ cells reveals the presence of three major cell populations: pericytes, venular SMCs and perivascular fibroblasts. Cells were projected into two dimensions via UMAP following Louvain clustering. **j**, *t*-distributed stochastic neighbor embedding (*t*-SNE) reduction of cells based on inferred regulon activity obtained from SCENIC. **k**, Hierarchical clustering using Pearson's correlation across the overall transcriptomes of annotated baseline populations. Values shown are the Pearson correlation coefficient (*r*). **l**, Feature plots of selected pericyte-specific genes enriched in pericytes and venular SMCs. Data are expressed as log-normalized counts. **m**, Feature plots of selected genes enriched in perivascular fibroblasts. Data are expressed as log-normalized counts. **n**, Heat map summarizing relative expression of selected genes (top) and the top ten differentially expressed genes (DEGs; bottom) of each annotated population. Values are shown as *z*-scores of normalized expression. **o**, Hierarchical clustering of all active regulons and their activities across annotated populations. Values are shown as *z*-scores of regulon activities. **p**, In the double transgenic *Hic1*^{CreERT2};*Rosa26*$^{LSL\text{-}tdTomato}$;*Pdgfra*$^{tm11(EGFP)Sor}$/J mouse, perivascular fibroblasts (tdTomato$^+$/GFP$^+$, arrows) are located along pial arterioles, penetrating arterioles and some first-order pre-capillary arterioles. Pericytes and venular SMCs (tdTomato$^+$/GFP$^-$, arrowheads) are located on capillaries and venules, respectively. Quantification of perivascular fibroblast: pericyte/venular SMC ratio relative to branch order shown in the bar plot (data points represent the percentage of cells that are tdTomato$^+$/GFP$^+$). **q**, Morphologies of perivascular fibroblasts, pericytes and venular SMCs along the vascular tree.

https://doi.org/10.1038/s41593-025-01872-y

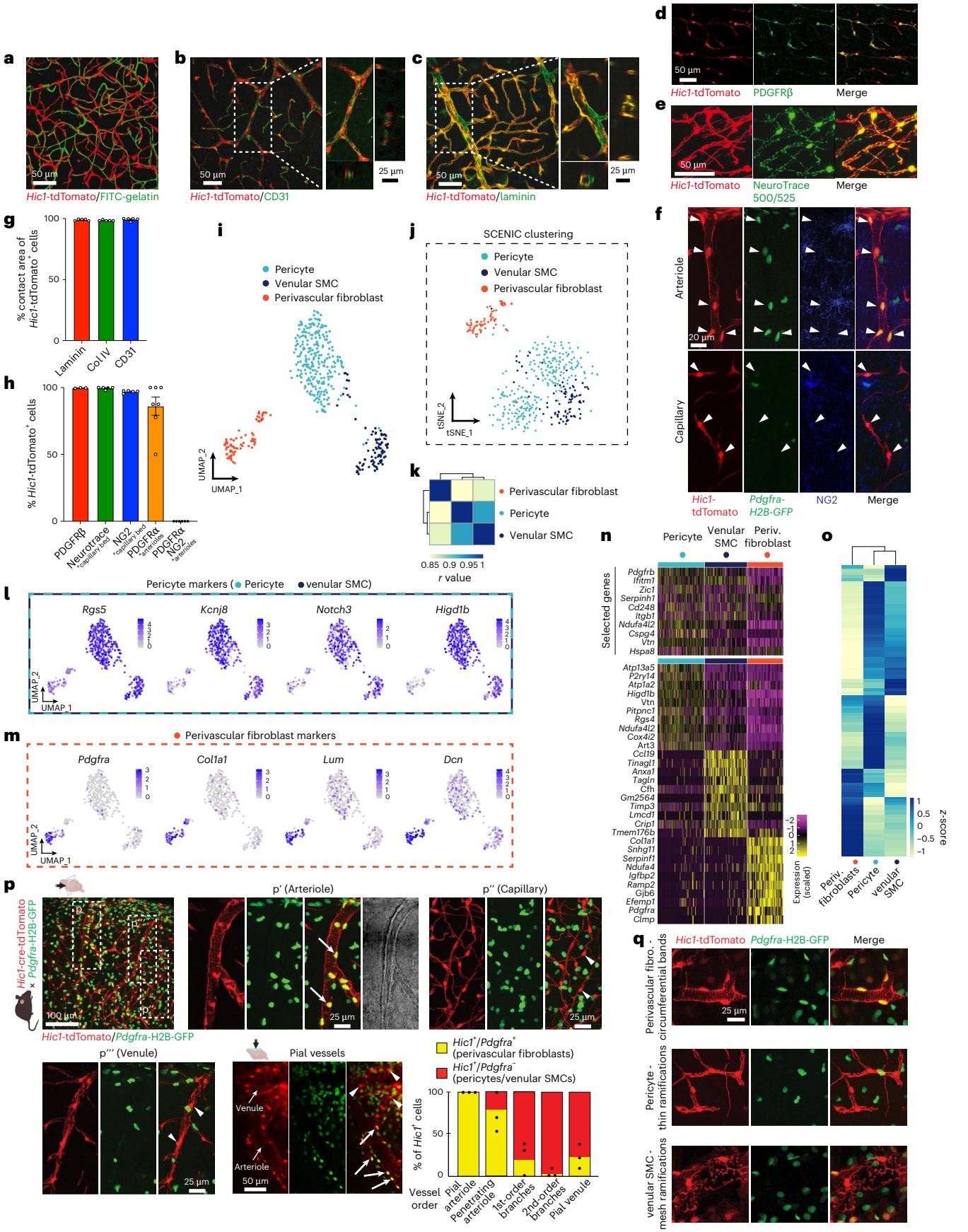

Similarities between pericytes and venular SMCs, and their dissimilarities with aSMCs and aaSMCs are in accordance with previously demonstrated subclasses of mural cells[61]. The second major population of *Hic1*$^+$ brain cells showed perivascular fibroblast characteristics, with enriched transcription of *Pdgfra*, *Col1a1*, *Lum* and *Dcn* (perivascular fibroblasts, 17.8% of the *Hic1*$^+$ cells; Fig. 2m,n and Extended Data Fig. 3g). Interestingly, expression of *Slc1a3* (GLAST) among *Hic1*$^+$ cells was enriched in perivascular fibroblasts (Extended Data Fig. 3g).

Next, we assessed the regulatory programs, or regulons, underlying the annotated populations of *Hic1*$^+$ cells using single-cell regulatory network inference and clustering (SCENIC), an inference tool that reconstructs gene regulatory networks governing distinct transcriptional signatures observed[67]. Cell clustering with regulon activities confirmed that two major populations exist within *Hic1*-expressing cells: pericytes/venular SMCs and perivascular fibroblasts (Fig. 2j and Extended Data Fig. 3h). Interestingly, the pericyte and venular SMC subsets shared overlapping regulatory programs, and thus clustered together, as opposed to those of perivascular fibroblasts. The similarity between the pericyte and venular SMC clusters was also confirmed by correlation analysis of whole-transcriptome signature (Fig. 2k). This highly homogeneous transcriptional regulatory pattern within pericytes and venular SMCs confirms previous observations that pericytes and venular SMCs exist in a continuum where a gradual expression of contractile machinery (in very low levels) defines venular SMCs but an overwhelming similarity exists between both mural cell subtypes[31,61].

Because the use of transcriptional data to identify vascular cell subpopulations and transient activated profiles relies on the expression level of a combination of multiple genes, we have created a searchable database available online where our entire dataset can be browsed in a user-friendly portal (Integrated Single-cell Navigation Portal (ISNAP); https://isnap.rossilab.dev/GSE146930/). This includes the uninjured cells described here as well as the dataset integrating uninjured cells with stroke-activated cells presented in Figs. 3–7. Shown in ISNAP are clustering data obtained from single-cell gene expression and SCENIC-based transcription factor activity along with violin plots.

Transcriptomic signatures of *Hic1*$^+$ cells suggest that the adult brain-resident stromal precursor population consists of a continuum of pericytes and venular SMCs in addition to a distinct subpopulation of perivascular fibroblasts. By crossing the *Hic1*^{CreERT2};*Rosa26*$^{LSL\text{-}tdTomato}$ mouse with a reporter mouse for *Pdgfra* (*Pdgfra*$^{tm11(EGFP)Sor}$/J, referred herein as *Pdgfra*-H2B-GFP), we were able to spatially determine the differential location of both populations along the cortical vascular tree. Perivascular fibroblasts (*Hic1*-tdTomato$^+$/*Pdgfra*-H2B-GFP$^+$) were located exclusively on descending arterioles and first-order and second-order branches, while pericytes (*Hic1*-tdTomato$^+$/*Pdgfra*-H2B-GFP$^-$) lined capillaries (from first order to *n*th order) and venules (Fig. 2p–q and Extended Data Fig. 4a–c). Using this transgenic reporter approach, perivascular fibroblasts (*Hic1*-tdTomato$^+$/*Pdgfra*-H2B-GFP$^+$) accounted for 23.2% of the *Hic1*$^+$ population within the cortex. Morphologically, *Hic1*-tdTomato$^+$ cells with circumferential bands around large vessels were *Pdgfra*$^+$ (perivascular fibroblasts; Fig. 2p–q). Note that these *Hic1*$^+$/*Pdgfra*$^+$ cells do not transcribe contractile proteins or *Cspg4* (NG2; perivascular fibroblast cluster of our scRNA-seq analysis; Extended Data Fig. 3d,e) and, therefore, are different from SMCs that share similar morphology and location. Furthermore, 98.6% of perivascular *Pdgfra*$^+$ cells are also *Hic1*$^+$, suggesting the vast majority of perivascular fibroblasts express *Hic1* at rest. However, 92.3% of all *Pdgfra*$^+$ cells (including nonperivascular cells) do not express *Hic1*, reflective of a nonperivascular *Hic1*$^-$/*Pdgfra*$^+$ oligodendrocyte progenitor population (Extended Data Fig. 4c). *Hic1*$^+$ ensheathing pericytes on the first-order to fourth-order capillary branches, as well as thin-strand pericytes with processes running longitudinally to deeper capillaries did not express *Pdgfra*, and are therefore pericytes (Fig. 2p–q)[31]. On ascending venules, *Hic1*-tdTomato$^+$ cells with a ramified morphology also did not express *Pdgfra* (Fig. 2p,q). Quantification of SPCs in the pia revealed that all *Hic1*$^+$ SPCs on pial arterioles are *Pdgfra*$^+$ and thus perivascular fibroblasts. On pial venules, the population of *Hic1*$^+$/*Pdgfra*$^+$ perivascular fibroblasts accounts for 21.4% of SPCs, in accordance with *Col1a1*-based mouse models that showed venular perivascular fibroblasts only on large-diameter ascending venules, close to the pial surface (Fig. 2p).

Activated pericytes and fibroblasts in the ischemic area following stroke

Our initial observations showed that after injury, accumulation of *Hic1*-tdTomato$^+$ cells was spatially and temporally correlated with post-stroke remodeling, suggesting pericytes, venular SMCs and perivascular fibroblasts not only share baseline SPC characteristics such as stromal location and marker expression, but also respond to injury as expected and predicted for SPCs. Another hallmark of SPCs is the ability to undergo cellular activation, a transient phenotype associated with injury-dependent functions. Within the ischemic area 7 days after stroke, we observed striking changes in tdTomato$^+$ cell phenotype, characterized by a distinctive morphological transformation to flat round cell bodies with short and stubby protrusions (Fig. 3a,b). We further investigated whether putative SPC populations of pericytes, venular SMCs and perivascular fibroblasts undergo activation in the stroke-affected area by characterizing the transcriptional profile of lineage-tracked *Hic1*-tdTomato$^+$ cells. To do this, we performed scRNA-seq analysis of tdTomato$^+$ cells collected in the ischemic lesion at day 7 after stroke compared to those collected from the contralateral hemisphere (Fig. 3c and Extended Data Fig. 5). FACS-sorted tdTomato$^+$ cells of both regions were processed for scRNA-seq in two independent

Fig. 3 | Activated pericytes and fibroblasts are present in the ischemic area following stroke. a, Images of cortex from brain slices showing death of *Hic1*-tdTomato$^+$ cells in the ischemic core (IC) at day 1 after stroke, accumulation and changes in morphology of *Hic1*-tdTomato$^+$ cells in the IC at day 7 and perivascular location of *Hic1*-tdTomato$^+$ cells in the revascularized area (R) at day 21. **b**, In vivo cortical images showing lack of viable *Hic1*-tdTomato$^+$ cells in the ischemic core at day 1 after stroke, accumulation and changes in morphology of *Hic1*-tdTomato$^+$ cells in the ischemic core at day 7 and perivascular location of *Hic1*-tdTomato$^+$ cells in the revascularized area at day 21. Orthogonal view is provided to illustrate the depth of imaged *Hic1*-tdTomato$^+$ cells. Images were acquired in different animals at the indicated time points. **c**, 7 days after stroke, tissue from the stroke lesion and from the contralateral hemisphere was collected, cells were FACS-sorted for tdTomato and scRNA-seq analysis was performed. **d**, UMAP plot following scRNA-seq of FACS-sorted tdTomato$^+$ cells collected from contralateral hemispheres (contralateral) or from the ischemic area at day 7 after stroke (stroke). The dotted line shows the general demarcation between cells collected in the contralateral hemisphere versus cells collected in the ischemic lesion and is shown for reference on all subsequent UMAP plots. **e**, UMAP plot showing 7 annotated cell identities used for further analysis. **f**, Hierarchical clustering using Pearson's correlation across transcriptomes of annotated populations. Values shown are the Pearson correlation coefficient (*r*). **g**, Feature plots showing transcription of selected SPC, mural cell and activation markers. Data are expressed as log-normalized counts. **h**, Heat map of the top 10 differentially transcribed genes for annotated populations. Values are shown as *z*-scores of normalized expression. **i**, Feature plots showing transcription of selected pericyte-specific genes. Data are expressed as log-normalized counts. **j**, Feature plots showing transcription of selected fibroblast-specific genes. Data are expressed as log-normalized counts. **k**, Feature and violin plots depicting *Slc1a3* enrichment in baseline and activated perivascular fibroblasts but not in pericytes. **l**, In the double transgenic *Hic1*^{CreERT2};*Rosa26*$^{LSL\text{-}tdTomato}$;*Pdgfra*$^{tm11(EGFP)Sor}$/J mouse after stroke, activated fibroblasts (tdTomato$^+$/GFP$^+$, arrowhead) and activated pericytes (tdTomato$^+$/GFP$^-$, arrow) are observed (*z*-depth on orthogonal view = 20 µm). Quantification for resting state (also see Fig. 1) and post-stroke day 7 is shown on the right ($n = 5$; scatterplot indicates the individual values, and the black line indicates the median).

https://doi.org/10.1038/s41593-025-01872-y

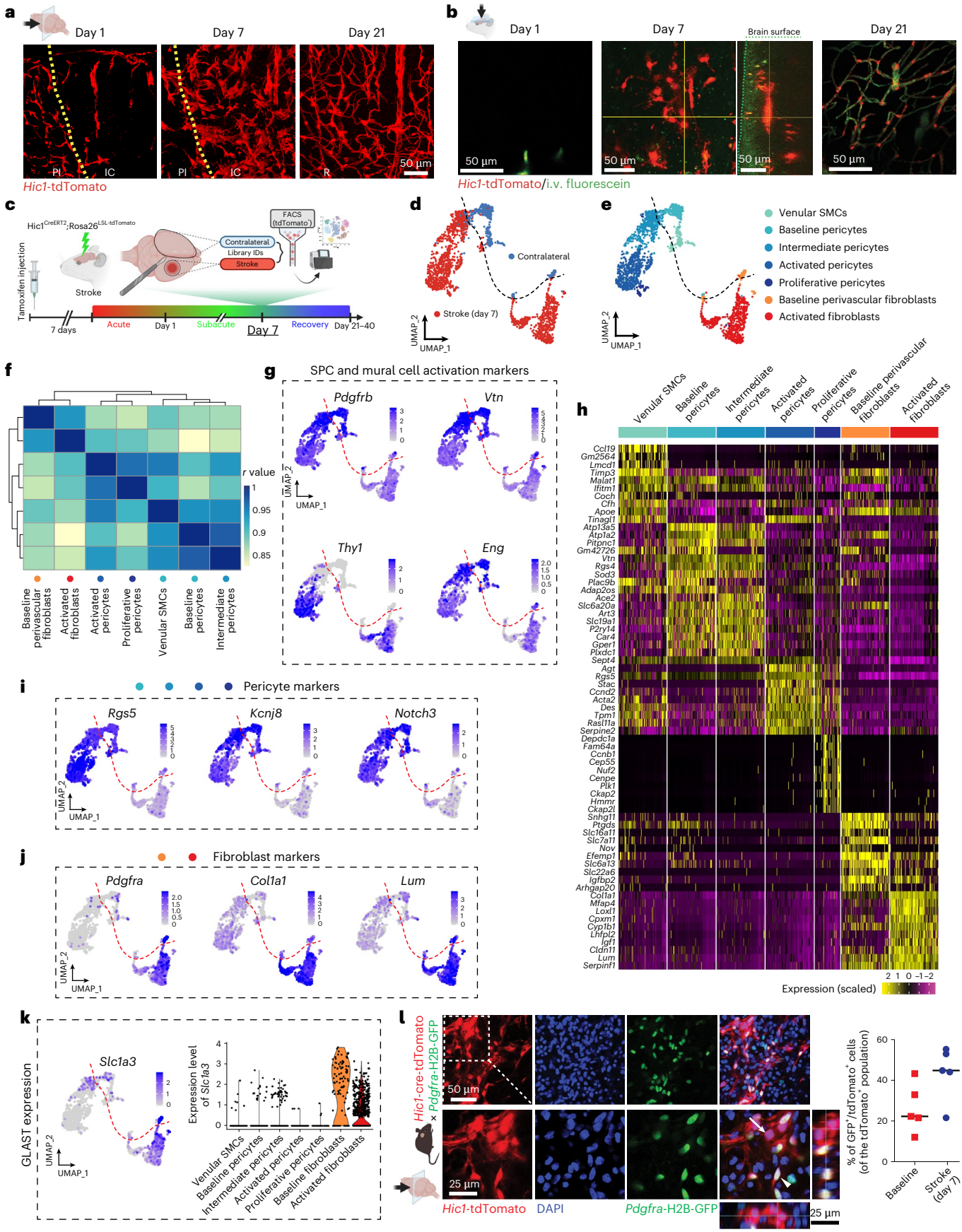

experiments (lesion and contralateral samples from 4–5 mice for each experiment). Unsupervised clustering of integrated datasets showed that striking differences exist between the transcription profiles of quiescent versus stroke-associated *Hic1*-tdTomato$^+$ cells (Fig. 3d, Extended Data Fig. 6a,b and Supplementary Data 3). Importantly, these stroke-activated *Hic1*-tdTomato$^+$ cells were clearly separated into two major discrete clusters, with a pericyte and venular SMC group distinct from a fibroblast group (Fig. 3e). Whole-transcriptome correlation analysis confirmed that the signatures of both groups remained distinctly separate in the injured area (Fig. 3f). All stroke-associated *Hic1*-tdTomato$^+$ cells showed transcripts for stromal/mural cell markers *Pdgfrb*, *Vtn* and others while showing enrichment for stromal/mesenchymal activation markers *Thy1* and *Eng*, suggesting they conserve their potential SPC identity while inducing an activated program (Fig. 3g and Extended Data Fig. 6c). Stroke-activated cells stemming from the pericyte cluster, despite undergoing major morphological and locational changes in response to injury, retained elevated transcription of pericyte-specific genes like *Rgs5*, *Kcnj8*, *Notch3* and others (Fig. 3h,i and Extended Data Fig. 6d). These stroke-activated cells expressing pericyte markers clustered into homogeneous groups (termed intermediate and activated pericytes, more details below), suggesting that pericytes dynamically change into an activated transcriptional state following stroke. Similarly, perivascular fibroblast progeny within the stroke-affected area modified their transcriptional state while retaining their fibroblast gene-set signature (*Pdgfra*, *Col1a1*, *Lum*; Fig. 3h,j and Extended Data Fig. 6e). Using transcriptomic identity, the proportion of pericytes and fibroblasts derived from *Hic1*$^+$ cells within the ischemic area was 61.2% and 38.8%, respectively. GLAST-expressing cells (previously termed 'type A pericyte') have been shown to give rise to fibroblast-like cells upon injury[13,44,46]. Our data show that GLAST (*Slc1a3*) is only enriched in the perivascular fibroblast subpopulation, both in baseline conditions and after stroke (Fig. 3k). While differences in cell-type nomenclature may lead to this discrepancy, our data nevertheless show that within the stroke lesion, there is a clear population of activated pericytes (enriched for *Rgs5*, *Kcnj8*, *Notch3*) that are distinct from the progeny of perivascular fibroblasts (enriched for *Pdgfra, Col1a1* and *Slc1a3*).

We further confirmed the presence of pericytes and perivascular fibroblasts within the lesioned area using a transgenic *Hic1*^{CreERT2}; *Rosa26*$^{LSL\text{-}tdTomato}$; *Pdgfra*$^{tm11(EGFP)Sor}$/J mouse. At day 7 after stroke, both populations were present as 56.2% of tdTomato$^+$ cells were GFP$^-$, indicative of pericytes, while 43.8% of tdTomato$^+$ cells were GFP$^+$, indicative of a fibroblast population expressing *Pdgfra* (Fig. 3l). These results indicate that two populations of putative *Hic1*$^+$ SPCs, namely pericytes and perivascular fibroblasts, coexist after injury and suggests they may differentially contribute to injury repair. Note that within the lesion, 57.0% of *Pdfgra*-expressing cells do not express tdTomato, possibly representing cells derived from fibroblast populations other than brain-resident perivascular fibroblasts, or from oligodendrocyte progenitor cells also known to participate in CNS injury remodeling[68,69].

Transcriptional signature of stroke-activated pericytes and fibroblasts

As observed in the uniform manifold approximation and projection (UMAP) representation of cell transcriptional profile clustering, the resting-state pericytes and venular SMCs from the uninjured contralateral hemisphere (referred to as baseline pericytes and venular SMCs; Fig. 3e) clustered separately from the stroke-associated ones (intermediate, activated and proliferative pericytes; Fig. 3e), indicating that activated pericytes possess a distinct transcriptional profile. Interestingly, a subcluster of the stroke-associated pericytes exhibited increased expression of genes associated with mitotic and cell cycle processes, indicating proliferative pericytes exist within the stroke region (proliferative pericytes; Fig. 3e and discussed further below). UMAP clustering revealed that some pericytes are found in an intermediate state of activation, and these cells were excluded from further comparisons between baseline and activated pericytes. Pathway enrichment analysis was performed to compare overrepresented biological processes in the activated pericytes relative to the baseline pericytes (Fig. 4a,b). This yielded pathways indicative of increased transcriptional and translational activity, ECM production, cellular adhesion, as well as angiogenesis and vascular development.

Examination of the fibroblast-like subpopulation of SPCs also revealed a dynamic change in their transcriptional profile upon injury. The cluster of perivascular fibroblasts in their resting state (baseline perivascular fibroblasts) segregated separately from the stroke-associated fibroblast-like populations (activated fibroblasts; Fig. 3e). Biological processes upregulated in activated versus baseline perivascular fibroblasts included terms linked to ECM production/organization and connective tissue development, suggesting a more fibrogenic profile (Fig. 4c,d). Interestingly, a fibrogenic scar-forming function has been shown for GLAST-expressing type A pericytes[13,46]. Direct comparison of stroke-activated pericytes to stroke-activated fibroblasts revealed biological processes linked to vessel reorganization enriched in pericytes, with ECM-related processes enriched in fibroblasts (Fig. 4e,f).

Global changes in transcriptional signatures and cell states such as those observed here after stroke are governed upstream by changes in transcription factor activity. Accordingly, hierarchical clustering based on transcription factor activity using SCENIC showed that annotated populations were primarily segregated based on their quiescent versus activated cell state while still showing pericyte-specific versus fibroblast-specific patterns (Fig. 4g and Extended Data Fig. 6f). Regulons associated with the quiescent to stroke-activated pericyte transition include *Foxf2* and *Mef2a*, while stroke-associated fibroblasts showed elevated activity of *Creb3l1* and *Runx1* (Fig. 4h).

Taken together, our in-depth scRNA-seq analysis of *Hic1* lineage cells after stroke demonstrates that both pericytes and perivascular fibroblasts undergo activation after injury and maintain distinct transcriptional programs. Hence both populations demonstrate this key SPC characteristic and may participate in the post-stroke response leading to regeneration of the cerebrovasculature.

Hic1$^+$ populations proliferate after stroke

Peripheral SPCs and resident brain pericytes have been shown to proliferate under various conditions, and our imaging and transcriptomic data suggested that proliferation of brain *Hic1*-tdTomato$^+$ cells occurred following stroke. We explored whether the apparent increase in tdTomato$^+$ cells truly arose from proliferation after stroke injury by measuring 5-ethynyl-2′-deoxyuridine (EdU; daily injections after stroke)

Fig. 4 | Transcriptional profiles of activated pericytes and fibroblasts following stroke. a, Heat map of the top 50 upregulated DEGs in stroke-activated pericytes relative to baseline pericytes. Values are shown as *z*-scores of normalized expression. **b**, Pathway enrichment analysis showing selected terms overrepresented in stroke-activated pericytes compared to baseline pericytes. **c**, Heat map of the top 50 upregulated DEGs in stroke-activated fibroblasts relative to baseline fibroblasts. Values are shown as *z*-scores of normalized expression. **d**, Pathway analysis showing selected terms overrepresented in stroke-activated fibroblasts compared to baseline perivascular fibroblasts. **e**, Heat map of top 50 upregulated DEGs in stroke-activated pericytes relative to stroke-activated fibroblasts. Values are shown as *z*-scores of normalized expression. **f**, Pathway enrichment analysis showing selected terms overrepresented in stroke-activated pericytes compared to stroke-activated fibroblasts. **g**, Hierarchical clustering of all active regulons and their activities across annotated populations obtained from SCENIC. Values are shown as *z*-scores of regulon activities. **h**, Feature plot of selected transcription factors and their activities obtained from SCENIC. Values shown are area under the curve scores of active regulons. GO, Gene Ontology.

https://doi.org/10.1038/s41593-025-01872-y

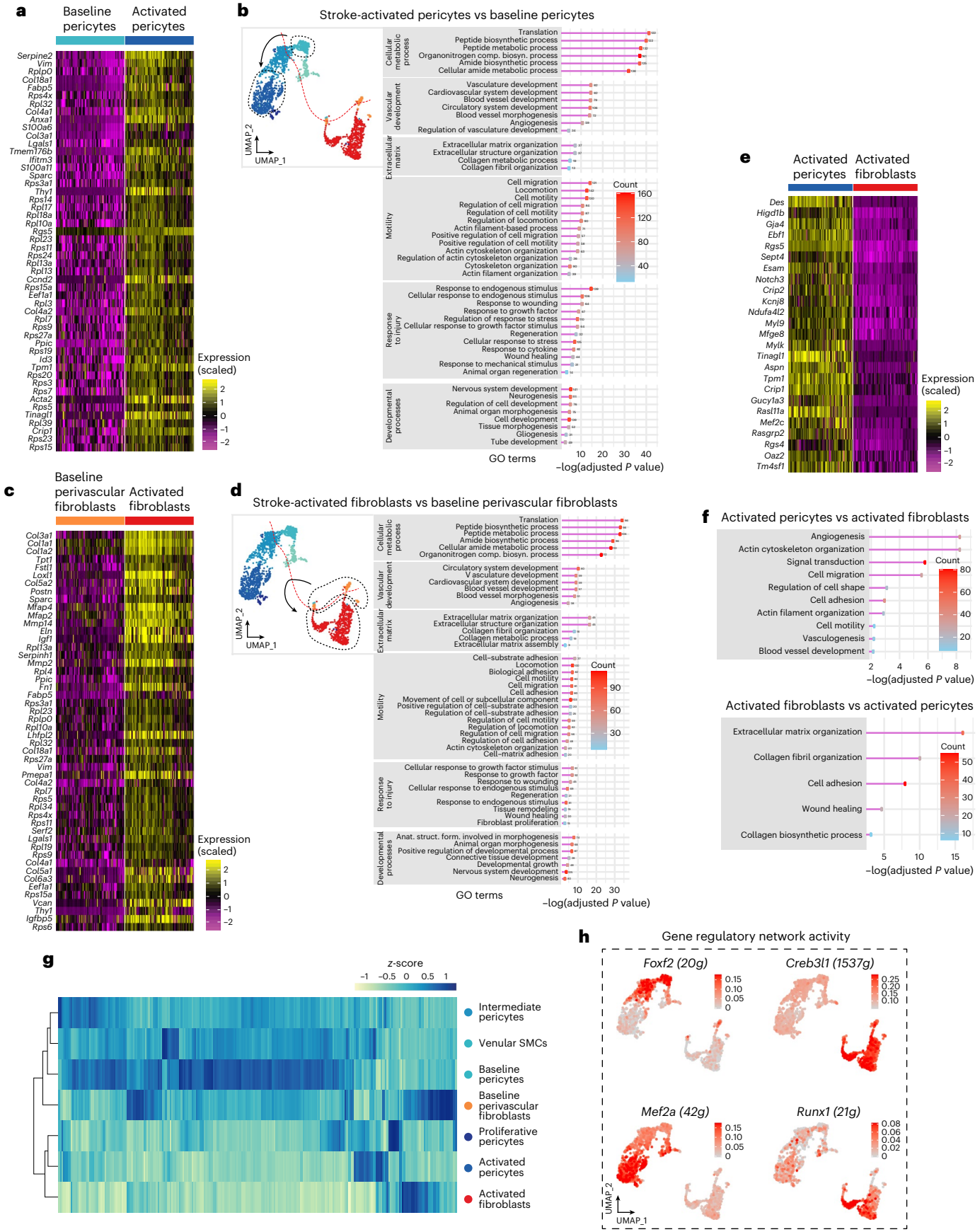

incorporation at day 7 after injury (Fig. 5a,b). Within the ischemic area, 69.9% of newly appearing tdTomato$^+$ cells were EdU$^+$ and, therefore, daughter cells of *Hic1*$^+$ SPCs that were outside the ischemic core region because complete loss of *Hic1*$^+$ cells was observed at day 1 within the ischemic core. Furthermore, our scRNA-seq data showed a discrete population of highly proliferative pericytes with enriched transcripts of proliferation and cell cycle-related genes (*Mki67*, *Plk1*, *Top2a*, *Ccnb1* and *Bub1* among others) along with enriched pericyte-specific genes (*Rgs5*, *Kcnj8*, *Notch3* and *Higd1b*; Fig. 5c,d). Accordingly, pathway enrichment analysis comparing the proliferative pericytes to other stroke-activated pericytes identified terms related to cell cycle control, cell division and proliferation (Fig. 5e).

Activated SPCs are motile and disengage from vessels

Our observations of tdTomato$^+$ cells 7 days after stroke showed morphologically altered activated pericytes and fibroblasts that had accumulated within the ischemic area. This implies that pericytes and perivascular fibroblasts, which are essentially immobile under resting conditions[32], acquire a motile phenotype upon activation. Time-lapse in vivo two-photon imaging of the ischemic zone at day 7 after stroke showed considerable motility of stroke-activated tdTomato$^+$ cells over a time course of 6 h (Fig. 5f). In contrast, *Hic1*-tdTomato$^+$ cells from uninjured areas did not display any movement over the same time frame (Extended Data Fig. 7a,b). Accordingly, the activated pericyte population showed a striking upregulation of genes associated with cell motility such as *Tagln*, *Acta2*, *Myh11*, *Mylk*, *Tpm1* and *Tpm2*, and enrichment of pathways linked to motility (Fig. 5g,h).

In their normal mature state, both pericytes and perivascular fibroblasts are found in the stromal compartment, embedded within, or adhered to the basement of cerebral vessels (Figs. 1d and 2c and Extended Data Fig. 2a). In contrast, activated *Hic1*-tdTomato$^+$ cells were found in an area devoid of functional blood flow within the ischemic core (Figs. 1b,e,f and 3a). tdTomato$^+$ cells were also observed to be detached from the vasculature within the peri-infarct area, supporting the concept that stromal cells can disengage from vessels when shifting into an activated phenotype (Fig. 5i and Extended Data Fig. 8b). Interestingly, our scRNA-seq data show significant upregulation of *Rgs5* transcription in activated pericytes, and RGS5 was recently shown to drive pericytes to shift from their perivascular location to the parenchyma (Fig. 5j)[70,71]. During embryonic development, pericytes can travel to areas of angiogenesis via vasculogenic tubes[72]. Similarly, we observed tdTomato$^+$ cells within the lumen of laminin or collagen type IV tubes in the post-stroke recovery stage (Fig. 5k,l and Extended Data Fig. 8c). Along with the frequent observation of tdTomato$^+$ cells migrating on remaining non-perfused vessel-like structures (Extended Data Fig. 8d,e), their appearance within remnant laminin or collagen sleeves suggests these are pathways for activated SPCs to migrate into the inner ischemic area.

Activated SPCs produce ECM components

In parallel to the accumulation of activated tdTomato$^+$ cells within the stroke core, we observed the transient formation of a dense mesh of laminin and collagen type IV, two ECM components critical in the composition of the basement membrane during angiogenesis and tissue compartmentalization (Fig. 5k,l and Extended Data Fig. 8f,g). A concomitant increase in transcription of genes coding for collagen IV and laminins (*Col4a1*, *Col4a2*, *Lama2*, *Lama4*, *Lamb1*, *Lamb2*, *Lamc1*) was observed in both lesion-associated pericyte and fibroblast populations (Fig. 5m). This demonstrates that both activated putative SPC populations produce matrix components that have been shown to be necessary for vascular basement membrane formation, as well as for BBB maturation and astrocytic endfoot polarization, all required for proper vascular development[73]. On the other hand, fibroblasts have repeatedly been shown to produce matrix components that lead to scar formation by activating a fibrogenic program after injury[15,74,75]. These ECM molecules include collagen type I and III (*Col1a1*, *Col3a1*, *Col5a2*, among others) and fibronectin (*Fn1*), which were particularly enriched in the activated fibroblast population (Fig. 5m). Similarly enriched in stroke-associated fibroblasts (but not in pericytes) were chondroitin sulfate proteoglycans like versican (*Vcan*), known to inhibit axon growth following CNS injury (Fig. 5m)[76]. Together, this suggests a possible dichotomy between the transient stroke-activated functions of the proposed brain SPC populations, where activated pericytes promote angiogenesis while the activated fibroblasts mostly drive scar formation.

Activated SPCs accumulate on the ischemic side of the astroglial border

During stroke recovery, astrocytes form a clearly defined astroglial border delineating the outer boundary of the ischemic core and blood-perfused peri-infarct cortical regions[77,78]. By comparing the distribution of glial fibrillary acidic protein-positive (GFAP$^+$) astrocytes to *Hic1*-tdTomato$^+$ progeny after stroke, we observed that following proliferation and invasion of the ischemic area, the tdTomato$^+$ cells accumulate adjacent to the inner edge of the astrogliosis region (Fig. 6a and Extended Data Fig. 9a–c). The region of astrogliosis delineates a dynamic border that follows alongside the area of activated putative SPCs over the course of days and progressively moves into the ischemic region, giving way to revascularized tissue. Our observations of this dynamic process suggest that activated pericytes are part of the initial phase of cerebral vessel regeneration, before astrocytic involvement, showing similarities between the spatiotemporal pattern of pericyte involvement during development and post-injury cerebrovascular regeneration.

Fig. 5 | Stroke-activated SPCs proliferate, are motile, disengage from vessels and deposit basement membrane components. a, Graphical illustration of the experimental timeline. All data shown in Fig. 5 were obtained 7 days after stroke. **b**, Stroke-activated SPCs (arrowheads) proliferated and incorporated EdU 7 days after stroke (daily injections after stroke). **c**, Feature plots showing enrichment of cell cycle-associated and proliferation-associated genes in the stroke-associated proliferative pericyte cluster (arrow). Data are expressed as log-normalized counts. **d**, Heat map of selected pericyte-associated, fibroblast-associated and proliferation-associated genes showing the pericyte identity of the proliferative stroke-associated SPCs. Values are shown as *z*-scores of normalized expression. **e**, Pathway enrichment analysis showing selected terms overrepresented in stroke-activated proliferative pericytes compared to stroke-activated pericytes. **f**, Stroke-activated SPCs show cellular motility over a 6-h time lapse, observed through an acute cranial window. Quantification of cell velocity (right) shows a significant difference in motility between lesion-associated cells and cells in uninjured tissue ($P < 0.0001$; horizontal line represents the median). Colored lines indicate movement of selected individual cells over the entire time course. An orthogonal view is provided to illustrate depth of imaged *Hic1*-tdTomato$^+$ cells. Arrowheads point to stationary structures, serving as landmarks for the longitudinal analysis. **g**, Feature plots showing enrichment of selected motility-related and contractility-related genes in the stroke-activated pericytes cluster. Data are expressed as log-normalized counts. **h**, Pathway enrichment analysis showing selected terms overrepresented in stroke-activated pericytes compared to baseline pericytes. **i**, In vivo imaging of the peri-ischemic region shows activated SPCs (arrowheads) detached from vessels with functional blood flow (i.v. dextran-conjugated fluorescein). **j**, Violin plot showing increased transcription of *Rgs5* in activated pericytes (adjusted P value = 7.98×10^{-86} for activated pericyte versus baseline pericyte). Also see feature plot of *Rgs5* transcription in Fig. 3i. **k**, Overproduction of basement membrane component laminin observed 7 days after stroke in the region of accumulated activated SPCs. Stroke-activated SPCs are also observed inside laminin sleeves (*z*-depth on orthogonal view = 55 µm). **l**, Overproduction of basement membrane component collagen type IV observed 7 days after stroke in the region of accumulated activated SPCs (*z*-depth on orthogonal view = 50 µm). **m**, Heat map of selected genes linked to basement membrane formation enriched in stroke-activated pericytes, and enrichment of fibrogenic genes in activated fibroblasts. Values shown as *z*-score of normalized expression.

https://doi.org/10.1038/s41593-025-01872-y

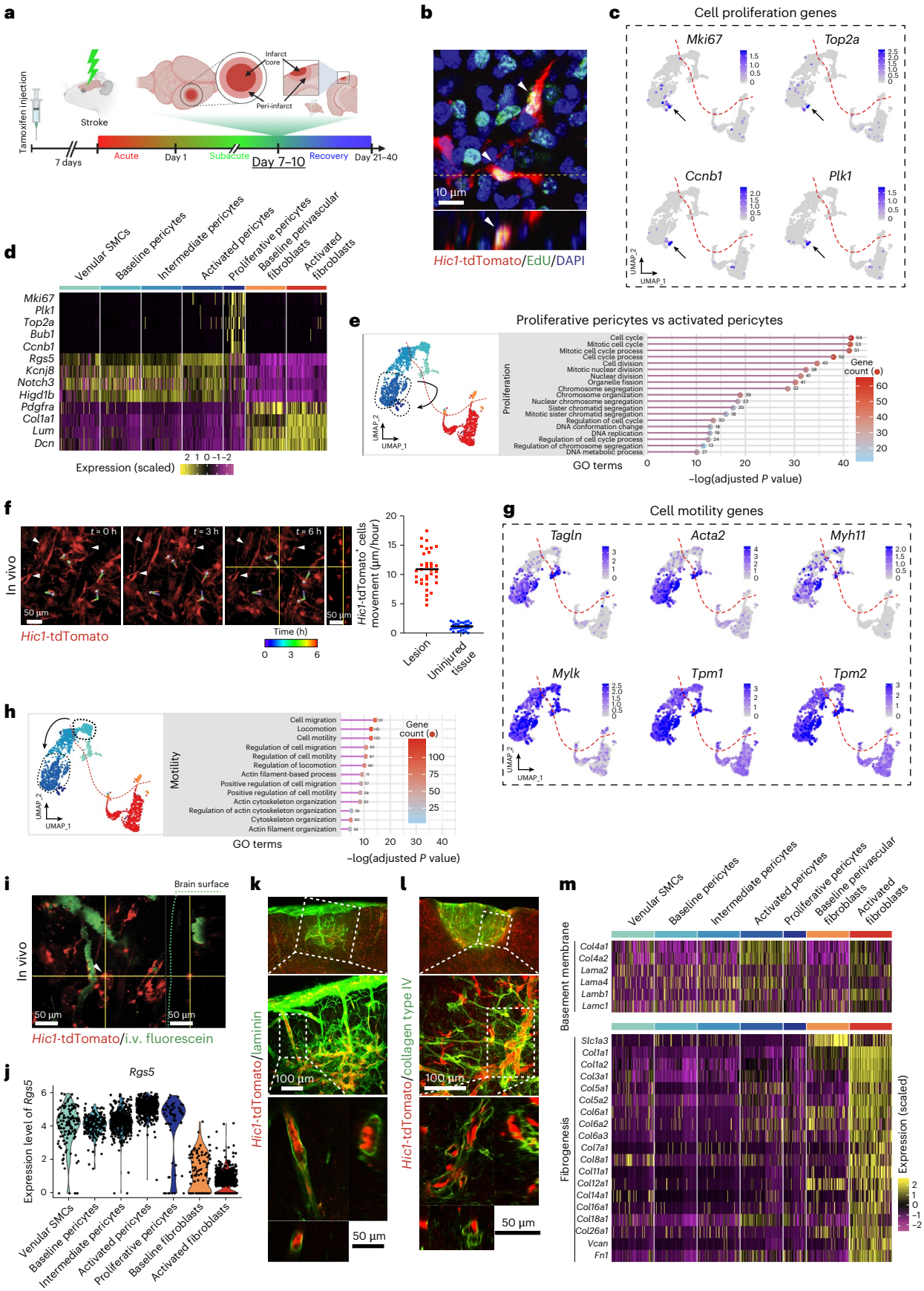

https://doi.org/10.1038/s41593-025-01872-y

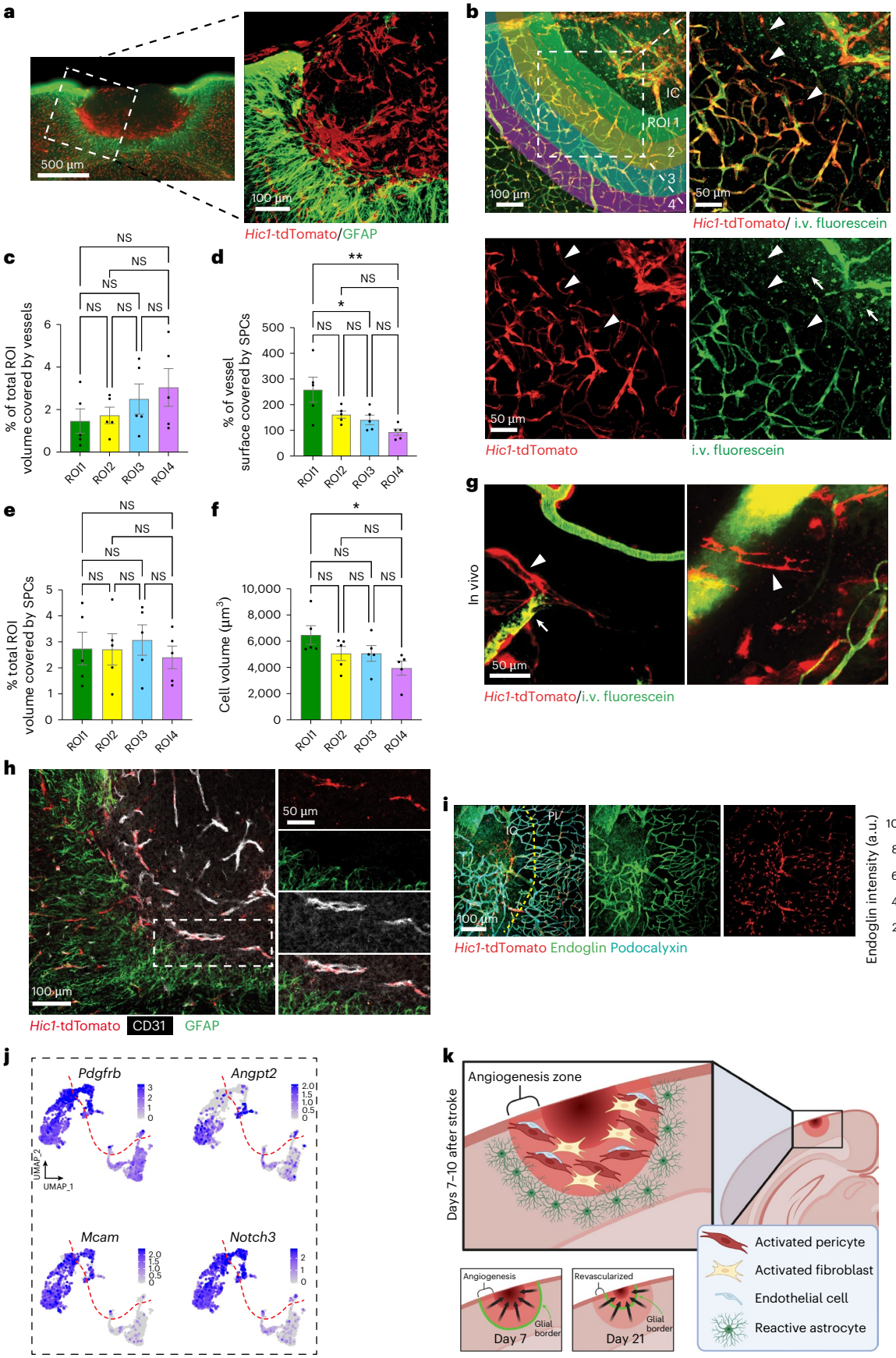

Fig. 6 | Angiogenic SPCs after stroke associate with astrocytes and ECs. **a**, Stroke-activated *Hic1*-tdTomato$^+$ cells accumulate on the ischemic side of the GFAP$^+$ reactive astrogliosis border. **b**, Stroke-activated *Hic1*-tdTomato$^+$ cells accumulate inside the ischemic core in a region devoid of capillary blood flow (observed with i.v. dextran-conjugated fluorescein). In the early active revascularization zone (ROI 1), activated *Hic1*-tdTomato$^+$ cells show thin-strand ramification morphology indicative of nascent immature vessels before blood flow establishment (arrowheads). In revascularized areas (ROI 4), *Hic1*-tdTomato$^+$ cells show morphology similar to resting conditions. Arrows show leakage of 70-kDa dextran-conjugated fluorescein in the angiogenic zone where the BBB of immature vessels is leaky. **c**, Quantification of total ROI volume covered by vessels. ($n = 5$; data are presented as mean values ± s.e.m., one-way ANOVA). **d**, Quantification of the percentage of vessel surface covered by SPCs. ($n = 5$; data are presented as mean values ± s.e.m., one-way ANOVA; ROI 1 versus ROI 3; $P = 0.039$, ROI 1 versus ROI 4; $P = 0.003$). **e**, Quantification of the total ROI volume covered by SPCs. ($n = 5$; data are presented as mean values ± s.e.m., one-way ANOVA). **f**, Quantification of the cellular volume of SPCs ($n = 5$; data are presented as mean values ± s.e.m., one-way ANOVA; ROI 1 versus ROI 4; $P = 0.004$). **g**, In vivo imaging of the peri-ischemic region shows evidence of capillary-associated thin-strand ramification pericytes (arrowheads) on nonfunctional vessels (that is, not filled by i.v. fluorescein). Evidence of stalled blood flow indicative of immature vessels was also observed near those thin-strand pericytes (arrows). **h**, On the ischemic side of the reactive astrogliosis border, stroke-activated *Hic1*-tdTomato$^+$ cells associate in close proximity to CD31$^+$ ECs. **i**, Stroke-activated *Hic1*-tdTomato$^+$ cells associate with ECs overexpressing endoglin (PI, peri-infarct region). Quantification of the endoglin expression intensity on podocalyxin$^+$ cells relative to the distance from the ischemic lesion is also shown. **j**, Feature plots showing transcription of selected genes involved in angiogenic signaling between ECs and pericytes. Data are expressed as log-normalized counts. **k**, Graphical illustration of the angiogenesis zone lining the inner side of the glial border. This angiogenic zone progressively reperfuses the ischemic region. a.u., arbitrary units; NS, not significant; $^*P < 0.05$; $^{**}P < 0.01$; $^{***}P < 0.001$.

To analyze the dynamics of the putative tdTomato$^+$ SPCs in a spatial manner, we segmented four regions of interest (ROIs) of 100 µm originating at the astroglial border, outside the lesion core and progressing away from it toward nonischemic tissue (Fig. 6b; ROI 1 green (nearest to lesion) to ROI 4 purple (healthy tissue)). Capturing tdTomato$^+$ vessel coverage in a volumetric analysis, we found a significant over-coverage of vessels by SPCs at the front of the angiogenic zone (ROI 1, green), suggesting an enhanced role for SPCs during early active vascular reorganization. Vessels that were observed with an over-coverage of tdTomato$^+$ SPCs were yet mostly devoid of active blood flow, as could be seen by the lack of fluorescein (injected intravenously (i.v.); Fig. 6b). Additionally, within ROI 1, tdTomato$^+$ SPCs displayed an activated morphological phenotype, with a larger overall volume (Fig. 6c–f). This phenomenon of large pericytes covering newly established, yet not fully functional vessels, was also observed in vivo and in brain slices using two-photon microscopy (Fig. 6g and Extended Data Fig. 9d). As the angiogenic front is spatially and temporally dynamic, this suggests that *Hic1*$^+$ progeny alter their morphology with the progression of the revascularization effort.

Pro-angiogenic activated SPCs associate with ECs

Developmental neovascularization requires close cell–cell interaction and paracrine communication between pericytes and lumen-lining ECs[28,37,38,79]. During stroke recovery, we observed close association of ECs (stained for CD31 or podocalyxin) with tdTomato$^+$ activated SPCs, which occurred on the inner (lesion) side of the astrogliosis border (Fig. 6h,i and Extended Data Fig. 9e,g). Further supporting the presence of neovascularization in the pericytosis zone is the concomitant presence of endoglin on ECs, which show significantly higher expression at the front of the angiogenic zone (spanning 100 µm into the lesion), colocalizing with endothelial marker podocalyxin (Fig. 6i and Extended Data Fig. 9f). Endoglin intensity on ECs gradually decreased away from the stroke core, indicating a gradient of ongoing angiogenesis. Additionally, ECs are known to produce tip cells for developmental vascularization. We used isolectin B4 (IB4) to look for the filament-like structures and found them present within the angiogenic zone and the peri-infarct area, where they protrude from ECs proximal to SPCs (Extended Data Fig. 9g). Endothelial–pericyte signaling pathways regulating blood vessel formation and maturation include PDGFB–PDGFRB, ANG-1/ANG-2–Tie2 and Notch[27,29]. Our transcriptomic data reveal that stroke-associated pericytes, to a much higher extent than fibroblasts, actively transcribe the genes *Pdgfrb*, *Angpt2* and *Notch3* (Fig. 6j). Activated pericytes also transcribed CD146 (*Mcam*) (Fig. 6j), which acts as a co-receptor to PDGFRβ during the inductive phase of BBB maturation to induce endothelial expression of tight junction proteins[80,81]. These data again suggest that, as opposed to a putative role in scar formation, brain pericytes instead drive capillary growth in an active zone of angiogenesis lining the inner side of the astroglial border. This angiogenic zone progressively reperfuses the ischemic region (Fig. 6k).

Hic1$^+$ cells promote BBB recovery after stroke

During developmental brain vessel maturation, pericytes are critically involved in stabilizing the nascent vessels, regulating vessel size and establishing the integrity of tight junctions of the BBB[28,37,79,82]. Therefore, we evaluated the BBB-promoting function of the proposed *Hic1*$^+$ brain SPC population at later time points, 21 days after stroke in the peri-infarct area after revascularization had occurred (Fig. 7a). The region was identified by its location and high proportion of EdU$^+$ cells that were found surrounding blood vessels (Extended

Fig. 7 | Pericytes promote BBB recovery after post-stroke revascularization. **a**, Graphical illustration of the experimental timeline. Shown are data obtained 21 days after stroke (except **b**: 10 days after stroke). **b**, In the revascularized tissue outside the infarct core, pericytes had regained a perivascular thin-strand ramification morphology. Of these pericytes, 36.0% ± 6.3% had incorporated EdU (arrowheads; *z*-depth on orthogonal view = 40 µm). **c**, In vivo images of the revascularized region 21 days after stroke show tdTomato$^+$ SPCs lining functional blood vessels (i.v. dextran-conjugated fluorescein). **d**, In the double transgenic *Hic1*^{CreERT2}; *Rosa26*$^{LSL\text{-}tdTomato}$; *Pdgfra*$^{tm11(EGFP)Sor}$/J mouse 21 days after stroke, perivascular fibroblasts (tdTomato$^+$/GFP$^+$, arrowheads) and pericytes (tdTomato$^+$/GFP$^-$, arrows) regained their location on larger arterioles and smaller capillaries, respectively. **e**, In the transgenic *Pdgfra*^{creERT2}; *Rosa26*$^{LSL\text{-}tdTomato}$ mouse (lineage tracing of fibroblasts) 21 days after stroke, fibroblasts are found in the lesion and perivascular fibroblasts are found along large vessels (arrowhead) but not alongside new capillaries. **f**, Feature plots showing no enrichment of transcripts of neuron-specific, microglia-specific, astrocyte-specific, endothelial-specific or oligodendrocyte-specific genes either in the resting or in activated SPCs. Data are expressed as log-normalized counts. **g**, 21 days after stroke, BBB integrity is reestablished in the revascularized region. Evans blue (961 Da) leakage is observed in the remaining infarct core but not in revascularized cortical tissue. **h**, 21 days after stroke, leakage of i.v.-injected 70-kDa dextran-conjugated fluorescein (arrowhead) was observed in the remaining infarct, but not in the revascularized region. ($n = 6$; data are presented as mean values ± s.e.m., *t*-test, $P = 0.0004$). **i**, 21 days after stroke, leakage of i.v.-injected 1-kDa cadaverine was observed and quantified. A significant reduction in leakage was found when comparing the remaining infarct and the adjacent revascularized region. ($n = 3$, data are presented as mean values ± s.e.m., *t*-test). **j**, 21 days after stroke, VE-cadherin activity patterning was analyzed in the previously ischemic area (next to the remaining stroke core) and compared to age-matched control mice. No significant differences were found indicating intact VE-cadherin junctions. The patches are blindly classified as 1 (stable), 2 (a singular break), 3 (presence of a VE-cadherin tuft) or 4 (multiple breaks within one patch of a singular vessel). $^{***}P < 0.001$.

https://doi.org/10.1038/s41593-025-01872-y

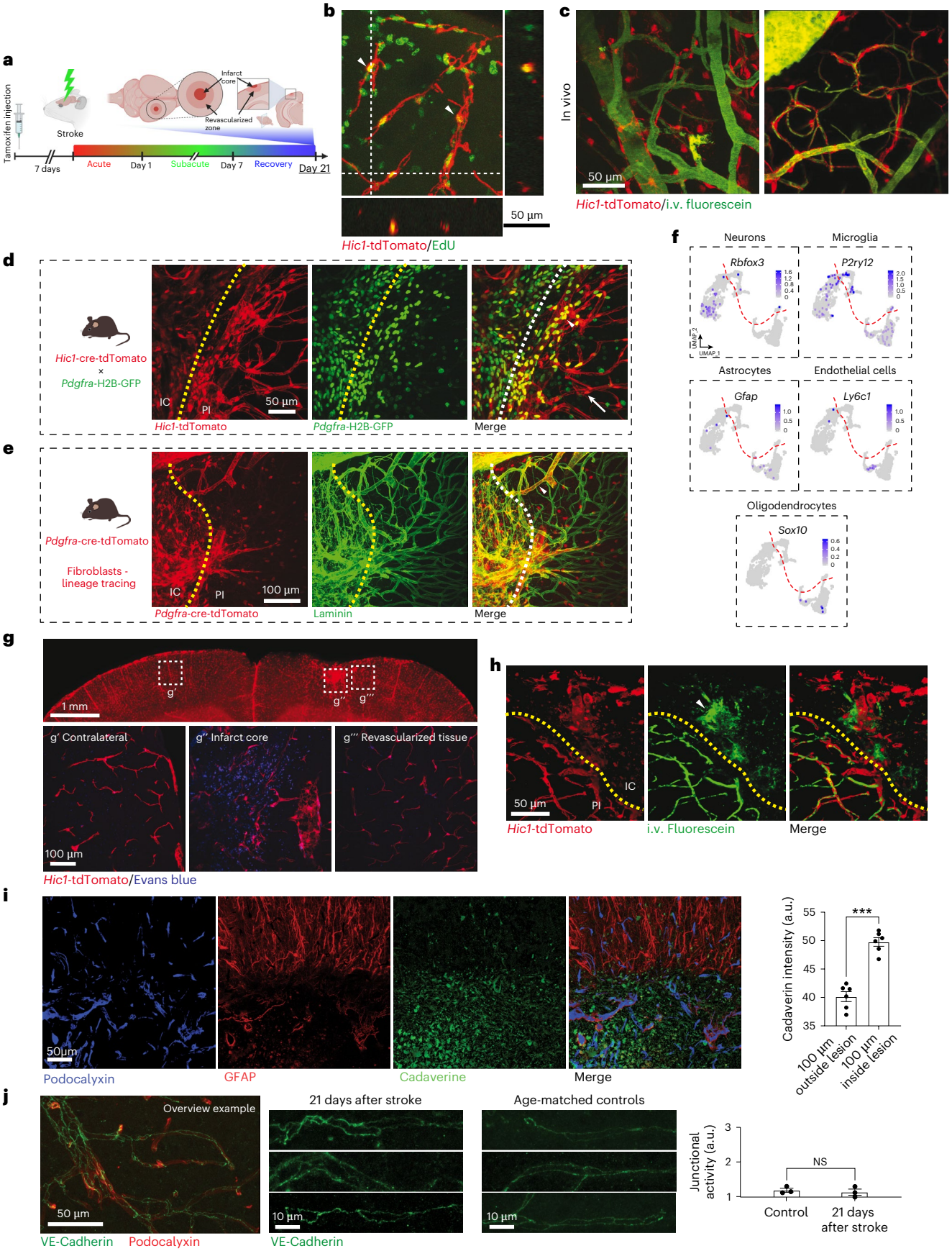

Data Fig. 10a). In this area, pericytes and perivascular fibroblasts had assumed a resting morphology, showing circular processes on arterioles and thin-strand processes along capillaries, respectively (Fig. 7b–d). Within these perivascular *Hic1*-tdTomato$^+$ cells, 36.0% were EdU$^+$, indicating they represent *Hic1*$^+$ cell progeny that ultimately associate with functional microvessels and integrate into a maturing neurovascular unit after transitioning from an activated phenotype (imaged at day 10 after stroke, following daily EdU injections; Fig. 7b). The location of SPCs along the functional vessels 21 days after stroke seemed similar to the distribution in control conditions, and SPC vessel detachment was only observed near areas where blood flow was disrupted (Fig. 7c). Using the double transgenic *Hic1*^{CreERT2}*;Rosa26*$^{LSL\text{-}tdTomato}$*;Pdgfra*$^{tm11(EGFP)Sor}$/J mouse, we observed perivascular fibroblasts along larger vessels and *Hic1*-tdTomato$^+$/*Pdgfra*-H2B-GFP$^-$ pericytes along capillaries in the revascularized area (Fig. 7d). Using a lineage tracing mouse to specifically follow the fate of all fibroblast populations, including perivascular fibroblasts (*Pdgfra*^{creERT2}*;Rosa26*$^{LSL\text{-}tdTomato}$), we observed tdTomato$^+$ perivascular fibroblast progeny on large vessels. However, our observations provided no evidence for the differentiation of *Pdgfra*$^+$ fibroblasts into capillary pericytes within the 21 days after stroke investigated here, further suggesting both populations remain distinct following activation and injury (Fig. 7e). Although proliferation of *Hic1*$^+$ pericytes and perivascular fibroblasts was readily observed after stroke, no evidence of multipotency into non-pericyte/venular SMCs or nonperivascular fibroblast cells was detected, extending recent in vivo observations[83]. This was corroborated by a lack of transcripts for other lineages including neurons, microglia/macrophages, astrocytes, ECs or oligodendrocytes as identified by scRNA-seq of *Hic1* lineage cells after stroke (Fig. 7f and Extended Data Fig. 10b). To investigate BBB integrity and potential differences in junction tightness, we performed i.v. injections of dyes with different sizes. Firstly, the relatively large dye Evans blue (961 Da) was injected i.v., and we observed no leakage from regenerated vessels lined with mature pericytes indicating that the BBB was intact (Fig. 7g and Extended Data Fig. 10c,d). In contrast, an expected local extravasation of Evans blue as well as of i.v.-injected 70-kDa dextran-conjugated fluorescein was observed from immature vessels in the active angiogenic zone (Fig. 7g,h and Extended Data Fig. 10c,d). To test whether smaller dyes might be able to cross the BBB, we next injected cadaverine (1 kDa) and found similar results with prominent leakage being detected in the stroke core but significantly less in the revascularized area directly surrounding the stroke core (Fig. 7i). As these results indicate a restoration of the BBB, we next evaluated ongoing tight junction activity, which can also be observed during development and is indicative of BBB integrity. VE-cadherin patterning was analyzed in the revascularized area 21 days after stroke. We observed that formed VE-cadherin junctions after stroke were stable and not significantly different from those in age-matched wild-type controls (Fig. 7j). This suggests that the new pericytes and perivascular fibroblasts can associate with new vessels to promote the maturation of a functional BBB. In development, appearance of astrocytic endfeet wrapping capillaries represents one of the last steps toward BBB integrity. In the revascularized tissue surrounding the remaining stroke lesion, the astrocytic endfoot coverage appeared normal 21 days after stroke (Extended Data Fig. 9a).

Discussion

Stroke remains a major cause of morbidity and although recent restorative therapies show promise in extending the therapeutic window for recovery, a better understanding of how endogenous remodeling of the cerebrovasculature is coordinated might reveal therapeutic targets. Our comprehensive dataset spanning baseline and post-injury conditions reveals that pericytes, venular SMCs and perivascular fibroblasts together form a niche of adult brain-resident SPCs. Using a new transgenic tool to follow the fate of *Hic1*-expressing precursor cells specialized in remodeling stromal tissue, we show here that both pericytes and perivascular fibroblasts accumulate in the ischemic area to coordinate stromal regeneration in the adult brain by activating angiogenic and fibrogenic programs, respectively. We uncover a transient angiogenic profile of injury-activated pericytes that recapitulates their contribution to developmental vascularization. Importantly, our in-depth description of the transcriptional signatures of stroke-activated pericytes and perivascular fibroblasts is publicly available via a searchable online database and reveals key signaling pathways that may be harnessed to improve cerebrovascular regeneration.

In all organs, recovery from injury relies on rebuilding the stroma, or connective tissue forming the tissue's scaffold, as a necessary step for subsequent parenchymal and functional restoration. Peripheral organs possess multiple types of stromal compartments around nerves, blood vessels, ducts, tendon or supporting connective tissue. These compartments harbor reservoirs of stromal (or mesenchymal) progenitors that give rise to various cells of mesenchymal lineage upon injury and orchestrate multiple aspects of the regenerative program[11,14,15]. Within the brain, however, the only stromal compartment lies in the perivascular space surrounding vessels of the intricate cerebrovascular system. Stromal regeneration in the brain is, therefore, not only necessary for structural recovery but also vital for revascularization of ischemic tissue. Discrepancies have been reported regarding the regenerative potential of brain pericytes in that in vitro culture studies suggested they behave as multipotent stem cells[11,84–86], whereas in vivo it was reported that pericytes exhibited limited lineage potential[83]. Using the pan-SPC marker gene *Hic1*, we demonstrate that a continuum of pericytes and venular SMCs as well as a more distinct group of perivascular fibroblasts, are key SPC subpopulations in the adult brain. The high degree of transcriptional similarity observed here between pericytes and venular SMCs is in accordance with previous reports showing two distinct subclasses of mural cells: one group of arterial/arteriolar SMCs, and another group composed of a continuum of pericytes and venular SMCs. Interestingly, our results show that after injury, SPC progenies stemming from the pericyte/venular SMC continuum behave as one homogeneous group of activated cells retaining pericyte markers and functions, suggesting that post-injury response may be a key differentiating factor between the two subclasses of mural cells. Following injury, the SPCs behave as progenitors by entering a transient amplification stage and modifying their phenotype to contribute to stroma regeneration but, importantly, retain their respective cellular identities and do not contribute to other non-SPC lineages.

Our findings indicate that stromal remodeling drives two distinct processes following stroke: one where pericytes promote angiogenesis and the formation of nascent blood vessels, and one where perivascular fibroblasts drive the formation of a fibrotic scar. Revascularization is a critical step to support tissue regeneration as restored blood flow is required to provide the oxygen and nutrients needed for implantation of parenchymal neural cells. Thus, promoting an angiogenic program that is partially driven by pericytes may heighten potential graft-based therapies after stroke. On the other hand, scar formation appears to be promoted by perivascular fibroblast progeny. While scar formation can be detrimental to CNS recovery by inhibiting axonal growth, glial and fibrotic scars also play an important structural role to spatially and temporally seal a lesion site[77,87,88]. Consequently, a balance needs to exist between pro-angiogenic and profibrotic signals for proper tissue repair and regeneration. We were able to show that injury-activated pericyte and fibroblast phenotypes provide this balance in brain tissue. It is important to note that because the photothrombotic stroke model used here induces severe ischemic injury within a large area of the cortex, the relative responses of pericytes and fibroblasts may be different in smaller vascular blockade or microstrokes, where the scar formation response is modest.

On one side of that balance, we show that bona fide pericytes can modify their functional and transcriptional phenotype to promote post-injury angiogenesis. Within 7 to 10 days after stroke, pericyte

recruitment and coverage of newly organized vascular structures was observed to go hand in hand with ECs and multiple markers of angiogenesis. This pericyte–EC association occurred before functional blood flow recovery, in a spatiotemporal pattern highly similar to that recently observed in the neonatal brain by the Shih group[40]. During development (postnatal day (P) 8 to P12), capillary growth originates strictly from ascending venules[40]. Remarkably, the post-stroke angiogenesis drive we observed stems from the pool of SPCs located (at rest) on the capillary-to-venule aspect of the arterio–venular tree, raising the interesting possibility that location cues are maintained in adulthood and regulate SPC post-injury functions. We show that only capillary and venular SPCs (pericytes/venular SMCs) retain the ability to activate an angiogenic program, while arteriolar SPCs (perivascular fibroblasts) activate a fibrogenic program. Furthermore, our transcriptomic analysis reveals that several pathways involved in vessel development are active in stroke-associated pericytes. Important components of pericyte–EC signaling such as *Pdgfrb*, *Angpt2*, *Notch3* and *Mcam* have been shown to be necessary for the inductive phase of vessel maturation as well as BBB induction during development[27,29,81,89]. These markers are transcribed at appreciable levels (and enriched relative to perivascular fibroblast progeny) in the post-stroke angiogenic pericyte population uncovered here.

Interestingly, the SCENIC toolbox offers additional insights into the inferred transcription factor activity that lies upstream, driving the global activated pericyte phenotype. Regulons driven by transcription factors such as *Mef2a* and *Mef2c* were more active in the stroke-associated pericytes, and *Mef2*-dependent transcription has been shown to be involved in several angiogenic mechanisms[90]. On the other hand, *Foxf2* activity was specific to pericytes, but its activity was downregulated in the stroke-associated pericytes. Interestingly, *Foxf2*-null mice exhibit more numerous, proliferative brain pericytes[91]. Silencing of *Foxf2*-controlled gene transcription may, therefore, partially underlie the transient proliferative pericyte phenotype observed early after injury. Overall, the spatiotemporal pattern of cell–cell communication observed during post-stroke recovery and the transcription of pro-angiogenic signaling pathways after stroke suggests that pericytes reactivate the phenotype and functional roles they exhibited during embryonic and neonatal vasculogenesis[92].

The angiogenic role of pericytes after injury contrasts with the scar-forming role of perivascular fibroblasts. At rest, the *Hic1*$^+$/*Pdgfra*$^+$ SPC subpopulation of perivascular fibroblasts was located mainly on pial and descending arterioles, and could be identified by *Col1a1*, *Col1a2* and *Slc1a3* transcription, as observed before[13,44,46,54,93]. The fact that scar formation is driven by perivascular fibroblasts and not pericytes appears common to multiple CNS injuries, as qualitatively similar results were obtained in experimental autoimmune encephalomyelitis[93], spinal cord injury, traumatic brain injury, middle cerebral artery occlusion and glioblastoma[13,44,46], albeit with different cell-type nomenclature. These commonalities in the functional response of CNS perivascular fibroblasts to injury likely extend to the transcriptional features driving their fibrogenic program. Therefore, the transcriptomic signature of a transient stroke-activated phenotype we describe here (complete and searchable scRNA-seq database available on our ISNAP portal; https://isnap.rossilab.dev/GSE146930/) likely shares features with other injury/disease paradigms and will help disentangle the identity and function of perivascular fibroblasts.

As would be expected from scar-forming cells, stroke-associated fibroblasts that were tdTomato$^+$ and, therefore, progeny of *Hic1*$^+$ perivascular fibroblasts showed increased transcription of ECM components involved in scarring, in particular fibrillar collagens (types I, III, V and others), proteoglycans and fibronectin[94,95]. Transcription of tissue inhibitor of metalloproteinases-1 and -2 (TIMP1, TIMP2), known to promote fibrosis after peripheral organ injury by inhibiting matrix metalloproteases and ECM degradation[96,97], were also found enriched in stroke-activated fibroblasts (*Timp1*, *Timp2*; Extended Data Fig. 10e). Increased activity of several transcription factors is required to promote a fibrogenic program. *Runx1* was highly active in the stroke-associated fibroblast population, and has been linked to scar formation in various organs[58,98,99]. *Creb3l1* was also highly transcribed in stroke-associated perivascular fibroblast progeny and is known to induce a profibrotic gene set in fibroblasts and induce collagen transcription[100,101]. Moreover, in an interesting cross-talk between both stroke-activated SPC populations, activated pericytes upregulate transcription of PDGF-A (*Pdgfa*), a ligand for PDGFRα that drives fibroblast activation (Extended Data Fig. 10e)[102].

Therefore, we propose that after injury, a balance exists between the two activated brain SPC populations where pericytes promote revascularization and perivascular fibroblasts support fibrogenesis. Previous reports suggested that pericytes themselves participate in scar formation[13,45,46,50]. While both populations share many commonalities, as evidenced by their shared expression of *Hic1*, our data suggest they differ in their roles after injury, whereas the scar-forming program is mostly supported by progenies of perivascular fibroblasts, and not those of pericytes. The identification of pericytes versus other mural cells has long been a matter of debate. The use of models relying on the expression of PDGFRβ, GLAST or NG2 has yielded results suggestive of a fibrogenic role of pericytes; however, our data and those of others show that these tools are not specific to pericytes. *Pdgfrb*, although enriched in pericytes, is also transcribed in perivascular fibroblasts and SMCs. Concomitant expression of NG2 (*Cspg4*) by oligodendrocyte progenitor cells, known to also activate following stroke, can confound interpretation[69]. Although the well-known GLAST (*Slc1a3*) expression in astrocytes can be distinguished from mural cells based on morphology and location, we show that among *Hic1*$^+$ SPCs, it is almost exclusively transcribed in the perivascular fibroblast population that becomes fibrogenic after stroke. Importantly, we show that GLAST$^-$ pericytes also activate following injury and retain functions distinct from those of activated GLAST$^+$ fibroblasts.

In conclusion, we have shown that pericytes, venular SMCs and perivascular fibroblasts form a major pool of stromal progenitors in the adult brain, where they play a critical role in the regeneration of cerebral blood vessels after injury. Following initial death within the ischemic zone, pericytes proliferate with a pro-angiogenic transcriptional profile and repopulate the stroke core near the outer astroglial border where they associate with ECs. Perivascular fibroblasts on the other hand promote scar formation by depositing ECM components. Together, brain SPCs participate in a progressive front of angiogenesis that paves the way for functional cerebrovascular regeneration in the peri-lesion area. We believe the ability of pericytes to activate and recapitulate their developmental role represents a key aspect in the initiation of brain regeneration after stroke.

Online content

Any methods, additional references, Nature Portfolio reporting summaries, source data, extended data, supplementary information, acknowledgements, peer review information; details of author contributions and competing interests; and statements of data and code availability are available at https://doi.org/10.1038/s41593-025-01872-y.

References

1. Carmichael, S. T. Cellular and molecular mechanisms of neural repair after stroke: making waves. *Ann. Neurol.* **59**, 735–742 (2006).
2. Lo, E. H. A new penumbra: transitioning from injury into repair after stroke. *Nat. Med.* **14**, 497–500 (2008).
3. Gotz, M. & Bocchi, R. Neuronal replacement: concepts, achievements, and call for caution. *Curr. Opin. Neurobiol.* **69**, 185–192 (2021).
4. Kempermann, G. et al. Human adult neurogenesis: evidence and remaining questions. *Cell Stem Cell* **23**, 25–30 (2018).

5. Gage, F. H. & Temple, S. Neural stem cells: generating and regenerating the brain. *Neuron* **80**, 588–601 (2013).
6. Zhang, R. et al. Activated neural stem cells contribute to stroke-induced neurogenesis and neuroblast migration toward the infarct boundary in adult rats. *J. Cereb. Blood Flow Metab.* **24**, 441–448 (2004).
7. Arvidsson, A., Collin, T., Kirik, D., Kokaia, Z. & Lindvall, O. Neuronal replacement from endogenous precursors in the adult brain after stroke. *Nat. Med.* **8**, 963–970 (2002).
8. Jin, K. et al. Evidence for stroke-induced neurogenesis in the human brain. *Proc. Natl Acad. Sci. USA* **103**, 13198–13202 (2006).
9. Xing, C., Hayakawa, K., Lok, J., Arai, K. & Lo, E. H. Injury and repair in the neurovascular unit. *Neurol. Res.* **34**, 325–330 (2012).
10. Liman, T. G. & Endres, M. New vessels after stroke: postischemic neovascularization and regeneration. *Cerebrovasc. Dis.* **33**, 492–499 (2012).
11. Crisan, M. et al. A perivascular origin for mesenchymal stem cells in multiple human organs. *Cell Stem Cell* **3**, 301–313 (2008).
12. Feng, J., Mantesso, A., De Bari, C., Nishiyama, A. & Sharpe, P. T. Dual origin of mesenchymal stem cells contributing to organ growth and repair. *Proc. Natl Acad. Sci. USA* **108**, 6503–6508 (2011).
13. Goritz, C. et al. A pericyte origin of spinal cord scar tissue. *Science* **333**, 238–242 (2011).
14. Scott, R. W., Arostegui, M., Schweitzer, R., Rossi, F. M. V. & Underhill, T. M. Hic1 defines quiescent mesenchymal progenitor subpopulations with distinct functions and fates in skeletal muscle regeneration. *Cell Stem Cell* **25**, 797–813 (2019).
15. Soliman, H. et al. Pathogenic potential of Hic1-expressing cardiac stromal progenitors. *Cell Stem Cell* **26**, 205–220 (2020).
16. Ozen, I., Boix, J. & Paul, G. Perivascular mesenchymal stem cells in the adult human brain: a future target for neuroregeneration? *Clin. Transl. Med.* **1**, 30 (2012).
17. Joe, A. W. et al. Muscle injury activates resident fibro/adipogenic progenitors that facilitate myogenesis. *Nat. Cell Biol.* **12**, 153–163 (2010).
18. Kramann, R. et al. Perivascular Gli1$^+$ progenitors are key contributors to injury-induced organ fibrosis. *Cell Stem Cell* **16**, 51–66 (2015).
19. Mendez-Ferrer, S. et al. Mesenchymal and haematopoietic stem cells form a unique bone marrow niche. *Nature* **466**, 829–834 (2010).
20. Uezumi, A., Fukada, S., Yamamoto, N., Takeda, S. & Tsuchida, K. Mesenchymal progenitors distinct from satellite cells contribute to ectopic fat cell formation in skeletal muscle. *Nat. Cell Biol.* **12**, 143–152 (2010).
21. Worthley, D. L. et al. Gremlin 1 identifies a skeletal stem cell with bone, cartilage, and reticular stromal potential. *Cell* **160**, 269–284 (2015).
22. Zhou, B. O., Yue, R., Murphy, M. M., Peyer, J. G. & Morrison, S. J. Leptin-receptor-expressing mesenchymal stromal cells represent the main source of bone formed by adult bone marrow. *Cell Stem Cell* **15**, 154–168 (2014).
23. Covas, D. T. et al. Multipotent mesenchymal stromal cells obtained from diverse human tissues share functional properties and gene-expression profile with CD146$^+$ perivascular cells and fibroblasts. *Exp. Hematol.* **36**, 642–654 (2008).
24. Schwab, K. E. & Gargett, C. E. Co-expression of two perivascular cell markers isolates mesenchymal stem-like cells from human endometrium. *Hum. Reprod.* **22**, 2903–2911 (2007).
25. Murphy, M. M., Lawson, J. A., Mathew, S. J., Hutcheson, D. A. & Kardon, G. Satellite cells, connective tissue fibroblasts and their interactions are crucial for muscle regeneration. *Development* **138**, 3625–3637 (2011).
26. Soliman, H. et al. Multipotent stromal cells: one name, multiple identities. *Cell Stem Cell* **28**, 1690–1707 (2021).
27. Armulik, A., Genove, G. & Betsholtz, C. Pericytes: developmental, physiological, and pathological perspectives, problems, and promises. *Dev. Cell* **21**, 193–215 (2011).
28. Daneman, R., Zhou, L., Kebede, A. A. & Barres, B. A. Pericytes are required for blood-brain barrier integrity during embryogenesis. *Nature* **468**, 562–566 (2010).
29. Sweeney, M. D., Ayyadurai, S. & Zlokovic, B. V. Pericytes of the neurovascular unit: key functions and signaling pathways. *Nat. Neurosci.* **19**, 771–783 (2016).
30. Faal, T. et al. Induction of mesoderm and neural crest-derived pericytes from human pluripotent stem cells to study blood-brain barrier interactions. *Stem Cell Rep.* **12**, 451–460 (2019).
31. Grant, R. I. et al. Organizational hierarchy and structural diversity of microvascular pericytes in adult mouse cortex. *J. Cereb. Blood Flow Metab.* **39**, 411–425 (2019).
32. Berthiaume, A. A. et al. Dynamic remodeling of pericytes in vivo maintains capillary coverage in the adult mouse brain. *Cell Rep.* **22**, 8–16 (2018).
33. Hartmann, D. A. et al. Pericyte structure and distribution in the cerebral cortex revealed by high-resolution imaging of transgenic mice. *Neurophotonics* **2**, 041402 (2015).
34. Bell, R. D. et al. Pericytes control key neurovascular functions and neuronal phenotype in the adult brain and during brain aging. *Neuron* **68**, 409–427 (2010).
35. Peppiatt, C. M., Howarth, C., Mobbs, P. & Attwell, D. Bidirectional control of CNS capillary diameter by pericytes. *Nature* **443**, 700–704 (2006).
36. Hall, C. N. et al. Capillary pericytes regulate cerebral blood flow in health and disease. *Nature* **508**, 55–60 (2014).
37. Armulik, A. et al. Pericytes regulate the blood-brain barrier. *Nature* **468**, 557–561 (2010).
38. Obermeier, B., Daneman, R. & Ransohoff, R. M. Development, maintenance and disruption of the blood-brain barrier. *Nat. Med.* **19**, 1584–1596 (2013).
39. Hellstrom, M., Kalen, M., Lindahl, P., Abramsson, A. & Betsholtz, C. Role of PDGF-B and PDGFR-beta in recruitment of vascular smooth muscle cells and pericytes during embryonic blood vessel formation in the mouse. *Development* **126**, 3047–3055 (1999).
40. Coelho-Santos, V., Berthiaume, A. A., Ornelas, S., Stuhlmann, H. & Shih, A. Y. Imaging the construction of capillary networks in the neonatal mouse brain. *Proc. Natl Acad. Sci. USA* https://doi.org/10.1073/pnas.2100866118 (2021).
41. Sun, J. et al. Transplantation of hPSC-derived pericyte-like cells promotes functional recovery in ischemic stroke mice. *Nat. Commun.* **11**, 5196 (2020).
42. Rust, R. et al. Anti-Nogo-A antibodies prevent vascular leakage and act as pro-angiogenic factors following stroke. *Sci Rep.* **9**, 20040 (2019).
43. Shimauchi-Ohtaki, H. et al. The dynamics of revascularization after white matter infarction monitored in Flt1-tdsRed and Flk1-GFP mice. *Neurosci. Lett.* **692**, 70–76 (2019).
44. Dias, D. O. et al. Pericyte-derived fibrotic scarring is conserved across diverse central nervous system lesions. *Nat. Commun.* **12**, 5501 (2021).
45. Dulauroy, S., Di Carlo, S. E., Langa, F., Eberl, G. & Peduto, L. Lineage tracing and genetic ablation of ADAM12$^+$ perivascular cells identify a major source of profibrotic cells during acute tissue injury. *Nat. Med.* **18**, 1262–1270 (2012).
46. Dias, D. O. et al. Reducing pericyte-derived scarring promotes recovery after spinal cord injury. *Cell* **173**, 153–165 (2018).
47. Hesp, Z. C. et al. Proliferating NG2-cell-dependent angiogenesis and scar formation alter axon growth and functional recovery after spinal cord injury in mice. *J. Neurosci.* **38**, 1366–1382 (2018).

48. Birbrair, A. et al. Type-1 pericytes accumulate after tissue injury and produce collagen in an organ-dependent manner. *Stem Cell Res. Ther.* **5**, 122 (2014).
49. Shibahara, T. et al. Pericyte-mediated tissue repair through PDGFRbeta promotes peri-infarct astrogliosis, oligodendrogenesis and functional recovery after acute ischemic stroke. *eNeuro* https://doi.org/10.1523/ENEURO.0474-19.2020 (2020).
50. Picoli, C. C. et al. Pericytes act as key players in spinal cord injury. *Am. J. Pathol.* **189**, 1327–1337 (2019).
51. Klement, W. et al. A pericyte-glia scarring develops at the leaky capillaries in the hippocampus during seizure activity. *Epilepsia* **60**, 1399–1411 (2019).
52. Attwell, D., Mishra, A., Hall, C. N., O'Farrell, F. M. & Dalkara, T. What is a pericyte? *J. Cereb. Blood Flow Metab.* **36**, 451–455 (2016).
53. Rajan, A. M., Ma, R. C., Kocha, K. M., Zhang, D. J. & Huang, P. Dual function of perivascular fibroblasts in vascular stabilization in zebrafish. *PLoS Genet.* **16**, e1008800 (2020).
54. Bonney, S. K., Sullivan, L. T., Cherry, T. J., Daneman, R. & Shih, A. Y. Distinct features of brain perivascular fibroblasts and mural cells revealed by in vivo two-photon imaging. *J. Cereb. Blood Flow Metab.* **42**, 966–978 (2022).
55. Dorrier, C. E., Jones, H. E., Pintaric, L., Siegenthaler, J. A. & Daneman, R. Emerging roles for CNS fibroblasts in health, injury and disease. *Nat. Rev. Neurosci.* https://doi.org/10.1038/s41583-021-00525-w (2021).
56. Adams, K. L. & Gallo, V. The diversity and disparity of the glial scar. *Nat. Neurosci.* **21**, 9–15 (2018).
57. Bradbury, E. J. & Burnside, E. R. Moving beyond the glial scar for spinal cord repair. *Nat. Commun.* **10**, 3879 (2019).
58. Abbasi, S. et al. Distinct regulatory programs control the latent regenerative potential of dermal fibroblasts during wound healing. *Cell Stem Cell* **27**, 396–412 (2020).
59. Fernandez-Klett, F. et al. Early loss of pericytes and perivascular stromal cell-induced scar formation after stroke. *J. Cereb. Blood Flow Metab.* **33**, 428–439 (2013).
60. Montagne, A. et al. Pericyte degeneration causes white matter dysfunction in the mouse central nervous system. *Nat. Med.* **24**, 326–337 (2018).
61. Vanlandewijck et al. A molecular atlas of cell types and zonation in the brain vasculature. *Nature* **554**, 475–480 (2018).
62. He, L. et al. Analysis of the brain mural cell transcriptome. *Sci Rep.* **6**, 35108 (2016).
63. Zeisel, A. et al. Molecular architecture of the mouse nervous system. *Cell* **174**, 999–1014 (2018).
64. Zeisel, A. et al. Brain structure. Cell types in the mouse cortex and hippocampus revealed by single-cell RNA-seq. *Science* **347**, 1138–1142 (2015).
65. Soderblom, C. et al. Perivascular fibroblasts form the fibrotic scar after contusive spinal cord injury. *J. Neurosci.* **33**, 13882–13887 (2013).
66. Stuart, T. et al. Comprehensive integration of single-cell data. *Cell* **177**, 1888–1902 (2019).
67. Aibar, S. et al. SCENIC: single-cell regulatory network inference and clustering. *Nat. Methods* **14**, 1083–1086 (2017).
68. Almad, A., Sahinkaya, F. R. & McTigue, D. M. Oligodendrocyte fate after spinal cord injury. *Neurotherapeutics* **8**, 262–273 (2011).
69. Zhang, R., Chopp, M. & Zhang, Z. G. Oligodendrogenesis after cerebral ischemia. *Front. Cell Neurosci.* **7**, 201 (2013).
70. Roth, M. et al. Regulator of G-protein signaling 5 regulates the shift from perivascular to parenchymal pericytes in the chronic phase after stroke. *FASEB J.* **33**, 8990–8998 (2019).
71. Ozen, I. et al. Loss of regulator of G-protein signaling 5 leads to neurovascular protection in stroke. *Stroke* **49**, 2182–2190 (2018).
72. Stratman, A. N., Malotte, K. M., Mahan, R. D., Davis, M. J. & Davis, G. E. Pericyte recruitment during vasculogenic tube assembly stimulates endothelial basement membrane matrix formation. *Blood* **114**, 5091–5101 (2009).
73. Lendahl, U., Nilsson, P. & Betsholtz, C. Emerging links between cerebrovascular and neurodegenerative diseases-a special role for pericytes. *EMBO Rep.* **20**, e48070 (2019).
74. Fu, X. et al. Specialized fibroblast differentiated states underlie scar formation in the infarcted mouse heart. *J. Clin. Invest.* **128**, 2127–2143 (2018).
75. Mutsaers, S. E., Bishop, J. E., McGrouther, G. & Laurent, G. J. Mechanisms of tissue repair: from wound healing to fibrosis. *Int. J. Biochem. Cell Biol.* **29**, 5–17 (1997).
76. Schmalfeldt, M., Bandtlow, C. E., Dours-Zimmermann, M. T., Winterhalter, K. H. & Zimmermann, D. R. Brain derived versican V2 is a potent inhibitor of axonal growth. *J. Cell Sci.* **113**, 807–816 (2000).
77. Anderson, M. A. et al. Astrocyte scar formation aids central nervous system axon regeneration. *Nature* **532**, 195–200 (2016).
78. Sofroniew, M. V. Molecular dissection of reactive astrogliosis and glial scar formation. *Trends Neurosci.* **32**, 638–647 (2009).
79. Armulik, A., Abramsson, A. & Betsholtz, C. Endothelial/pericyte interactions. *Circ. Res.* **97**, 512–523 (2005).
80. Chen, J. et al. CD146 is essential for PDGFRbeta-induced pericyte recruitment. *Protein Cell* **9**, 743–747 (2018).
81. Chen, J. et al. CD146 coordinates brain endothelial cell-pericyte communication for blood-brain barrier development. *Proc. Natl Acad. Sci. USA* **114**, E7622–E7631 (2017).
82. Gerhardt, H. & Betsholtz, C. Endothelial-pericyte interactions in angiogenesis. *Cell Tissue Res.* **314**, 15–23 (2003).
83. Guimaraes-Camboa, N. et al. Pericytes of multiple organs do not behave as mesenchymal stem cells in vivo. *Cell Stem Cell* **20**, 345–359 (2017).
84. Dore-Duffy, P., Katychev, A., Wang, X. & Van Buren, E. CNS microvascular pericytes exhibit multipotential stem cell activity. *J. Cereb. Blood Flow Metab.* **26**, 613–624 (2006).
85. Greenhalgh, S. N., Iredale, J. P. & Henderson, N. C. Origins of fibrosis: pericytes take centre stage. *F1000Prime Rep.* **5**, 37 (2013).
86. Sakuma, R. et al. Brain pericytes serve as microglia-generating multipotent vascular stem cells following ischemic stroke. *J. Neuroinflammation* **13**, 57 (2016).
87. Silver, J. & Miller, J. H. Regeneration beyond the glial scar. *Nat. Rev. Neurosci.* **5**, 146–156 (2004).
88. Rolls, A., Shechter, R. & Schwartz, M. The bright side of the glial scar in CNS repair. *Nat. Rev. Neurosci.* **10**, 235–241 (2009).
89. Liu, H., Zhang, W., Kennard, S., Caldwell, R. B. & Lilly, B. Notch3 is critical for proper angiogenesis and mural cell investment. *Circ. Res.* **107**, 860–870 (2010).
90. Sacilotto, N. et al. MEF2 transcription factors are key regulators of sprouting angiogenesis. *Genes Dev.* **30**, 2297–2309 (2016).
91. Reyahi, A. et al. Foxf2 is required for brain pericyte differentiation and development and maintenance of the blood–brain barrier. *Dev. Cell* **34**, 19–32 (2015).
92. Biswas, S., Cottarelli, A. & Agalliu, D. Neuronal and glial regulation of CNS angiogenesis and barriergenesis. *Development* https://doi.org/10.1242/dev.182279 (2020).
93. Dorrier, C. E. et al. CNS fibroblasts form a fibrotic scar in response to immune cell infiltration. *Nat. Neurosci.* **24**, 234–244 (2021).
94. Ricard-Blum, S., Baffet, G. & Theret, N. Molecular and tissue alterations of collagens in fibrosis. *Matrix Biol.* **68-69**, 122–149 (2018).
95. Zollinger, A. J. & Smith, M. L. Fibronectin, the extracellular glue. *Matrix Biol.* **60-61**, 27–37 (2017).

96. Sa, Y., Li, C., Li, H. & Guo, H. TIMP-1 induces alpha-smooth muscle actin in fibroblasts to promote urethral scar formation. *Cell. Physiol. Biochem.* **35**, 2233–2243 (2015).
97. Mann, C. J. et al. Aberrant repair and fibrosis development in skeletal muscle. *Skelet. Muscle* **1**, 21 (2011).
98. Kim, W. et al. RUNX1 is essential for mesenchymal stem cell proliferation and myofibroblast differentiation. *Proc. Natl Acad. Sci. USA* **111**, 16389–16394 (2014).
99. Koth, J. et al. Runx1 promotes scar deposition and inhibits myocardial proliferation and survival during zebrafish heart regeneration. *Development* https://doi.org/10.1242/dev.186569 (2020).
100. Yamamoto, A. et al. Transcription factor old astrocyte specifically induced substance is a novel regulator of kidney fibrosis. *FASEB J.* **35**, e21158 (2021).
101. Chen, Q., Lee, C. E., Denard, B. & Ye, J. Sustained induction of collagen synthesis by TGF-beta requires regulated intramembrane proteolysis of CREB3L1. *PLoS ONE* **9**, e108528 (2014).
102. Andrae, J., Gallini, R. & Betsholtz, C. Role of platelet-derived growth factors in physiology and medicine. *Genes Dev.* **22**, 1276–1312 (2008).

Methods

Experimental model and mouse details

Mice. *Hic1*$^{nLacZ/+}$ were used to analyze the location of *Hic1*-expressing cells in the brain. *Hic1*^{CreERT2} mice were crossed to B6.Cg-Gt(ROSA)26Sor$^{tm14(CAG-tdTomato)Hze}$/J (Ai14 line, JAX stock 007914, herein referred to as *Rosa26*$^{LSL-tdTomato}$) to generate *Hic1*^{CreERT2};*Rosa26*$^{LSL-tdTomato}$ mice for lineage tracing. To induce Cre-ERT2 nuclear translocation, timed TAM injections were used (described below) leading to tdTomato expression in *Hic1*$^{+}$ cells. This approach leads to the stable and indelible expression of tdTomato in all quiescent *Hic1*$^{+}$ SPC populations and their derivatives. Three additional mouse lines were used in this study: (1) *Hic1*^{CreERT2};*Rosa26*$^{LSL-tdTomato}$ were crossed to B6.129S4-*Pdgfra*$^{tm11(EGFP)}$Sor/J (*Pdgfra*$^{H2b-EGFP/+}$; JAX stock 007669, herein referred to as *Pdgfra*-H2B-GFP) mice to create *Hic1*^{CreERT2};*Rosa26*$^{LSL-tdTomato}$; *Pdgfra*-H2B-GFP knock-in mice to differentiate and trace SPC subpopulations. (2) *Hic1*^{CreERT2} were crossed with B6.129P2-Gt(ROSA)26Sor$^{tm1(DTA)Lky}$/J (JAX stock 009669, herein referred to as *Rosa26*^{DTA}) to generate *Hic1*^{CreERT2};*Rosa26*^{DTA} mice used as described below to induce timed SPC deletion. (3) For lineage tracing of fibroblasts, B6.129S-*Pdgfra*$^{tm1.1(cre/ERT2)Blh}$/J (JAX stock 032770) were crossed with B6.Cg-Gt(ROSA)26Sor$^{tm14(CAG-tdTomato)Hze}$/J (Ai14 line, JAX stock 007914) to generate *Pdgfra*^{creERT2};*Rosa26*$^{LSL-tdTomato}$ mice. All mouse lines were maintained on a C57BL/6J background. Male and female mice at the age of 2–5 months were used. All mice were group housed under pathogen-free conditions (12-h light–dark cycle) and provided food and water ad libitum. All experimental procedures were performed in accordance with Canadian Council on Animal Care regulations and German veterinary office regulations (for the state of Hessen) and were approved by the local authorities for animal experimentation (Regierungspräsidium Darmstadt, Germany), with protocols approved by the University of British Columbia committee on animal care. Animals received photothrombotic stroke as described below and remained in their home cage until the respective time point (day 1, 4, 7, 8, 14, 21 or 40 after stroke) was reached.

Method details

TAM injections. Heterozygous *Hic1*^{CreERT2};*Rosa26*$^{LSL-tdTomato}$ mice were injected with TAM (Sigma-Aldrich, T5648, 25 mg ml^{-1}, intraperitoneal injections of 100 µl per day) dissolved in sunflower or peanut oil for 5 consecutive days to induce expression of the reporter. Throughout the course of TAM injection, mice were closely monitored for any adverse reactions to the treatment. To induce timed SPC deletion, *Hic1*^{CreERT2};*Rosa26*^{DTA} transgenic mice were used. TAM (Sigma-Aldrich, T5648, 25 mg ml^{-1}, intraperitoneal injections of 100 µl per day) was injected for 14 consecutive days to achieve targeted *Hic1*$^{+}$ cell deletion before i.v. injection of Evans blue (as described below).

Photothrombotic stroke. We used Rose Bengal-induced photothrombosis to obtain targeted ischemia in *Hic1*^{CreERT2};*Rosa26*$^{LSL-tdTomato}$, *Hic1*^{CreERT2};*Rosa26*$^{LSL-tdTomato}$; *Pdgfra*-H2B-GFP and *Pdgfra*^{creERT2};*Rosa26*$^{LSL-tdTomato}$ mice. Using this approach, light-induced production of reactive oxygen species triggers coagulation in the targeted brain region. To achieve this, we anesthetized the animal initially with 3% isoflurane and lowered the dose to 1.5% to maintain anesthesia. The body temperature was maintained at 37 °C using a heating pad with a feedback regulator from a rectal temperature probe. A small incision was made and the skin retracted in order to reveal the skull area covering the somatosensory cortex. Rose Bengal dye was injected intraperitoneally (0.1 mg per gram mouse body weight diluted to 10 mg ml^{-1} in 0.9% NaCl saline). To target vessels in an area of ~1.5 mm, a custom-built laser beam from a diode-pumped laser (Beta Electronics, MGM-20) was used (wavelength of 530 nm). Photoactivation was performed for 20 min to ensure maximum blockage of targeted vessels. After completion, the skin was sutured to cover the skull and animals were monitored until they were fully awake. For longitudinal in vivo imaging experiments, the laser illumination was performed through the cranial window and through a 1.5-mm pinhole to restrict the laser beam (11 mW/cm^2). Animals were then single housed and imaged on days 1, 4, 7, 21 and 40, and brains were subsequently collected for analysis.

Cranial window surgery. For cranial windows, *Hic1*^{CreERT2};*Rosa26*$^{LSL-tdTomato}$ mice were anesthetized using a three-component mix (fentanyl, 0.05 mg per kg body weight; midazolam, 5 mg per kg body weight; medetomidine, 0.5 mg per kg body weight) and a cranial window of 4 mm in diameter was placed on the somatosensory cortex as previously described[103]. In brief, the anesthetized animals were head-fixed in a modified stereotactic frame (Stoelting, 51731) while placed on a feedback-controlled heating pad. An approximately 4-mm circle was drilled into the skull surface. Using a forceps, the piece of skull was removed taking care not to irritate or puncture the dura mater. A sterile round glass coverslip (Warner Instruments no. 1, thickness of 0.13 mm, 4 mm in diameter) was lowered until it was parallel and flush with the edge of the skull by use of a modified micromanipulator. The coverslip was sealed to the skull with dental composite (Venus Flow, Heraeus Kulzer) and a custom-made titanium ring was sealed on top of the coverglass to headfix the mouse. After surgery, animals were injected with an antidote (flumazenil, 0.5 mg per kg body weight; atipamezol, 2.5 mg per kg body weight) and closely monitored until they were fully awake.

Two-photon in vivo imaging. In vivo imaging was performed on anesthetized *Hic1*^{CreERT2};*Rosa26*$^{LSL-tdTomato}$ mice (1.5% isoflurane, Sigma, 792632) using a custom-built, fully motorized, two-photon microscope coupled to a Coherent Chameleon Ultra II laser. Images were acquired with a Zeiss W Plan-Apochromat ×40/numerical aperture 1.0 objective. A custom-built titanium ring was used to secure the mice by fitting the ring into a head fixation apparatus specifically designed to allow for relocation of previously imaged ROIs with high precision. Full motorization of the microscope is provided by a Sutter MP285 via ScanImage (version 3.8). Image acquisition via non-descanned detectors (Hamamatsu, GaAsP PMT, H10770PA-40) included the following fluorophores: tdTomato using an excitation of 920 nm, and 70-kDa dextran-conjugated fluorescein (Sigma, 46945, 25 mg ml^{-1}) acquired at 800 nm of excitation wavelength separated by emission filters (ET525/50m-2P and ET605/70m-2P, Chroma Technology). Images were collected approximately 50–150 µm from the cortical surface with a volume of 100 µm using two-line averaging, 1,024 × 1,024 pixels and a step size of 1–2 µm in the *z* axis between optical sections. Laser power was kept constant for each experiment and did not exceed 45 mW. In each mouse, 1–2 ROIs within the core of the ischemic lesion and 3–5 regions in the peri-infarct area were imaged. Images at different days following stroke were acquired in different animals with acute cranial windows installed immediately before imaging to maintain cranial integrity during the stroke recovery process. For in vivo SPC tracking over multiple hours, animals where anesthetized with three-component mix (fentanyl, 0.05 mg per kg body weight; midazolam, 5 mg per kg body weight; medetomidine, 0.5 mg per kg body weight) and images of four ROIs (peri-infarct area and ischemic core) were taken every 60 min for 6 h, immediately after installation of an acute cranial window.

Optical coherence tomography in vivo imaging. Functional blood flow imaging was performed additionally by label-free OCT using a Thorlabs OCT Telesto-II imaging system. A-scans were captured, and a variance image was obtained to visualize blood flow. Images shown are *z*-projected stacks of 600 µm in thickness with a *z* pixel size of 3.44 µm. Longitudinal imaging of the same region was obtained using the cranial window with head fixation as described above. Animals were anesthetized initially with 3% of isoflurane and the dose lowered to 1.5% to maintain anesthesia and positioned under the imaging system using a custom-built head fixation system. The body temperature

was maintained at 37 °C using a heating pad with a feedback regulator from a rectal temperature probe. Blood flow of all cortical layers was recorded at indicated time points. Imaged ROIs were imaged in intervals of 1, 4, 7, 14 and 21 days to observe revascularization and functional blood flow.

Ex vivo imaging. Imaging of 300-µm-thick slices was performed using a Coherent Chameleon Ultra II laser coupled to a two-photon scanning microscope (Zeiss LSM 7MP) with a Zeiss ×20 W/1.0 NA objective. Stacks of varying thickness (30 to 200 µm) were acquired using 16-line averaging, 1,024 × 1,024 pixels and stepping 2 µm in the *z* axis between optical sections. Images were shown as maximal projections obtained with ImageJ (National Institutes of Health) or three-dimensional renderings obtained from Zen imaging software (Zeiss). The following fluorophores were imaged: tdTomato, excitation wavelength (EW) 1,020 nm, filter settings (FS) ET630/75 m; 70-kDA dextran-conjugated fluorescein, EW 1,020 nm or 750 nm, FS ET520/60 m; FITC EW 1,020 nm or 750 nm, FS ET520/60 m; DAPI, EW 740 nm, FS ET455/50 m; Evans blue (Sigma, E2129), EW 850 nm, FS ET455/50 m; 1-kDa Alexa Fluor 555 cadaverine (Invitrogen, A30677) EW 555 nm, FS ET604/26 nm; EdU click it Alexa-647, EW 810 nm, FS ET660/80 m; Alexa Fluor 488-conjugated antibodies, EW 750 nm, FS ET520/60 m; NeuroTrace fluoro-Nissl dye 500/525 (Invitrogen, N21480), EW 1,000 nm, FS ET520/60 m. Immunohistochemically labeled 40-µm-thick sections were imaged using a Leica TCS SP5 confocal microscope with a HC PL Fluotar ×10/0.3 NA and HCX PL APO CS ×40/1.3 NA objective. Sections (100 µm in thickness) were imaged using a Leica TCS SP5 or a Leica SP8 confocal microscope. For the Leica SP5 confocal microscope with a HC PL APO ×20/0.7 NA, a HCX PL APO CS ×40/1.3 NA or a HCX PL APO CS ×63/1.4 NA Oil objective, the following fluorophores were imaged: Alexa 488, EW 488 nm, FS 498-541 nm, tdTomato, EW 561 nm, FS 573-618 nm and Alexa 647, EW 633 nm, FS 761-800 nm.

For the Leica SP8 confocal microscope with a HC FLUOTAR L ×25/0.95 NA W objective, the following fluorophores were imaged: Alexa 488, EW 488 nm, FS 508-546 nm, tdTomato, EW 561 nm, FS 577-619 nm; and for Alexa 647, EW 633 nm, FS 659-689 nm.

To obtain fluorescence images with a wider field of view, some coronal slices were also imaged using a Zeiss Axio ZoomV16 macroscope with a Plan-NEOFLUAR Z ×2.3/1.5 NA objective.

Acute slice preparation and maintenance. *Hic1*^{CreERT2};*Rosa26*$^{LSL\text{-}tdTomato}$ mice were anesthetized with 3% isoflurane and decapitated. The brains were removed immediately and placed in ice-cold artificial cerebrospinal fluid (ACSF) solution including the following components: 120 mM *N*-methyl-D-glucamine, 2.5 mM KCL, 25 mM $NaHCO_3$, 1 mM $CaCl_2$, 7 mM $MgCl_2$, 1.2 mM NaH_2PO_4, 2 mM D-glucose, 2.4 mM sodium pyruvate and 1.3 mM sodium L-ascorbate. The solution was constantly oxygenated with 95% O_2 and 5% CO_2. Brains were transferred into a vibratome (Leica, VT1200S) containing the same solution and were sliced coronally with disposable razor blades (Conemco & Marviac) at a thickness of 300 µm. Subsequent incubation was done for 1 h in oxygenated ACSF. The ACSF contained the following: 126 mM NaCl, 2.5 mM KCl, 26 mM $NaHCO_3$, 2 mM $CaCl_2$, 2 mM $MgCl_2$, 1.25 mM NaH_2PO_4, 10 mM D-glucose (pH 7.3–7.4, osmolarity ~300 mOsm).

NeuroTrace fluorescent Nissl dye imaging. Acute slices of *Hic1*^{CreERT2};*Rosa26*$^{LSL\text{-}tdTomato}$ mice were incubated in oxygenated ACSF with NeuroTrace 500/525 (Invitrogen; 1:250 dilution) for 30 min, then washed out in oxygenated ACSF for 1–2 h before imaging under a two-photon microscope in a bath continuously perfused with ACSF. Incubations and imaging were performed at 32 °C.

Immunohistology

Thick brain sections. *Hic1*^{CreERT2};*Rosa26*$^{LSL\text{-}tdTomato}$, *Hic1*^{CreERT2};*Rosa26*$^{LSL\text{-}tdTomato}$;*Pdgfra*-H2B-GFP or *Pdgfra*^{creERT2};*Rosa26*$^{LSL\text{-}tdTomato}$ mice were perfused intracardially with 0.1 M phosphate-buffered saline (PBS) and 4% paraformaldehyde (PFA) according to the protocols approved by the University of British Columbia committee on animal care. Brains were additionally post-fixed overnight in 4% PFA. Slices were prepared as 300-µm-thick coronal sections. Slices were then immunolabeled free floating and each step was performed in 0.1 M PBS with 20% dimethylsulfoxide and 2% Triton X-100 as published[104]. Slices were blocked for 24 h using 10 % goat serum and subsequently incubated for 8 days using one of the listed primary antibodies (rabbit anti-Laminin (1:100 dilution), Abcam, 11575; rabbit anti-Collagen IV (1:500 dilution), Biodesign, T40251R; rabbit anti-NG2 (1:500 dilution), Thermo Fisher, PA5-17199) and 2.5% goat serum. After washings for 24 h, one of the listed secondary antibodies was applied and slices were incubated for 6 days in 2.5% goat serum. Slices were rinsed in 0.1 M PBS before they were mounted on custom-made microscope slides for imaging. Then, 300-µm-thick slices were imaged with a two-photon microscope[104].

Thin brain sections. Coronal brain sections (100 µm) were prepared using a vibratome (VT1200S, Leica) and stored in freezing solution (30% glycerol, 30% ethylene glycol, 10% 1 M PBS, 30% distilled water) at −20 °C until further processing. For immunohistochemistry experiments, sections were washed three times with 0.1 M PBS, followed by ice-cold methanol fixation at 4 °C for 30 min while shaking at 45 rpm on an orbital shaker. After another three washing steps of 0.1 M PBS each for 5 min, the sections were permeabilized using 0.5% Triton X-100 (in case of anti-CD105, anti-podocalyxin or anti-GFAP labeling) or 1% Triton X-100 (in case of anti-PDGFRβ labeling) in 0.1 M PBS for 1 h at room temperature (RT) followed by blocking with 5% donkey serum in 0.1 M PBS for 1 h at RT. The sections were then incubated with a primary antibody (rat anti-CD105 (endoglin), 1:1,000 dilution, Thermo Fisher 14-1051-82, goat anti-podocalyxin, 1:500 dilution, R&D Systems AF1556, goat anti-PDGFRβ, 1:500 dilution, Neuromics GT15065, CD31 (rat; 1:50 dilution), BD Pharmingen 557355, rabbit anti-GFAP, 1:1,000 dilution, Dako Z 0334, VE-Cadherin (rat, 1:50), BD Pharmingen 555289) in 0.1 M PBS overnight at 4 °C shaking at 45 rpm. After each antibody treatment, the sections were washed three times with 0.1 M PBS-Tween-20 (0.05%). The sections were incubated with the appropriate secondary antibody (donkey anti-rabbit 488, 1:1,000 dilution, Thermo Fisher, A21206; donkey anti-rat 488, 1:1,000 dilution, Thermo Fisher, A21208; donkey anti-goat 488, 1:1,000 dilution, Thermo Fisher, A11055; donkey anti-rabbit 647, 1:1,000 dilution, Thermo Fisher, A31573; or donkey anti-goat 647, 1:1,000 dilution, Thermo Fisher, A21447) for 2 h at RT shaking at 45 rpm. Isolectin GS-IB4 (Griffonia simplicifolia Alexa Fluor 488 conjugate, I21411; 1:200 dilution in 0.1 M PBS) was incubated for 2 h at RT. The sections were mounted on Superfrost Plus slides using Fluoromount-G. Subsequent imaging was performed using a Leica SP5 or SP8 confocal microscope. Cryosections (40 µm) were collected as free-floating coronal slices. Sections were incubated with blocking solution (10% normal goat serum and 0.4% Triton X-100 in PBS) followed by primary or secondary antibody incubations. Thin sections were imaged using a Leica TCS SP5 confocal microscope as described above.

LacZ staining. For in situ X-gal staining on histological sections, tissues were prepared in the following manner. Mice were terminally anesthetized by intraperitoneal injection of Avertin (tribromoethanol; 400 mg per kg body weight) and fixed by intracardial perfusion of cold PBS followed by cold LacZ fixative as previously described[105], before dissection and immersion of tissue samples in LacZ fixative for 3 h on ice. For cryosectioning, the above collected and fixed samples were washed with PBS then incubated through a cryoprotective series of sucrose solutions of increasing concentration from 10–50% for >3 h each before embedding into OCT compound (Tissue-Tek, 4583). Tissues were immersed into OCT in disposable plastic cryomolds (Polysciences, 18646A) and frozen in an isopentane bath cooled by liquid

nitrogen. Cryosections were cut (Leica, CM3050S) at a thickness of 6 µm and mounted onto Superfrost Plus slides (VWR, 48311-703). This material was used for LacZ staining. For detection of LacZ on sections, in situ LacZ staining with X-gal was carried out. Slides were thawed at RT, washed 3 × 10 min in PBS and then incubated overnight at 37 °C in a humidified chamber with the aforementioned X-gal staining solution. For additional immunofluorescence (IF) staining of LacZ-stained samples, freshly stained slides were subsequently washed with PBS for 3 × 5 min and IF staining was carried out as described above. For IF staining, slides were thawed at RT, washed 3 × 10 min in PBS and incubated for 1 h in PBS containing 10 mg ml^{-1} sodium borohydride (Sigma, 213462) to quench autofluorescence. Following this treatment, slides were washed with PBS and incubated in block solution containing 2.5% bovine serum albumin (BSA; Sigma, A7030) and 2.5% Goat serum (Gemini, 100-190) for 90 min at RT before incubation in primary antibody overnight at 4 °C. Alexa Fluor-conjugated secondary antibodies were diluted at a ratio of 1:500 and applied to the slides for 45 min. After each antibody incubation, 3 × 5 min PBS washes were performed and sections were counterstained with DAPI (600 nM) and mounted with Aqua Polymount (Polysciences, 18606).

Evans blue injection. For analysis of vessel permeability, 100 µl of Evans blue (Sigma, E2129, 1 mg ml^{-1}) was injected in the tail vein of *Hic1*^{CreERT2}*; Rosa26*$^{LSL\text{-}tdTomato}$ mice 30 min before perfusion of the mouse at the indicated time points. The brains were then sectioned into 300-µm-thick slices and imaged using two-photon microscopy as described above. To evaluate the effect of SPC deletion on vascular permeability, *Hic1*^{CreERT2}*; Rosa26*^{DTA} transgenic mice were injected with TAM as described above. On the last day of injection animals also received 20 mg per kg body weight Evans blue in PBS by intraperitoneal injection. Twenty-four hours later, animals were euthanized and perfused with 15 ml PBS followed by 4% PFA. The brains were removed and 2-mm coronal sections were prepared for analysis. To detect Evans blue extravasation, integrated fluorescence intensity at 700 nm was measured using a LiCor imaging system. Background autofluorescence at 800 nm was also collected. Results were compared to control *Hic1*^{CreERT2}*; Rosa26*$^{LSL\text{-}tdTomato}$ mice that received the same TAM treatment.

Dextran-conjugated fluorescein injection. For analysis of vessel permeability, 100 µl of 70-kDa dextran-conjugated fluorescein was injected in the tail vein and imaged in vivo through a cranial window and/or in 100/300-µm-thick slices. For slices, the brains of *Hic1*^{CreERT2}*; Rosa26*$^{LSL\text{-}tdTomato}$ mice were fixed by direct overnight incubation in 4% PFA (no perfusion was performed to preserve the location of fluorescein within the vessels). For FITC-conjugated gelatin experiments (Thermo Fisher, G13187), mice were perfused intracardially first with 0.1 M PBS and subsequently with 20 ml of a 10% fluorescein-conjugated-albumin gel (wt/vol) using a peristaltic pump set at a speed of 1 ml min^{-1}. During this procedure, the mouse was tilted head down on a custom-built platform. Curing of the gel was achieved after the perfusion by submerging the carcass in ice-cold water for 30 min. The brain was harvested and immersion-fixed in 4% PFA in PBS for 12 h and then sliced in 300-µm-thick sections for imaging.

Cadaverine injection. For analysis of vessel permeability, animals were injected with 70 µl of 1 kDa cadaverine delivered through the retro-orbital venous sinus. The dye circulated for 20 min. The mice were then perfused intracardially with 4% PFA. Brains were then post-fixed at RT for 2 h, and then transferred to 30% sucrose overnight. The brains were flash frozen and sectioned in 60-µm-thick slices for analysis. To quantify Alexa Fluor 555 cadaverine leakage, a mask was made of the anti-podocalyxin channel to exclude vessel-bound signal. The remaining mean fluorescence intensity was measured in a ROI spanning 100 µm out from and within the astroglial scar (peri-infarct area).

EdU incorporation experiments. To identify cells that have undergone DNA synthesis in vivo, we visualized EdU incorporation. Mice were given intraperitoneal injections of EdU (20 mg per kg body weight, in PBS) on a daily basis after the photothrombotic stroke. For longer periods, daily doses were 10 mg per kg body weight for 10 consecutive days. *Hic1*^{CreERT2}*; Rosa26*$^{LSL\text{-}tdTomato}$ or *Hic1*^{CreERT2}*; Rosa26*$^{LSL\text{-}tdTomato}$*; Pdgfra*-H2B-GFP mice were euthanized and perfused with 4% PFA 7 or 10 days after the photothrombotic stroke and the brains were removed and sliced into 300-µm-thick sections. EdU staining was conducted using Click-iT EdU imaging kit (Invitrogen, C10086). After two washing steps with 3% BSA) in PBS, the sections were permeabilized using 0.5% Triton X-100 in PBS for 20 min. After another two washing cycles with 3% BSA in PBS, the sections were incubated with a Click-iT reaction mix containing reaction buffer, $CuSO_4$, Alexa Fluor 647 and reaction buffer additive for 30 min protected from light. Subsequently, sections were washed with 3% BSA in PBS and imaged. DAPI was used to localize the nucleus of activated SPCs.

TTC staining. TTC (Sigma, T8877) staining was used to detect the size of ischemic area. TTC was dissolved in PBS at 2% and 800-µm-thick coronal brain slices were taken 24 h after stroke and incubated in TTC solution for 20 min at RT. Slices were imaged immediately.

CD105 (endoglin) intensity analysis. After imaging of 100-µm-thick sections as described above, maximum projections of tile *z*-stacks were analyzed using Fiji software (ImageJ). The lesion was identified by the glial scar (visible via GFAP immunoreactivity) and a ROI of the lesion drawn manually. This ROI was then expanded radially in 100-µm steps for subsequent analysis of CD105 in colocalization with podocalyxin to quantify the mean intensity within each ring-shaped ROI. Statistical analysis was performed with Prism 9.3.0 software (GraphPad) using ordinary one-way ANOVA with Dunnett's multiple-comparisons test (comparing each dataset to the −100 µm to 0 µm ROI).

Colocalization and contact area of fluorescence signals. After immunohistochemistry was performed as described above, images of 300-µm-thick brain sections of *Hic1*^{CreERT2}*; Rosa26*$^{LSL\text{-}tdTomato}$ were analyzed using Imaris 9.2 (Bitplane, Oxford Instruments) as a visualization and analysis tool. Colocalization of fluorescent markers was analyzed via the Imaris colocalization tool creating a separate overlapping channel of the fluorophores in question. Fluorophores included tdTomato, Alexa Fluor 488-conjugated secondary antibodies (for laminin, Col IV, CD31, PDGFRβ and NG2), DAPI and Neurotrace 500/525. For soma colocalization, the 'spot' recognition tool of Imaris was used to localize cell somata in the different fluorescent channels. Spots that colocalized within the same soma were then counted as double positive for their respective marker/dye. The 'surface to surface contact area' tool embedded in the MATLAB extension of Imaris was used to further analyze areas of contact between two neighboring but not necessarily overlapping fluorophores.

Quantification of vascular tree branching order. The filament tracing tool in Imaris 9.2 was used to trace vascular structures. The starting point was set to the primary point of entry into the brain and branching thereafter was automated via the Imaris filament tracing algorithm. A surface reconstruction was subsequently used to create a contact area for fluorescence signals associated to the vascular tree according to the respective branch orders. *Hic1*-tdTomato^{+}, *Pdgfra*-H2B-GFP^{+} somata in *Hic1*^{CreERT2}*; Rosa26*$^{LSL\text{-}tdTomato}$*; Pdgfra*-H2B-GFP mice were detected and analyzed using the spot recognition algorithm followed by a colocalization analysis. The 'surface to surface contact area' tool embedded in the MATLAB extension of Imaris was used to quantify the number of recognized double-positive somata that were associated to the surface reconstruction of the vascular tree according to their branching order.

Quantification of single-cell tracking in vivo. SPCs in *Hic1*^{CreERT2};*Rosa26*$^{LSL\text{-}tdTomato}$ mice were observed for 6 h using in vivo two-photon imaging as described above. Obtained images were analyzed using Imaris 9.2. Images were loaded in a time sequence and corrected for movement using the 'drift correction' algorithm of Imaris. Spot recognition was used to detect the center of mass on SPC somata. Spots were then automatically tracked over the time course of 6 h and speed (µm per hour) was calculated for all moving cells. Results were compared to SPC somata in uninjured tissue of the same animals imaged and analyzed in the same manner.

Quantification of lesion size over time. Analysis of lesion size over a time course of 21 days was performed on the maximum circumference of longitudinally acquired OCT images on days 1, 7 and 21 after stroke. For the tdTomato intensity analysis, intensity of each ROI (in arbitrary values before normalization) was compared to the uninjured contralateral ROI of the same slice, and significant differences were evaluated using a paired *t*-test.

Quantification of SPC and vessel volume. Maximum projections of tile *z*-stacks were analyzed using Fiji software (ImageJ). The ROI of the lesion was drawn manually. This ROI was then expanded radially in 100-µm steps outwards from the lesion and 100 µm inwards of the lesion border. 0 represents the lesion boarder itself; thus, the ROIs are moving outwards in the direction of healthy tissue. Subsequent analysis within each ring-shaped ROI was performed using the surface detection algorithm (Imaris 9.2), providing the respective volumes for the vessels (i.v. fluorescein) and SPCs (tdTomato). Single-cell volume was calculated by automatic soma detection based on cell morphology (Imaris 9.2), which was then divided by the overall volume calculated for each ring-shaped ROI. Overall volumes of the ring-shaped ROI were used to normalize all values within the given ROI. Statistical analysis was performed with Prism 9.3.0 software (GraphPad) using ordinary one-way ANOVA with Dunnett's multiple-comparisons test.

Quantification of VE-cadherin activity. For analysis of junctional activity, images of VE-cadherin were taken using a Leica TCS SP8 Multiphoton microscope with a ×63 objective using a zoom of 2.0 in 1,024 × 256-pixel format. The images were then processed, if necessary, to optimize the clarity of the signal. Using a script generously provided by the laboratory of A. Acker-Palmer (Goethe University), the VE-cadherin images were sectioned into 100 × 256-pixel patches, which were then randomized and presented for blinded classification. Analysis was performed in a ROI spanning 150 µm out from the astroglial scar (peri-infarct area). The patches are classified as 1 (stable), 2 (a singular break), 3 (presence of a VE-cadherin tuft) or 4 (multiple breaks within one patch of a singular vessel). After the patches are classified, the average of each animal is taken; the vasculature is considered stable when the average rating is ≤1.5.

Statistics and reproducibility

For all experimental conditions where a representative image is shown, experiments were repeated at least four times with similar results. No data were excluded from the analyses. For most experiments, the investigators were not blinded to allocation during experiments and outcome assessment. No statistical methods were used to predetermine sample sizes but our sample sizes are similar to those reported in previous publications and animal ethics consideration were taken into account. Animals and samples were randomly assigned to experimental groups. Data distribution was assumed to be normal but this was not formally tested.

FACS methodology

Brains from *Hic1*^{CreERT2};*Rosa26*$^{LSL\text{-}tdTomato}$ mice were dissected and immediately sliced into 800-µm-thick coronal slices using a Vibratome (Leica, VT1200S) as described above to improve visualization of the ischemic area. The ischemic area was dissected from four mice and pooled for FACS sorting. Contralateral hemispheres from four mice were also pooled separately. A razor was used to cut the brain tissue into <1-mm^3 pieces. Digestion buffer (1.5 ml) was added containing 1.5 U ml^{-1} Collagenase D (Roche, 11 088 882 001) and 2.4 U ml^{-1} Dispase II (Roche, 04 942 078 001) for 40 min. Digested material was subsequently triturated by pipetting and centrifuged at 963*g* for 5 min. Resuspended tissue (6 ml PBS) was again triturated by pipetting and passed through a 70-µm cell strainer. Tissue was resuspended in 37% Percoll and centrifuged at 963*g* for 20 min at RT. The separated myelin and Percoll were removed followed by 5 min of centrifugation at 390*g*. To enrich for tdTomato cells from this whole-brain suspension, cells were stained with a cocktail containing anti-Ter119-647d (AbLab, AB00000305; 1:200 dilution), anti- CD45-488 (AbLab, AB00000383; 1:1,000 dilution) and anti-CD31-APC (BD Pharmingen, 551262; 1:400 dilution). This mixture containing cells and antibodies was then incubated on ice for 20 min (in the dark). Afterwards, 3 ml FACS buffer was added to dilute the antibodies before centrifugation at 1,400 rpm for 5 min. Cells were resuspended in FACS buffer and centrifuged at 390*g* for 5 min. The pellet was resuspended in FACS buffer containing propidium iodide (PI) and Hoechst 33342 (Sigma, B2261) to a final concentration of 4 µM. Positively stained cells were then sorted using a BD Influx, and PI-negative, Hoechst-positive, and forward/side scatter parameters were used to identify viable single cells for all FACS enrichments. Sorted cells were collected into sort media (DMEM, 5% FBS) in cooled siliconized microcentrifuge tubes (Fisher Scientific, 02-681-320). For isolation of RNA, cells were microcentrifuged at 664*g* for 5 min with soft braking and the isolated cell pellet was lysed in RNAzol (Sigma, R4533).

Gene expression profiling—bulk RNA-seq

Brains were dissociated as described above and pooled before FACS sorting and bulk RNA-seq. Total RNA was isolated using RNAzol (Sigma, R4533) as per the manufacturer's instructions with some modifications: StepV.2.-linear polyacrylamide (GenElute, Sigma, 56575) was added as a carrier to the RNA solution before cold isopropanol was added. To support precipitation of total RNA, the samples were incubated overnight at −20 °C. Precipitated RNA was centrifuged at >12,000g for 30 min at 4 °C. SUPERase-IN RNase inhibitor (Thermo Fisher, AM2696) was added at a 1:20 ratio to the resuspended RNA solution. An Agilent Bioanalyzer 2100 RNA 6000 Nano chip (5067-1511) was used to test the sample integrity. RNA samples with a RNA Integrity Number > 8 were used to prepare libraries following the standard protocol for the TruSeq Stranded mRNA library kit (Illumina) on the Illumina Neoprep automated nanofluidic library prep instrument. Paired-end sequencing was performed on the Illumina NextSeq 500 High Output Kit. Illumina sequencing output-generated BCL files were de-multiplexed by bcl2fastq2. De-multiplexed read sequences were then aligned to the Mouse Genome mm10 reference sequence using the STAR (https://www.ncbi.nlm.nih.gov/pubmed/23104886/) aligner. Assembly and FPKM values were estimated using Cufflinks (http://cole-trapnell-lab.github.io/cufflinks/). Genes were ranked based on expression level.

Single-cell RNA-seq

Single-cell suspensions were generated as described for pop-RNA-seq with the following downstream modifications. CD45$^+$/tdTomato$^-$ and CD45$^-$/tdTomato$^+$ cells were separated and enriched by FACS sorting into 0.22-µm vacuum-filtered SC collection media (DMEM containing 5% FBS) with PI. Viable CD45$^+$/tdTomato$^-$ and CD45$^-$/tdTomato$^+$ target cells were subsequently further purified, and debris reduced by a second sort. Equal numbers of each target population were collected into the same 10 µl of SC collection media. Sorted CD45$^+$/tdTomato$^-$ cells were used as carrier cells with CD45$^-$/tdTomato$^+$ cells to increase the probability of successful cell capture for downstream single-cell RNA-seq protocols. Cells were counted and quality control

was determined by a hemocytometer. If results showed that >98% of visible objects were verified to be single cells, the suspension was put into a Chromium Controller (10x Genomics), and captured and library prepared with the Chromium single cell 3′ reagent kit v2 (10x Genomics). cDNA libraries were sequenced on a NextSeq 500 (Illumina) to a minimum depth of 50,000 reads per cell. Raw base call files were de-multiplexed into FASTQ files using the cellranger package (10x Genomics; version 2.2.0), specifically the 'cellranger mkfastq' pipeline. A transgenic reference genome was generated by the concatenation of the sequences for tdTomato to the mm10 reference genome and subsequent use of the 'cellranger mkref' pipeline. Alignment to the modified mm10 reference genome was performed using the cellranger count pipeline (10x Genomics). Graphical output was generated using the cellrangerRkit R package (10x Genomics). Gene-count matrices were processed and analyzed using the Seurat package (Satija Lab, version 3.1.2) in R. Preliminary clustering (see details below) was performed to identify barcodes corresponding to myeloid cells based on *Ptprc* (CD45), *Cx3cr1* and *P2ry12* expression. These cells were subsetted out, followed by quality control to remove cells expressing <200 genes and genes expressed in <3 cells. Additional quality control was performed based on sample features, including total genes expressed, total unique molecular identifiers and percentage mitochondrial counts to remove outliers, which may be low-quality cells and potential multiplets. Gene expression per cell was log normalized to a scale factor of 10,000. To minimize batch-associated differences in the visualization of data, datasets belonging to different batches of experimental preparation were integrated to preserve cells of similar biological state[66]. Expression of each gene in the integrated data was scaled to a mean and variance of zero and one, respectively. Scaled expression is used for heat maps and principal component analysis, which was conducted with the top 2,000 variable genes across all datasets. Louvain clustering was performed using the first 20 PCs. Visualization of data in low-dimensional space was achieved with UMAP. Similarities of annotated SPC populations were assessed by hierarchical clustering with Pearson's correlation across all genes. DEGs were computed using Wilcoxon's rank-sum test and values were adjusted using Bonferroni correction. Only genes expressed in at least 25% of each cluster were considered in the computation. To perform pathway enrichment analyses, all significant (adjusted P value < 0.05) and upregulated genes (log fold change > 0) were inputted into DAVID Bioinformatics Resources 6.8 to generate biological processes under the 'GO FAT' category[106]. Significant pathways were filtered based on adjusted P values (Benjamini–Hochberg correction). Using SCENIC (version 1.1.2-2), we reconstructed gene regulatory networks and inferred the activity of transcription factors characteristic to our scRNA-seq data. Default parameters and the mm9 RcisTarget database were adopted as outlined by the SCENIC vignette (https://github.com/aertslab/SCENIC/). The regulon activity matrix was appended to the Seurat object for visualization with feature plots. Hierarchical clustering with inferred activity was used to identify common regulatory programs shared across annotated populations[67].

Quantification and statistical analysis

Multiple mice were observed and analyzed as biological replicates. Animals (both male and female) were then used in different settings at these time points: For in vivo two-photon imaging, $n = 5$ animals were used for each time point. For in vivo tracing of cells over 6 h, $n = 5$ animals were used; displayed data points represent individual cells. For TTC imaging, $n = 4$ animals were used 24 h after photothrombosis. For optical coherence tomography, $n = 8$ mice were used longitudinally throughout the recovery process to assess lesion circumference over time and each was imaged before photothrombosis, immediately after and at days 1, 4, 7, 10, 14 and 21. For immunohistochemistry, $n = 5$ animals were used for each time point. For colocalization analysis with PDGFRβ and Hic1-tdTomato, $n = 3$ animals were used. For cadaverine injection, $n = 3$ animals were used. For VE-cadherin analysis, $n = 3$ animals were used. For analysis of SPCs at different time points before and after stroke, $n = 8$–10 animals were used for each time point. For fluorescein injection, $n = 4$ animals were used for each time point (days 1, 7 and 21 after stroke). For Evans blue injection, $n = 4$ animals were used for each time point (days 1, 7 and 21 after stroke). For acute slice preparation experiments, $n = 3$ mice were used. For EdU incorporation experiments, $n = 5$ mice were used for each time point (days 7 and 10 after stroke). For SPC deletion experiments using *Hic1*^{CreERT2};*Rosa26*^{DTA} mice, $n = 5$ mice were used. For FITC-conjugated gelatin injection, $n = 5$ were used. For quantification analysis and localization of *Hic1*-tdTomato^{+}/*Pdgfra*-H2B-GFP^{+} cells in comparison to *Hic1*-tdTomato^{+}/*Pdgfra*-H2B-GFP^{-} cells, $n = 3$ of *Hic1*^{CreERT2};*Rosa26*$^{LSL\text{-}tdTomato}$ X *Pdgfra*$^{tm11(EGFP)}$Sor/J were used in baseline conditions. At day 7 after stroke, $n = 3$ were used. For image acquisition of all *Pdgfra*$^{+}$ cells after stroke, $n = 4$ *Pdgfra*^{CreERT2};*Rosa26*$^{LSL\text{-}tdTomato}$ mice were used. To investigate *Hic1*-expressing cells in the brain, $n = 5$ Hic1$^{nLacZ/+}$ mice were used. For VE-cadherin activity analysis, $n = 3$ mice were used. For IB4 experiments, $n = 3$ mice were used. Graphs were compiled in GraphPad Prism 8 or R and show the mean ± s.e.m. unless indicated otherwise. For population sequencing $n = 4$ animals were used. For scRNA-seq using contralateral tissue and tissue from the ischemic core, $n = 8$–10 animals were used.

Reporting summary

Further information on research design is available in the Nature Portfolio Reporting Summary linked to this article.

Data availability

The complete sequencing data report included in this paper was deposited to the NCBI Sequence Read Archive (Gene Expression Omnibus GSE146930; BioProject accession number PRJNA608615). All raw and processed data will be made available upon request.

Due to the nature of our study, the raw data consist of large image files that require substantial storage capacity. Making these files publicly available presents technical limitations, as current publicly accessible repositories do not provide the necessary capacity to host such extensive datasets. However, we are committed to transparency and data accessibility. Therefore, we are happy to provide the raw data upon reasonable request to ensure that it can be accessed by interested researchers. Source data are provided with this paper.

References

103. Hefendehl, J. K. et al. Long-term in vivo imaging of beta-amyloid plaque appearance and growth in a mouse model of cerebral beta-amyloidosis. *J. Neurosci.* **31**, 624–629 (2011).
104. Dissing-Olesen, L. & MacVicar, B. A. Fixation and immunolabeling of brain slices: SNAPSHOT method. *Curr. Protoc. Neurosci.* **71**, 1.23.1–1.23.12 (2015).
105. Scott, R. W. & Underhill, T. M. Methods and strategies for lineage tracing of mesenchymal progenitor cells. *Methods Mol. Biol.* **1416**, 171–203 (2016).
106. Huang, D. W., Sherman, B. T. & Lempicki, R. A. Bioinformatics enrichment tools: paths toward the comprehensive functional analysis of large gene lists. *Nucleic Acids Res.* **37**, 1–13 (2009).

Acknowledgements

This work was supported by grants from the Fondation Leducq (15CVD02) and Canadian Institute for Health Research (FDN-148397 (to B.A.M.), PJT-148816, PJT-175102 (to T.M.U.), MOT-97856, MOT-137100 (to F.M.R.)) and Heart and Stroke Foundation (G-23-0034151 (to B.A.M.)). L.-P.B. was supported by CIHR Banting Fellowship, Heart and Stroke Foundation, Michael Smith Foundation for Health Research. J.K.H. was supported by a DFG Postdoctoral Fellowship, Michael Smith Foundation for Health Research, Emmy Noether Award (HE 6867/3-1), Alzheimer's Association (AARF-17-529810), SFB1531 (456687919). B.A.M. was supported by a Canada Research Chair in Neuroscience.

Author contributions

L.-P.B., J.K.H. and B.A.M. conceived and designed the study. L.-P.B. and J.K.H. performed ex vivo and in vivo imaging. L.-P.B. and L.W.T. performed transcriptomics analysis L.-P.B., R.W.S., L.W.T., C.-A.L., D.G. and H.S. performed and analyzed sequencing experiments. L.-P.B., J.K.H., C.-A.L., M.D., J.H. and L.D.-O. performed immunostaining. L.-P.B. and R.W.S. carried out X-gal staining and R.W.S. designed and analyzed the SPC ablation experiments. T.M.U. and R.W.S. generated the transgenic mice. L.P.B., J.K.H. and B.A.M. analyzed and interpreted the data. L.-P.B. wrote the manuscript. L.-P.B., J.K.H., R.W.S., L.W.T., C.-A.L., H.S., L.D.-O., J.H., F.M.R., T.M.U. and B.A.M. contributed to the editing of the manuscript.

Competing interests

The authors declare no competing interests.

Additional information

Extended data is available for this paper at https://doi.org/10.1038/s41593-025-01872-y.

Supplementary information The online version contains supplementary material available at https://doi.org/10.1038/s41593-025-01872-y.

Correspondence and requests for materials should be addressed to Louis-Philippe Bernier or Brian A. MacVicar.

Peer review information *Nature Neuroscience* thanks the anonymous reviewers for their contribution to the peer review of this work.

https://doi.org/10.1038/s41593-025-01872-y

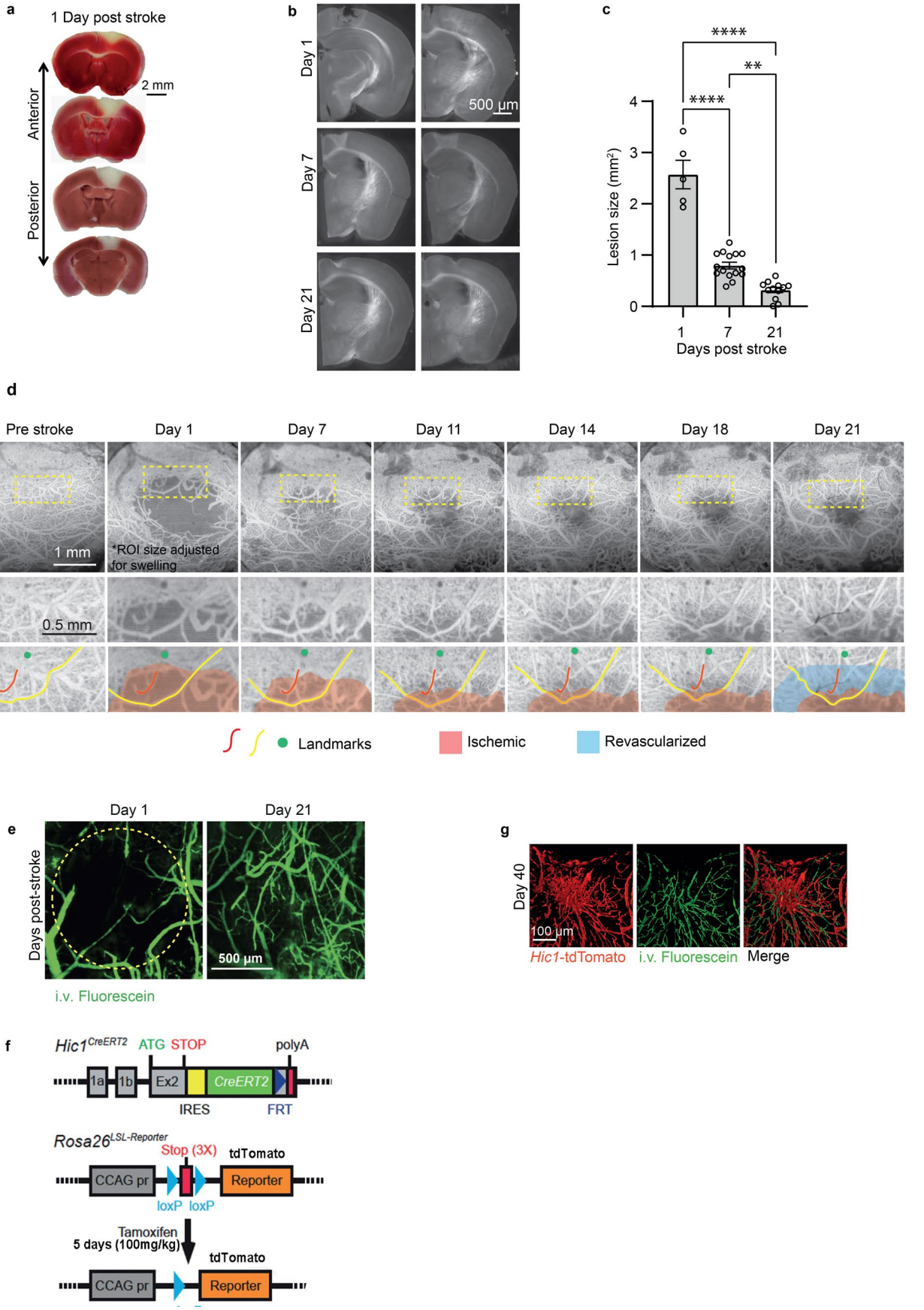

Extended Data Fig. 1 | See next page for caption.

https://doi.org/10.1038/s41593-025-01872-y

Extended Data Fig. 1 | Photothrombotic stroke in *Hic1*^{CreERT2};*Rosa26*$^{LSL\text{-}tdTomato}$ mice. a. TTC (2,3,5-triphenyltetrazolium chloride) staining of 800 µm-thick slices obtained 24 h after cortical photothrombosis showing the extent of the infarct. **b**. Brightfield images of 300 µm-thick coronal slices obtained with a Zeiss Axio Zoom microscope 1, 7 or 21 days after cortical photothrombosis showing a cross-section of the infarct area. **c**. Quantification of the cross-sectional area of the infarct zone obtained as in **b** (Data are presented as mean values +/- SEM. One-way ANOVA. **** < 0.0001; ** = 0.0011. Day 1, n = 5; Day 7, n = 15; Day 21, n = 12). **d**. Optical coherence tomography (longitudinal imaging before and after stroke at indicated time points) showing partial functional revascularization of the ischemic area 7-21 days following stroke. Landmarks (red and yellow line, green dot) indicate vessels that are visible throughout the recovery phase. Red and blue areas indicate the ischemic and revascularized areas. **e**. *In vivo* two-photon cortical images through a cranial window showing partial revascularization 21 days after stroke. Functional blood flow observed following i.v. 70-kDa dextran-conjugated fluorescein injection. **f**. Schematic diagram of the *Hic1*^{CreERT2} knock in allele and associated lineage-tracing strategy (*Rosa26*$^{LSL\text{-}tdTomato}$). **g**. In some mice, incomplete recovery is observed 40 days after cortical photothrombosis. When the previously ischemic cortical region was incompletely repaired after 40 days, accumulation of activated tdTomato$^+$ cells in *Hic1*^{CreERT2};*Rosa26*$^{LSL\text{-}tdTomato}$ mice was still observed. tdTomato$^+$ cells along with 70 kDa dextran-conjugated fluorescein injected i.v. show that some revascularization has taken place even within the area still populated with activated tdTomato$^+$ cells.

https://doi.org/10.1038/s41593-025-01872-y

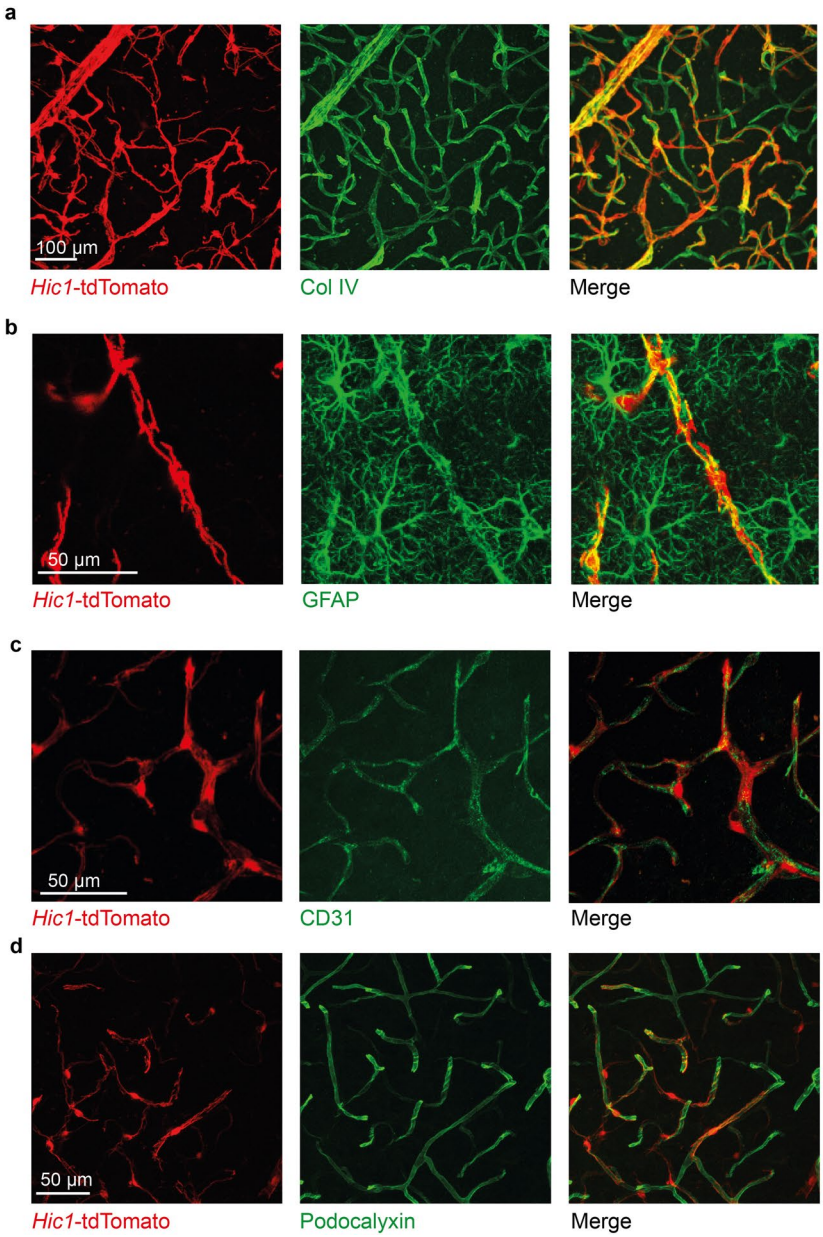

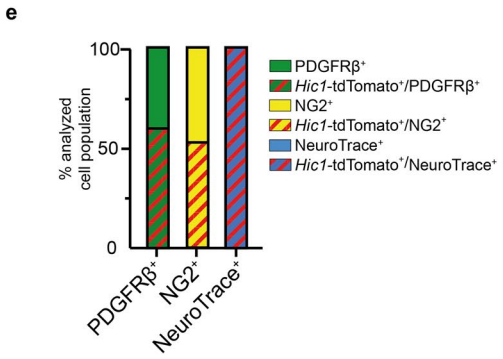

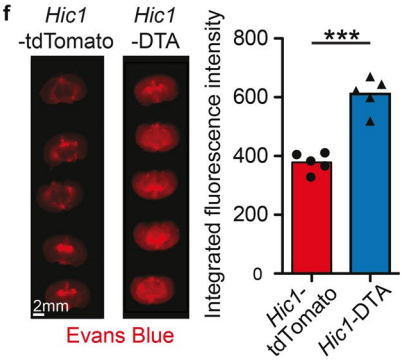

g Population RNA-seq - *Hic1*-tdTomato+ cells

*Rank out of 22,058 genes

Rank*	Gene	FPKM	Rank*	Gene	FPKM
1	*Vtn*	12565.7	272	*Mcam*	311.237
3	*Igfbp7*	4222.23	308	*Vim*	281.532
4	*Mgp*	4076.03	309	*Lum*	280.271
30	*Rgs5*	1475.69	311	*Coch*	277.448
41	*Ptn*	1150.37	319	*Moxd1*	271.995
54	*Ndufa4l2*	1015.54	328	*Abcc9*	265.929
61	*Kcnj8*	982.345	346	*Col1a1*	255.54
64	*Dcn*	937.516	402	*Notch3*	220.058
72	*Higd1b*	885.036	405	*Anpep*	219.155
80	*Pdgfrb*	835.426	410	*Serpinf1*	217.612
82	*Ifitm1*	805.755	544	*Des*	164.807
96	*Serpinh1*	700.222	571	*Zic1*	158.314
161	*Cd248*	488.205	603	*Cspg4*	150.711

Extended Data Fig. 2 | *Hic1*-tdTomato$^+$ cells within the neurovascular unit. **a**. Maximal projection image of Col IV (green) showing colocalization with tdTomato$^+$ cells. **b**. Maximal projection image of tdTomato$^+$ cells in close association with astrocytic endfeet, observed with GFAP staining. **c**. Maximal projection image of tdTomato$^+$ cells in close association with endothelial cells, observed with CD31 staining. **d**. Maximal projection image of tdTomato$^+$ cells in close association with endothelial cells, observed with Podocalyxin staining. **e**. Quantification of colocalization between tdTomato$^+$ cells and other known markers/dyes for pericytes (PDGFRβ, NG2, NeuroTrace 500/525) in the cell somata of all analysed cells. **f**. Ablation of *Hic1*$^+$ cells results in BBB dysfunction as Evans Blue leakage is observed following tamoxifen-dependent DTA expression in *Hic1*$^+$ cells in the *Hic1*^{CreERT2};*Rosa26*^{DTA} model (n = 5; p < 0.0001). **g**. Bulk- RNA-seq of tdTomato$^+$ cells show transcription of genes that were previously described as pericyte and perivascular fibroblast markers.

https://doi.org/10.1038/s41593-025-01872-y

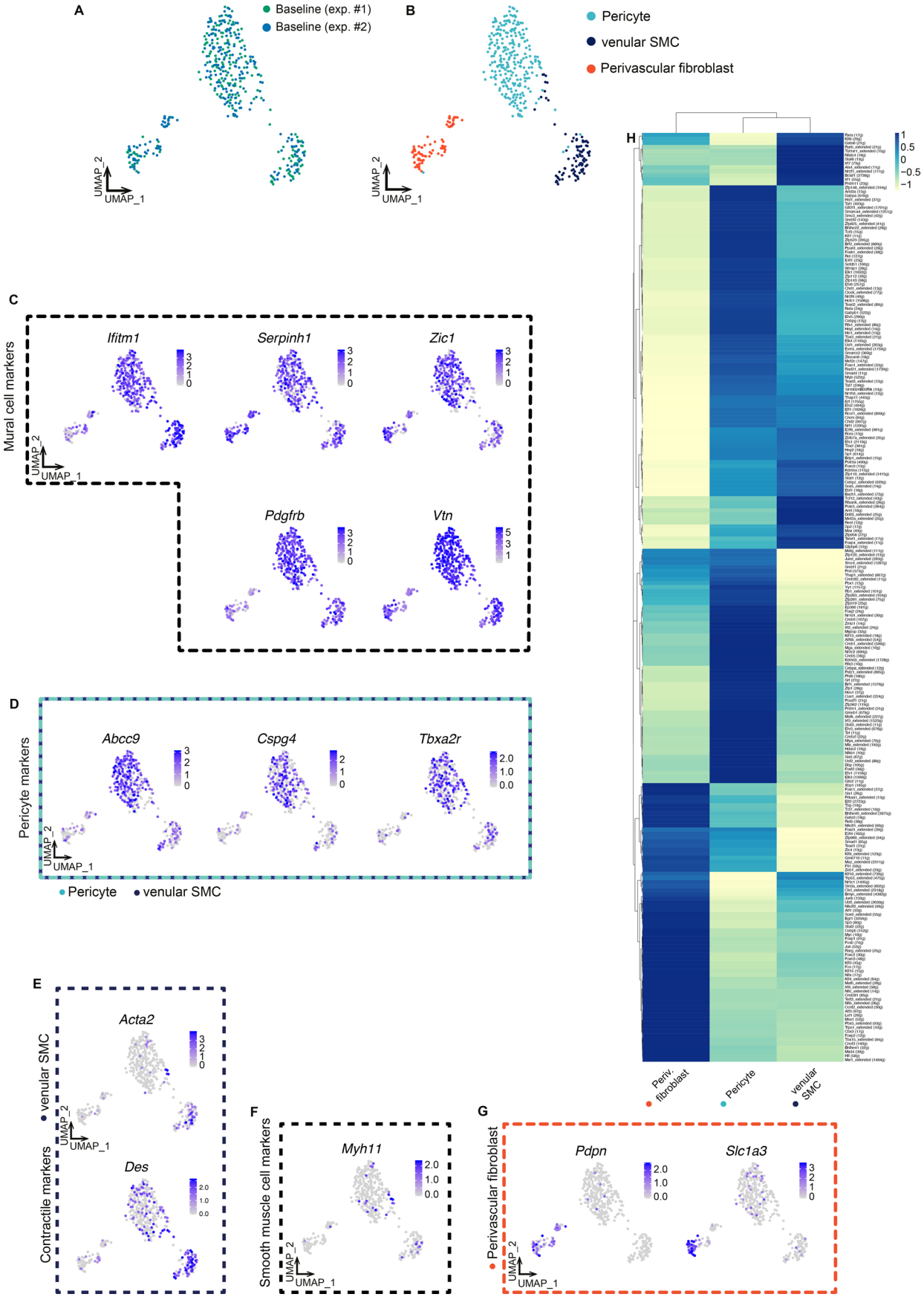

Extended Data Fig. 3 | See next page for caption.

https://doi.org/10.1038/s41593-025-01872-y

Extended Data Fig. 3 | Transcriptional profile of baseline pericytes, venular SMC and perivascular fibroblasts. a. Two individual sets of experiments including individual sample collection of tissue of *Hic1*^{CreERT2};*Rosa26*$^{LSL\text{-}tdTomato}$ *mice*. UMAP plots of integrated experiments display similar clustering pattern (colours indicate the individual sequencing experiments). **b**. Single-cell RNA sequencing of tdTomato^{+} cells collected from uninjured brain hemispheres shows different clusters of transcriptional signatures. Louvain clustering reveals 3 transcriptionally distinct clusters. **c**. Feature plots of known mural cell markers identified in all clusters. Data expressed as log-normalized counts. **d**. Feature plots of genes commonly used to identify pericytes. Data expressed as log-normalized counts. **e**. Feature plots of genes encoding for contractile machinery transcribed in venular SMC, albeit at low levels. Data expressed as log-normalized counts. **f**. Feature plot showing minimal transcription of *Myh11*, a marker of vascular SMC. Data expressed as log-normalized counts. **g**. Feature plots of genes commonly used to identify fibroblasts, including *Slc1a3* (GLAST). Data expressed as log-normalized counts. **h**. Hierarchical clustering of all active regulons and their activities across annotated populations. Values shown as z-score of regulon activities.

https://doi.org/10.1038/s41593-025-01872-y

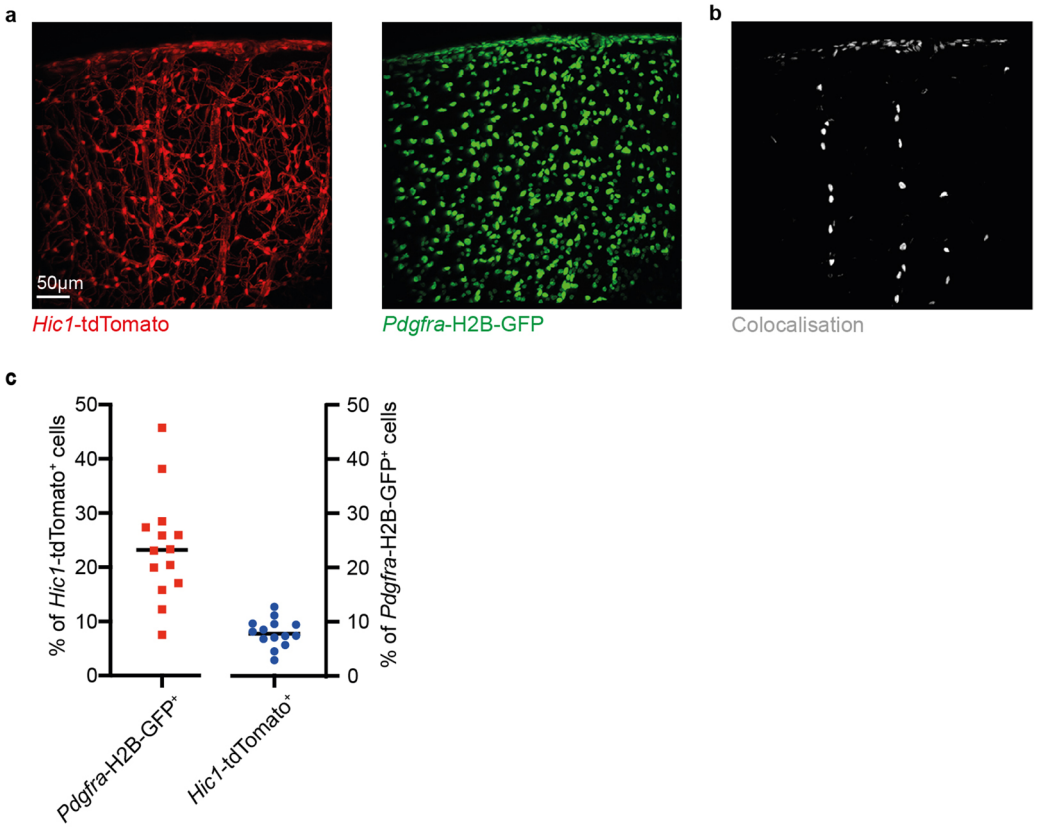

Extended Data Fig. 4 | *Hic1*-tdTomato$^+$ perivascular fibroblasts. a. Maximum projection image of *Hic1*-tdTomato$^+$ cells and *Pdgfra*-H2B-GFP$^+$ cell nuclei image taken from *Hic1*^{CreERT2};*Rosa26*$^{LSL\text{-}tdTomato}$ X *Pdgfra*-H2B-GFP mice. **b**. Colocalization channel created from overlapping signals of *Hic1*-tdTomato$^+$ cells and *Pdgfra*-H2B-GFP$^+$ cells showing perivascular fibroblasts mostly located on penetrating arteriole. **c**. In resting condition, the total number of quantified *Hic1*-tdtomato + /*Pdgfra*-H2B-GFP$^+$ nuclei account for 23.2% of the *Hic1*-tdtomato$^+$ nuclei and 7.6% of the *Pdgfra*-H2B-GFP$^+$ cell population. Black lines represent mean values.

https://doi.org/10.1038/s41593-025-01872-y

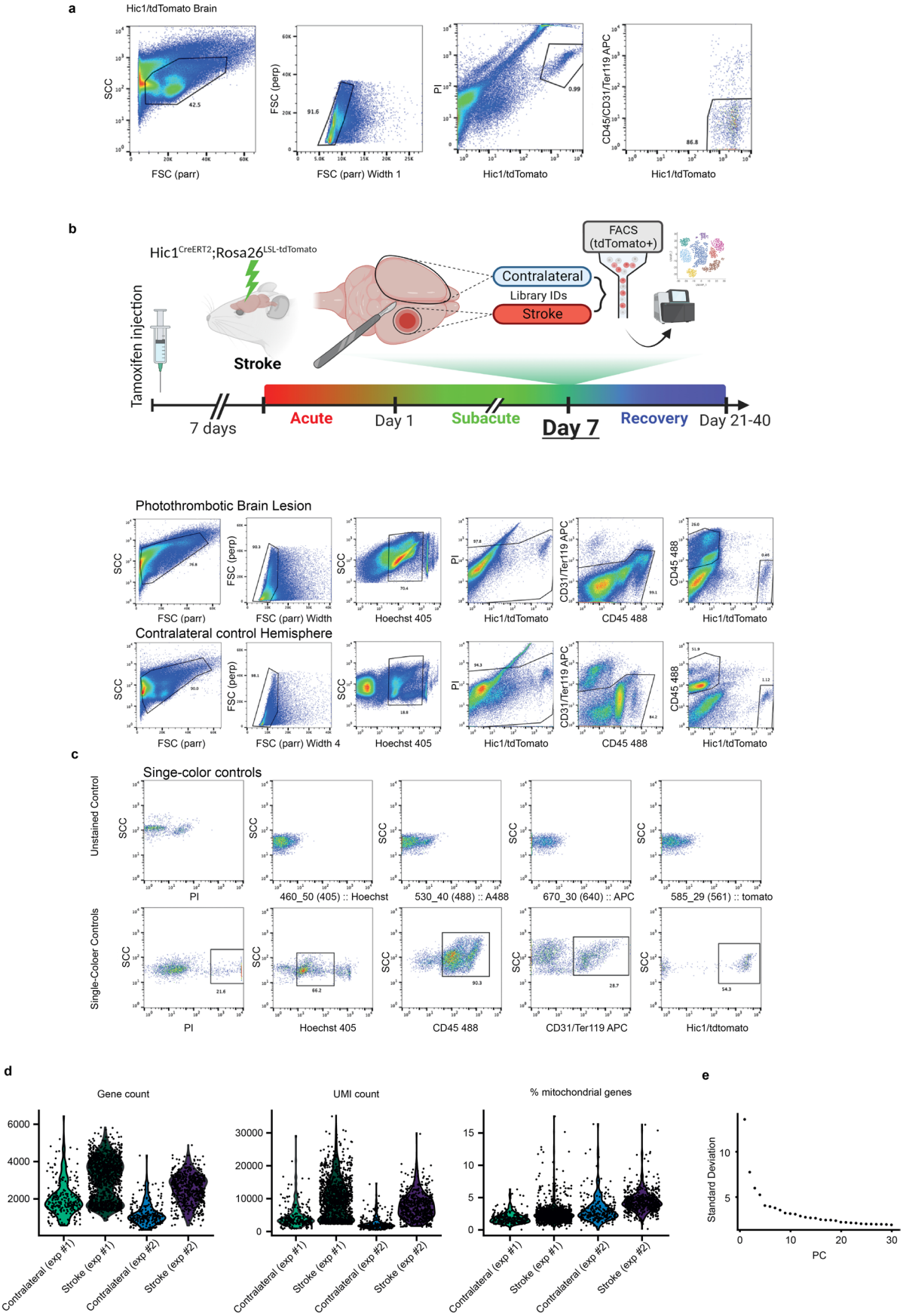

Extended Data Fig. 5 | See next page for caption.

https://doi.org/10.1038/s41593-025-01872-y

Extended Data Fig. 5 | FACS isolation and quality control for RNAseq of *Hic1*-tdTomato$^+$ cells. a. Two *Hic1*^{CreERT2};*Rosa26*$^{LSL\text{-}tdTomato}$ brains (with meninges removed) were digested as described in the methods section and liberated cells pooled for immunolabeling. Following forward scattering light (FSC) and side scattering light (SSC) gating of cells, doublets were excluded and tdTomato$^+$ live cells selected based on the absence of propidium iodide (PI) labelling. CD45 + , CD31 + , and Ter119$^+$ cells were excluded by gating and tdTomato$^+$ cells were isolated for bulk-RNA sequencing. **b.** For single cell RNA sequencing, at day 7 following photothrombotic stroke, *Hic1*^{CreERT2};*Rosa26*$^{LSL\text{-}tdTomato}$ brain tissue was collected from the ischemic lesion area (upper panel) and the contralateral hemisphere (lower panel). Following FSC and SSC gating of cells, doublets were excluded, and cells were further selected on the basis of positive labelling by Hoechst (med) and absent labelling by propidium iodide (PI). Cells negative for the expression of Ter119 and CD31 were separated into CD45 + /tdTomato$^-$ and CD45$^-$/tdTomato$^+$ populations and isolated by FACS. **c**. Single-color controls for all fluorescent markers used during FACS isolation of cells. **d**. Quality control data from single cell RNA-seq, showing distribution of gene counts, UMI counts and % of mitochondrial transcripts per cell across all sample groups. **e**. Scree plot of the first 30 principal components (PC). Downstream Louvain clustering and UMAP were performed with the first 20 PCs.

https://doi.org/10.1038/s41593-025-01872-y

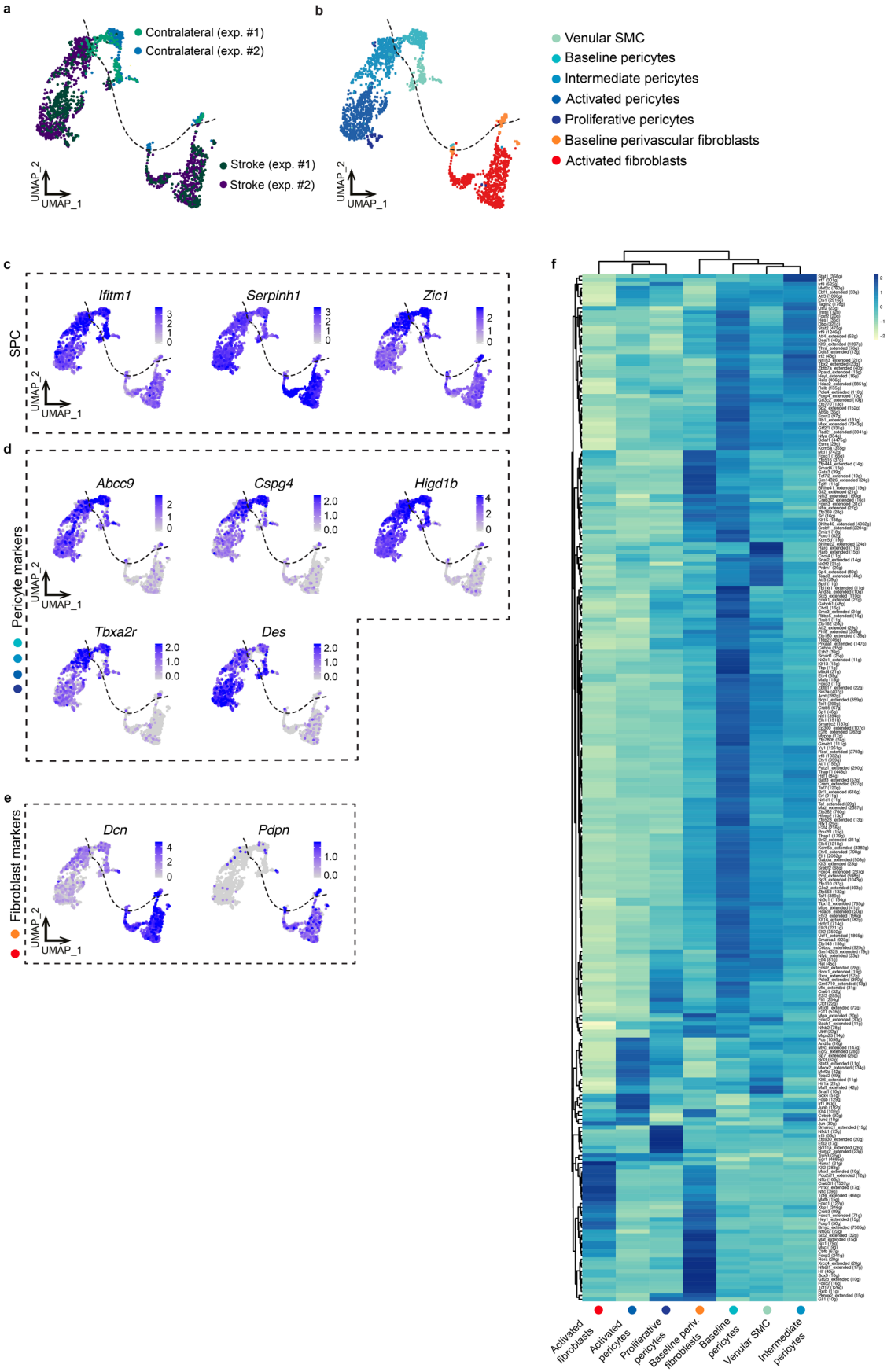

Extended Data Fig. 6 | See next page for caption.

https://doi.org/10.1038/s41593-025-01872-y

Extended Data Fig. 6 | Transcription profiles of quiescent vs stroke-associated *Hic1*-tdTomato$^+$ cells. a. Two individual sets of experiments including individual sample collection from *Hic1*^{CreERT2};*Rosa26*$^{LSL\text{-}tdTomato}$ mice of stroke and contralateral tissue. UMAP plots of merged experiments show similar clustering pattern (colours indicate the individual sequencing experiments). **b**. UMAP plot showing 7 annotated cell identities used for further analysis. **c**. Feature plots of known genes expressed in SPCs. Data expressed as log-normalized counts. **d**. Feature plots of genes commonly used to identify pericytes. Data expressed as log-normalized counts. **e**. Feature plots of genes commonly used to identify fibroblasts. Data expressed as log-normalized counts. **f**. Hierarchical clustering of all active regulons and their activities across annotated populations. Values shown as z-score of regulon activities.

https://doi.org/10.1038/s41593-025-01872-y

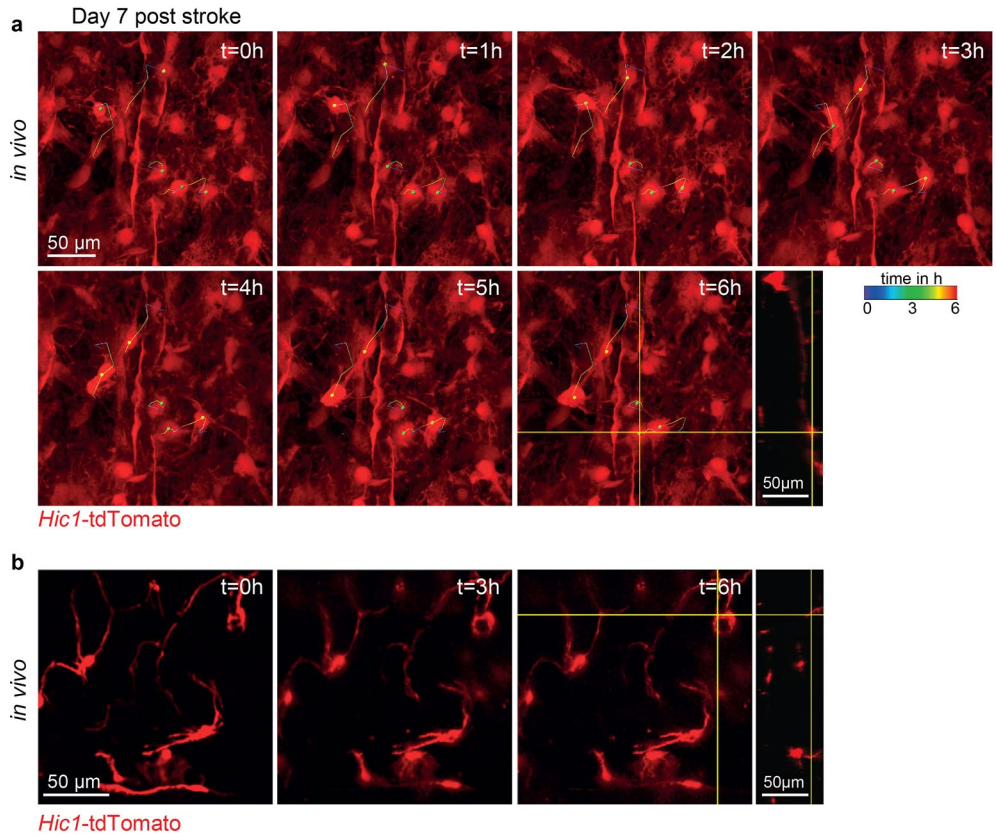

Extended Data Fig. 7 | Active *in vivo* movement of stroke-activated tdTomato$^+$ cell progenies. a. 7 days after the photothrombotic stroke, activated tdTomato$^+$ cell progenies were imaged *in vivo* in *Hic1*^{CreERT2};*Rosa26*$^{LSL\text{-}tdTomato}$ mice through a cranial window to track their movement over 6 h. Each region of interest was imaged at 1-hour intervals. Coloured lines indicate movement of selected individual cells over the entire time course. **b.** tdTomato$^+$ cells imaged in uninjured tissue areas (at least 400 µm away from lesion) displayed typical morphology for cells in a resting state. During the 6-hour time lapse imaging, only minimal movement of resting tdTomato$^+$ cells was detected. Each time point was imaged at 1-hour intervals (hours 0, 3 and 6 shown here).

https://doi.org/10.1038/s41593-025-01872-y

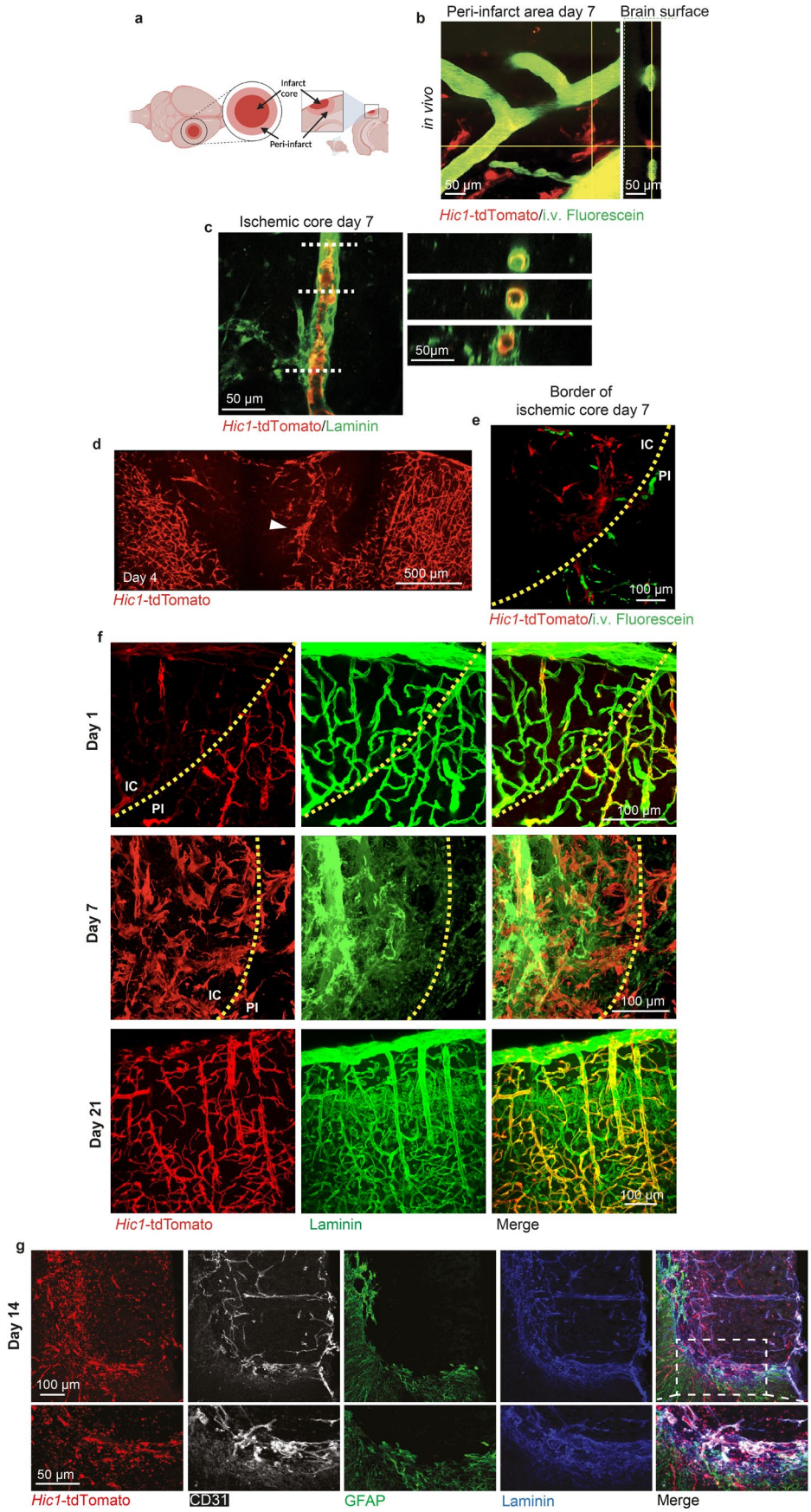

Extended Data Fig. 8 | See next page for caption.

https://doi.org/10.1038/s41593-025-01872-y

Extended Data Fig. 8 | Post stroke association of tdTomato$^+$ cells with ECM component laminin. a. Graphical sketch of peri-infarct area and ischemic core. **b**. Z-stack projections of *in vivo* two-photon images in *Hic1^{CreERT2};Rosa26$^{LSL\text{-}tdTomato}$* mice of tdTomato$^+$ cells along with i.v.-injected 70 kDa dextran-conjugated fluorescein to observe functional blood vessels. At the peri-infarct border, tdTomato$^+$ cells display an activated round morphology and are detached from the microvasculature. **c**. Within the ischemic area, some activated tdTomato$^+$ cells in *Hic1^{CreERT2};Rosa26$^{LSL\text{-}tdTomato}$* mice are located inside the lumen of a vascular tube immunostained for basement membrane component laminin (z-depth on orthogonal view = 50 µm). **d**. Wide-field Axio Zoom image obtained from a coronal slice of a *Hic1^{CreERT2};Rosa26$^{LSL\text{-}tdTomato}$* mouse at day 4 post-stroke showing activated tdTomato$^+$ cells located inside the ischemic area on a large vessel-like structure (arrowhead). **e**. At day 7 within the ischemic core, tdTomato$^+$ cells in *Hic1^{CreERT2};Rosa26$^{LSL\text{-}tdTomato}$* mice are located along a vessel-like structure. Intravenous 70-kDa dextran-conjugated fluorescein was injected to show the absence of functional blood flow in the vessel-like structure on which tdTomato$^+$ cells are observed. (IC: ischemic core; PI: peri-infarct). **f**. Post-stroke timeline of tdTomato$^+$ cells accumulation and recovery in *Hic1^{CreERT2};Rosa26$^{LSL\text{-}tdTomato}$* mice within the ischemic area relative to basement membrane deposition. Initial death of tdTomato$^+$ cells happens prior to basement membrane breakdown (day 1). Basement membrane deposition coincides spatially and temporally with the accumulation of activated tdTomato$^+$ cells within the ischemic area (day 7). In the revascularized area at day 21, normal co-localization of tdTomato$^+$ cells embedded within the basement membrane of vessels is re-established. (IC: ischemic core; PI: peri-infarct). **g**. Immunostainings showing the association between tdTomato$^+$ cells, CD31$^+$ endothelial cells and laminin overproduction at the active angiogenic zone inside the GFAP$^+$ astroglial border 14 days after stroke.

https://doi.org/10.1038/s41593-025-01872-y

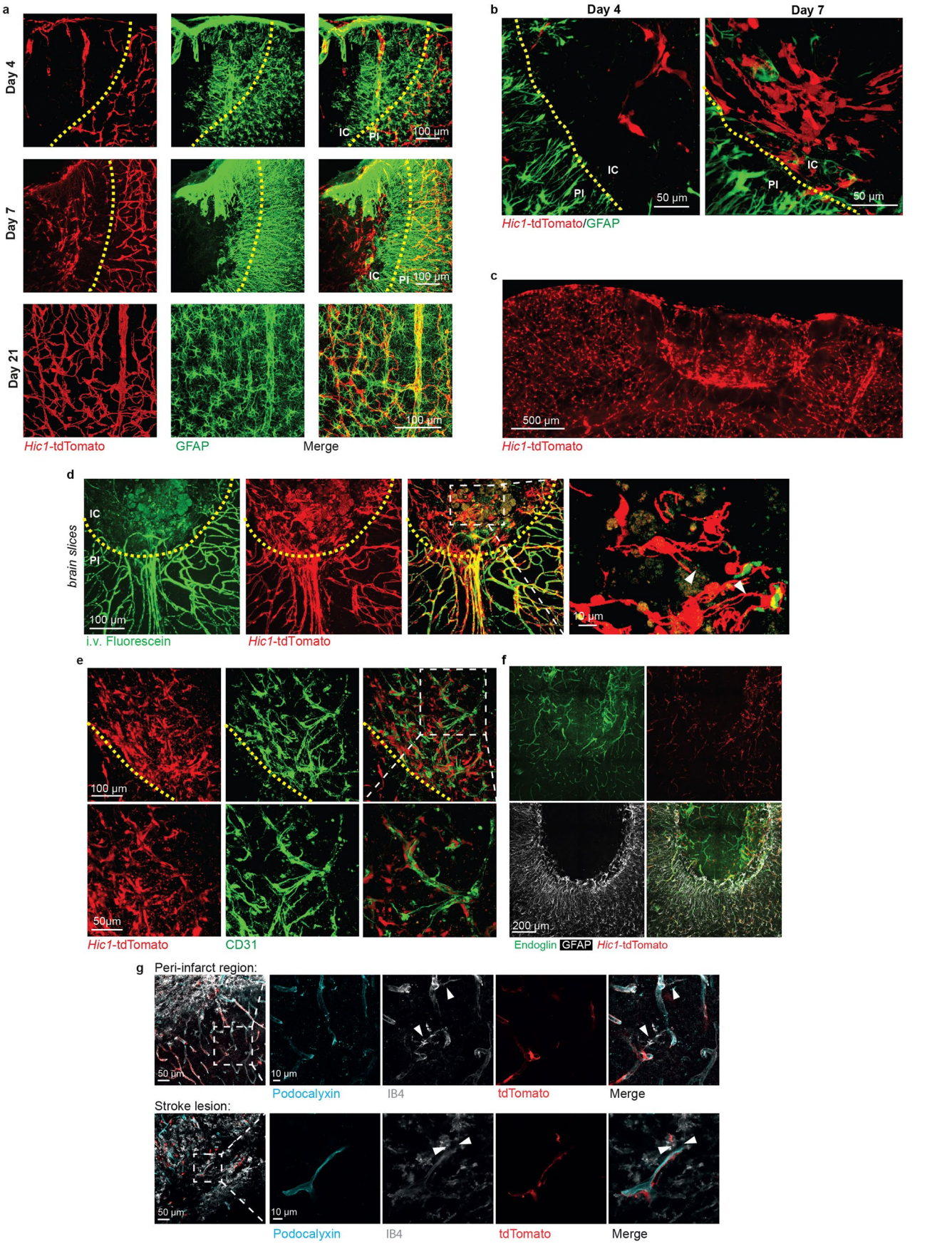

Extended Data Fig. 9 | See next page for caption.

https://doi.org/10.1038/s41593-025-01872-y

Extended Data Fig. 9 | Post-stroke timeline of *Hic1*-tdTomato$^+$ cell accumulation and recovery within the ischemic area relative to astrocytes and endothelial cells. a. At day 4 post-stroke, reactive astrocytes immunostained for GFAP start forming the astroglial border between the vascularized and ischemic regions. At day 7, activated tdTomato$^+$ SPCs accumulate on the inner side of the astroglial border in *Hic1*^{CreERT2};*Rosa26*$^{LSL\text{-}tdTomato}$ mice. In the revascularized area at day 21, normal association between tdTomato$^+$ cells and astrocytes is recovered. **b**. 3D renderings of tdTomato$^+$ cells accumulating on the ischemic side of the astroglial border at days 4 and 7. **c**. Image of activated tdTomato$^+$ cells accumulated within the ischemic area at day 7 post- stroke. **d**. Stroke-activated tdTomato$^+$ cells accumulate near the ischemic border (yellow dashed line, IC: ischemic core; PI: peri-infarct region) in a region devoid of blood flow (i.v. dextran- conjugated fluorescein). Activated tdTomato$^+$ cells show thin-strand ramification morphology (arrowheads) indicative of nascent immature vessels. **e**. 3D rendering showing the close association between tdTomato$^+$ cells and CD31$^+$ endothelial cells at the active angiogenic zone 7 days after stroke. **f**. Immunostainings show the association of stroke-activated tdTomato$^+$ cells with Endoglin$^+$ cells in the angiogenic zone inside the astroglial scar (GFAP). **g**. Immunostainings showing the association between Podocalyxin$^+$ endothelial cells and IB4$^+$ cells, displaying tip-cell like structures in close proximity to tdTomato$^+$ cells, within the stroke lesion and the peri-infarct area 21-days post-stroke.

https://doi.org/10.1038/s41593-025-01872-y

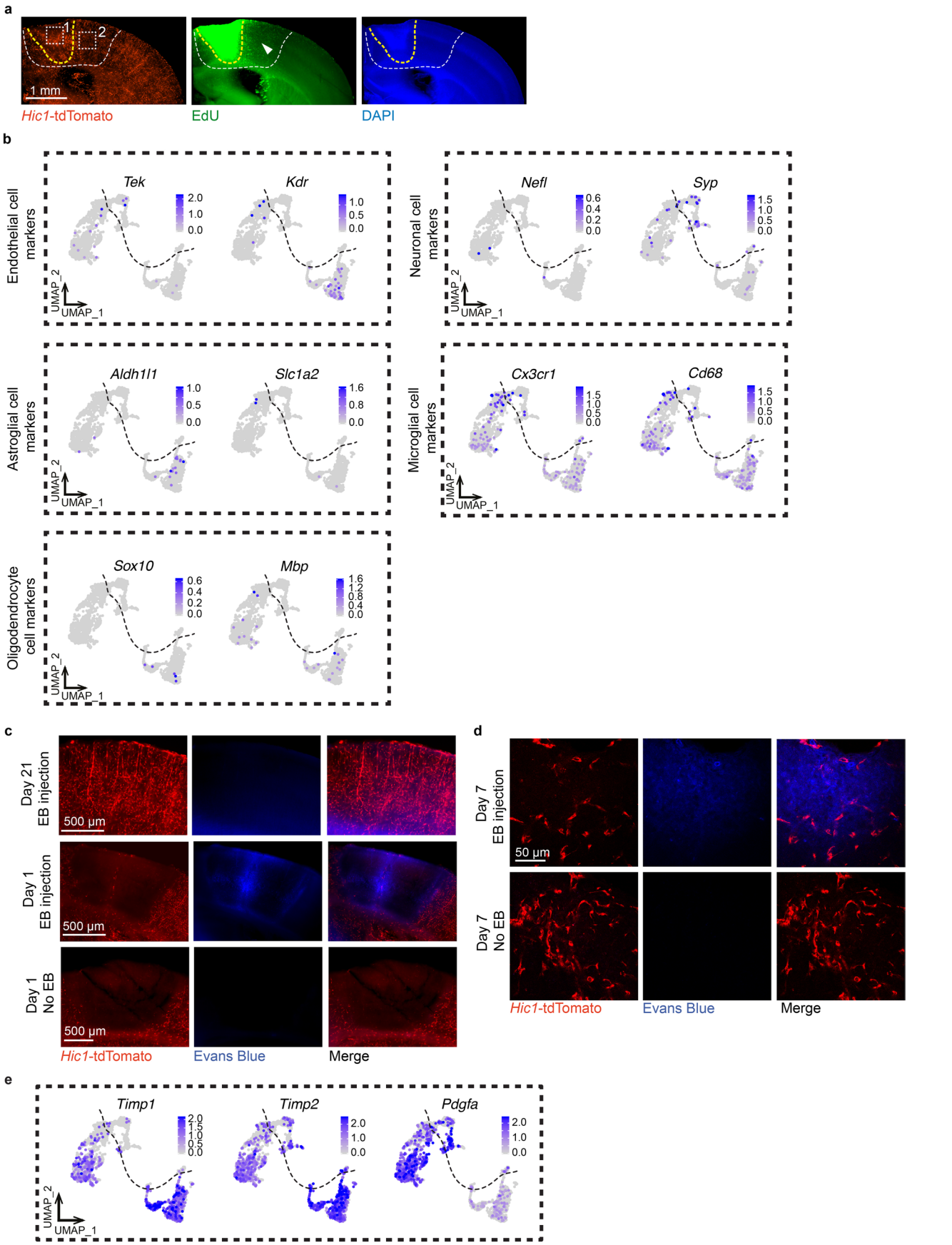

Extended Data Fig. 10 | See next page for caption.

https://doi.org/10.1038/s41593-025-01872-y

Extended Data Fig. 10 | BBB reestablishment and recovery program after photothrombotic stroke. a. EdU incorporation in infarct area and in revascularized cortical area. Images taken from slices collected at day 10 post-stroke from *Hic1*^{CreERT2};*Rosa26*$^{LSL\text{-}tdTomato}$ mice, showing EdU incorporation in cells within the ischemic area, as well as a high proportion of proliferated cells within the revascularized area (arrow). Indicated (white rectangles) are the approximate regions where tdTomato$^+$ cells were evaluated for EdU incorporation (Fig. 5b). **b**. Feature plots of genes commonly used to identify various cell types. The lack of expression in these markers likely indicate that Hic1-traced cells do not differentiate into cell types other than pericytes and fibroblasts. Data expressed as log-normalized counts. **c**. Images taken at indicated days post-stroke show no visible leakage of Evans Blue at day 21 post-stroke in the revascularized area while leakage is observed at day 1 within the infarcted region. To control for possible auto-fluorescence, a similar stroke lesion at day 1 was imaged under the same imaging settings, but without Evans Blue injection (lower panel). **d**. Images 7 days after stroke show Evans Blue leakage within the infarcted area populated with activated tdTomato$^+$ SPCs (upper panel). A similar infarct region was imaged under the same imaging settings but without Evans Blue injection to control for auto-fluorescence from the lesion (lower panel). **e**. Feature plots of genes mentioned in the discussion. Data expressed as log-normalized counts.

nature portfolio

Corresponding author(s): Dr. Brian MacVicar
Dr. Louis-Philipe Bernier

Last updated by author(s): Oct 8, 2024

Reporting Summary

Nature Portfolio wishes to improve the reproducibility of the work that we publish. This form provides structure for consistency and transparency in reporting. For further information on Nature Portfolio policies, see our Editorial Policies and the Editorial Policy Checklist.

Statistics

For all statistical analyses, confirm that the following items are present in the figure legend, table legend, main text, or Methods section.

n/a	Confirmed
☐	☒ The exact sample size (*n*) for each experimental group/condition, given as a discrete number and unit of measurement
☐	☒ A statement on whether measurements were taken from distinct samples or whether the same sample was measured repeatedly
☐	☒ The statistical test(s) used AND whether they are one- or two-sided *Only common tests should be described solely by name; describe more complex techniques in the Methods section.*
☒	☐ A description of all covariates tested
☒	☐ A description of any assumptions or corrections, such as tests of normality and adjustment for multiple comparisons
☐	☒ A full description of the statistical parameters including central tendency (e.g. means) or other basic estimates (e.g. regression coefficient) AND variation (e.g. standard deviation) or associated estimates of uncertainty (e.g. confidence intervals)
☐	☒ For null hypothesis testing, the test statistic (e.g. *F*, *t*, *r*) with confidence intervals, effect sizes, degrees of freedom and *P* value noted *Give P values as exact values whenever suitable.*
☒	☐ For Bayesian analysis, information on the choice of priors and Markov chain Monte Carlo settings
☒	☐ For hierarchical and complex designs, identification of the appropriate level for tests and full reporting of outcomes
☒	☐ Estimates of effect sizes (e.g. Cohen's *d*, Pearson's *r*), indicating how they were calculated

Our web collection on statistics for biologists contains articles on many of the points above.

Software and code

Policy information about availability of computer code

Data collection

Data was collected with the following programs:
Zeiss Zen 2 imaging software
ScanImage Version 3.8
ThorImage OCT imaging software
10xGenomics software
LAS X Version 3.5.7.23225
Fiji 2.14.01/1.54f
Imaris 9.2
FlowJo
SCENIC
FACS software

Data analysis

Maximum projections of tile Z stacks were analyzed using Fiji software (ImageJ).
Surface detection algorithm, colocalization and tracking were performed and analyzed in Imaris 9.2 (Bitplane, Oxford Instruments). Statistical analysis was performed with Prism 9.3.0 software (Graphpad). The “surface to surface contact area” tool embedded in the Matlab extension of Imaris was used to quantify somata associated to vessel structures. VE-Cadherin junctions were analyzed using Fiji software. Cadaverine leakage was analyzed using Fiji software. Mean signal intensity was measured outside of vessels (stained with anti-podocalyxin). A transgenic reference genome was generated by the concatenation of the sequences for tdTomato to the mm10 reference genome and subsequent use of the cellranger mkref pipeline. Alignment to the modified mm10 reference genome was performed using the cellranger count pipeline (10X Genomics). The cellranger aggr pipeline was used to create aggregated library. Graphical output was generated using the cellrangerRkit R

package (10X Genomics). All datasets were processed and analyzed using the Seurat package (Satija Lab, version 3.1.2) in R.

For manuscripts utilizing custom algorithms or software that are central to the research but not yet described in published literature, software must be made available to editors and reviewers. We strongly encourage code deposition in a community repository (e.g. GitHub). See the Nature Portfolio guidelines for submitting code & software for further information.

Data

Policy information about availability of data

All manuscripts must include a data availability statement. This statement should provide the following information, where applicable:

- Accession codes, unique identifiers, or web links for publicly available datasets
- A description of any restrictions on data availability
- For clinical datasets or third party data, please ensure that the statement adheres to our policy

The complete sequencing data report included in this paper was deposited to NCBI SRA (GEO GSE146930; BioProject accession number PRJNA608615). All raw and processed data bill be made available upon request.

Field-specific reporting

Please select the one below that is the best fit for your research. If you are not sure, read the appropriate sections before making your selection.

☒ Life sciences ☐ Behavioural & social sciences ☐ Ecological, evolutionary & environmental sciences

For a reference copy of the document with all sections, see nature.com/documents/nr-reporting-summary-flat.pdf

Life sciences study design

All studies must disclose on these points even when the disclosure is negative.

Sample size	Multiple mice were observed and analyzed as biological replicates. Animals (both male and female) were then used in different settings at these time points: For in vivo two-photon imaging n = 5 animals were used for each time point. For in vivo tracing of cells over 6 hours n = 5 animals are used, displayed datapoints represent individual cells. For TTC imaging n = 4 animals were used 24 hours after photothrombosis. For optical coherence tomography n = 8 mice were used longitudinally throughout the recovery process to assess lesion circumference over time and each was imaged prior to photothrombosis, immediately after and at days 1, 4, 7, 10, 14, 21. For immunohistochemistry n = 5 animals were used for each time point. For colocalization analysis with PDGFRb and Hic1-tdTomato n = 3 animals were used. For analysis of SPCs at different time points before and after stroke n = 8-10 animals were used for each time point. For fluorescein injection n = 4 animals were used for each time point (Day 1, 7, 21 post stroke). For Evans Blue injection n = 4 animals were used for each time point (Day 1, 7, 21 post stroke). For the quantification of VE-Cadherin activity n= 3 animals were used. For the quantification of Cadaverine leakage n = 3 animals were used. For acute slice preparation experiments n = 3 mice. For EdU incorporation experiments n = 5 mice were used for each time point (Day 7, 10 post stroke). For SPC deletion experiments using Hic1CreERT2;Rosa26DTA mice n = 5 were used. For FITC-conjugated gelatin injection n = 5 were used. For quantification analysis and localization of Hic1-tdTomato+/Pdgfra-H2B-GFP+ cells in comparison to Hic1-tdTomato+/Pdgfra-H2B-GFP- cells n = 3 of Hic1CreERT2;Rosa26LSL-tdTomato X Pdgfratm11(EGFP)Sor/J was used in baseline conditions. At day 7 post stroke n = 3 were used. For image acquisition of all Pdgfra+ cells post stroke PdgfraCreERT2;Rosa26LSL-tdTomato were used n = 4 mice. To investigate Hic1-expressing cells in the brain Hic1nLacZ/+ were used n = 5 mice. Graphs were compiled in Graphpad Prism 8 or R and show mean ± SEM unless indicated otherwise. For population sequencing n = 4 animals were used. For single cell RNA sequencing using contralateral tissue and tissue from the ischemic core n = 8-10 animals were used. The number of animals used in each group was carefully selected to ensure that we could reliably and repeatedly observe the described effects, while adhering to the 3Rs (Replacement, Reduction, Refinement) philosophy. This approach allowed us to balance the need for scientific rigor with our ethical commitment to minimizing the number of animals used in our research
Data exclusions	No data was excluded from the study.
Replication	All representative experiments shown were repeated with similar results in at least 3 independent experiments. All attempts of replication were successful and gave similar results.
Randomization	Mice were randomly assigned into the stroke of control groups. Brain sections within these groups used for imaging were selected randomly, however they were limited by the number of sections that contained the stroke in the case of images displaying different time points after experimental stroke.
Blinding	The VE-Cadherin images were sectioned into 100x256 pixels patches, which were then randomized and presented for blinded classification. All obtained images are stored within one database. Subsequently, they are presented for blinded classification in a randomized manner. For other experiments blinding was not possible as experimental conditions were evident from the imaged data. Quantifications were performed using pipelines and algorithms equally to all conditions and replications.

Reporting for specific materials, systems and methods

We require information from authors about some types of materials, experimental systems and methods used in many studies. Here, indicate whether each material, system or method listed is relevant to your study. If you are not sure if a list item applies to your research, read the appropriate section before selecting a response.

Materials & experimental systems

n/a	Involved in the study
☐	☒ Antibodies
☒	☐ Eukaryotic cell lines
☒	☐ Palaeontology and archaeology
☐	☒ Animals and other organisms
☒	☐ Human research participants
☒	☐ Clinical data
☒	☐ Dual use research of concern

Methods

n/a	Involved in the study
☒	☐ ChIP-seq
☐	☒ Flow cytometry
☒	☐ MRI-based neuroimaging

Antibodies

Antibodies used

rabbit anti-Laminin (1:100), Abcam 11575
rabbit anti-Collagen IV (1:500), Biodesign T40251R,
rabbit anti-NG2 (1:500), ThermoFisher PA5-17199
rat anti-CD105 (endoglin), 1:1000, ThermoFisher 14-1051-82,
goat anti-podocalyxin, 1:500, R&D Systems AF1556,
goat anti-PDGFRβ, 1:500, Neuromics GT15065,
rabbit anti-GFAP, 1:1000, Dako Z 0334
CD31 (rat, 1:50), BD Pharmingen 557355
VE-Cadherin (rat, 1:50),BD Pharmingen 555289
1 kDA Alexa Fluor™ 555 Cadaverine (Invitrogen A30677)
anit-CD31-APC (BD Pharmingen 551262, 1:400)
anti-Ter119-647d (Ablab AB00000305, 1:200)
anti- CD45-488 (AbLab AB00000383, 1:1000)

donkey anti-rabbit 488, 1:1000, ThermoFisher A21206
donkey anti-rat 488, 1:1000, ThermoFisher A21208,
donkey anti-goat 488, 1:1000, ThermoFisher A11055,
donkey anti-rabbit 647, 1:1000, ThermoFisher A31573
donkey anti-goat 647, 1:1000, ThermoFisher A21447
Goat anti-rabbit Alexa 488 (1:500), ThermoFisher A11034
Goat anti-rat Alexa 488 (1:500), ThermoFisher A-11006
Goat anti-rabbit Alexa 405 (1:500), Invitrogen A-31556
Goat anti-chicken Alexa 488 (1:500), Invitrogen A-11039
Goat anti-rabbit Alexa 647 (1:500), Invitrogen A-32733

Validation

Listed antibodies have been validated by the respective company and can be found on their webpages. Anti-Laminin, Suitable for Dot, IHC-P and reacts with Mouse, Human samples (https://www.abcam.com/en-us/products/primary-antibodies/laminin-antibody-ab11575#). Rabbit anti-NG2, this polyclonal antibody has been validated for Western blot (WB), Immunohistochemistry (IHC-P), and Immunocytochemistry (ICC/IF) in human, mouse, and rat samples.(https://www.thermofisher.com/antibody/product/NG2-Antibody-Polyclonal/PA5-97638). Rat anti-CD45 has been validated for WB, IHC-P, and ICC/IF in rat, mouse (https://www.thermofisher.com/order/genome-database/dataSheetPdf?producttype=antibody&productsubtype=antibody_primary&productId=14-1051-82&version=Local). Goat anti-podocalyxin has been validated for WB, IHC-P, and Flow Cytometry (https://www.rndsystems.com/products/mouse-podocalyxin-antibody_af1556). Goat anti-PDGFRβ has been validated in the following paper DOI: 10.1126/science.aao2861. CD31 has been validated for flow cytometry (https://www.bdbiosciences.com/en-eu/products/reagents/flow-cytometry-reagents/research-reagents/single-color-antibodies-ruo/purified-rat-anti-mouse-cd31.557355). VE-Cadherin has been validated for flow cytometry (https://www.bdbiosciences.com/en-us/products/reagents/functional-cell-based-reagents/purified-rat-anti-mouse-cd144.555289). Alexa Fluor™ 555 Cadaverine, this fluorescent conjugate is validated for use in microscopy and other fluorescent labeling techniques (https://www.thermofisher.com/order/catalog/product/A30677). Anti-CD31-APC has been validated for flow cytometry (https://www.bdbiosciences.com/en-ca/products/reagents/flow-cytometry-reagents/research-reagents/single-color-antibodies-ruo/apc-rat-anti-mouse-cd31.551262). Anti-Ter119-647d and Anti-CD45-488 have been validated for flow cytometry (https://ablab.ca/). The secondary antibodies from ThermoFisher (donkey anti-rabbit 488, 1:1000, donkey anti-rat 488, 1:1000, donkey anti-goat 488, 1:1000, donkey anti-rabbit 647, 1:1000, donkey anti-goat 647, 1:1000, Goat anti-rabbit Alexa 488, 1:500, Goat anti-rat Alexa 488 1:500) are validated for various applications such as immunofluorescence (IF), immunohistochemistry (IHC), and flow cytometry (FC). They are conjugated to Alexa Fluor dyes (either 488, 405 or 647), which provide bright, stable fluorescence suitable for multiple imaging techniques.
Validationsheets for the secondary antibodies listed in the order of the text can be found here:
https://www.thermofisher.com/order/genome-database/dataSheetPdf?producttype=antibody&productsubtype=antibody_secondary&productId=A-21206&version=Local
https://www.thermofisher.com/order/genome-database/dataSheetPdf?producttype=antibody&productsubtype=antibody_secondary&productId=A-21208&version=Local
https://www.thermofisher.com/order/genome-database/dataSheetPdf?producttype=antibody&productsubtype=antibody_secondary&productId=A-11055&version=Local
https://www.thermofisher.com/order/genome-database/dataSheetPdf?producttype=antibody&productsubtype=antibody_secondary&productId=A-31573&version=Local
https://www.thermofisher.com/order/genome-database/dataSheetPdf?producttype=antibody&productsubtype=antibody_secondary&productId=A-21447&version=Local

The secondary antibodies from Invitrogen (Goat anti-rabbit Alexa 405, 1:500, Goat anti-chicken Alexa 488, 1:500, Invitrogen A-11039 Goat anti-rabbit Alexa 647, 1:500) are validated for use in various fluorescence-based applications, including immunocytochemistry (ICC/IF), immunohistochemistry (IHC), and flow cytometry. Each antibody is conjugated to Alexa Fluor dyes, known for their bright, photostable fluorescence and minimal background. These antibodies are cross-adsorbed to reduce cross-reactivity, ensuring high specificity in multicolor labeling experiments. Validationsheets for the secondary antibodies listed in the order of the text can be found here:
https://www.thermofisher.com/order/genome-database/dataSheetPdf?producttype=antibody&productsubtype=antibody_secondary&productId=A48254&version=Local
https://www.thermofisher.com/order/genome-database/dataSheetPdf?producttype=antibody&productsubtype=antibody_secondary&productId=A-11039&version=Local
https://www.thermofisher.com/order/genome-database/dataSheetPdf?producttype=antibody&productsubtype=antibody_secondary&productId=A32733&version=Local

Animals and other organisms

Policy information about studies involving animals; ARRIVE guidelines recommended for reporting animal research

Laboratory animals	All mouse lines were maintained on a C57BL/6J background. Male and female mice at the age of 2-5 months were used. Hic1CreERT2;Rosa26DTA, Hic1CreERT2;Rosa26LSL-tdTomato, Hic1CreERT2;Rosa26LSL-tdTomato;Pdgfra-H2B-GFP, Hic1nLacZ/+ were used at day 1, 4, 7, 8, 14, 21 or 40 post stroke.
Wild animals	No wild animals were used in this study.
Field-collected samples	No field-collected samples were used in this study.
Ethics oversight	All experimental procedures were performed in accordance with Canadian Council on Animal Care (CCAC) regulations, German veterinary office regulations (for the state of Hessen) and approved by the local authorities for animal experimentation (Regierungspräsidium Darmstadt, Germany), with protocols approved by the University of British Columbia committee on animal care.

Note that full information on the approval of the study protocol must also be provided in the manuscript.

Flow Cytometry

Plots

Confirm that:

☒ The axis labels state the marker and fluorochrome used (e.g. CD4-FITC).

☒ The axis scales are clearly visible. Include numbers along axes only for bottom left plot of group (a 'group' is an analysis of identical markers).

☒ All plots are contour plots with outliers or pseudocolor plots.

☒ A numerical value for number of cells or percentage (with statistics) is provided.

Methodology

Sample preparation	Brains from Hic1CreERT2;Rosa26LSL-tdTomato mice were dissected and immediately sliced into 800-µm thick coronal slices using a Vibratome (Leica VT1200S) as described above to improve visualization of the ischemic area. The ischemic area was dissected from four mice and pooled for FACS-sorting. Contralateral hemispheres from four mice were also pooled separately. A razor was used to cut the brain tissue into <1 mm3 pieces. 1.5 ml digestion buffer was added containing 1.5 U/mL Collagenase D (Roche 11 088 882 001) and 2.4 U/mL Dispase II (Roche 04 942 078 001) for 40 minutes. Digested material was subsequently triturated by pipetting and centrifuged 2200 rpm for 5 minutes. Re-suspended tissue (6 ml PBS) was again triturated by pipetting and passed through a 70 µm cell strainer. Tissue was re-suspended in 37% Percoll and centrifuged at 2200 rpm for 20 minutes at room temperature. The separated myelin and Percoll were removed followed by 5 minutes of centrifugation at 1400 rpm. To enrich for tdTomato cells from this whole brain suspension, cells were stained with a cocktail containing anti-Ter119-647d (Ablab AB00000305, 1:200), anti- CD45-488 (AbLab AB00000383, 1:1000) and anti-CD31-APC (BD Pharmingen 551262, 1:400). This mixture containing cells and antibodies was then incubated on ice for 20 minutes (in the dark). Afterwards, 3 ml FACS buffer was added to dilute the antibodies prior to centrifugation at 1400 rpm for 5 minutes. Cells were re-suspended in FACS buffer and centrifuged at 1400 rpm for 5 minutes. The pellet was re-suspended in FACS buffer containing propidium iodide (PI) and Hoechst 33342 (Sigma B2261) to a final concentration of 4 µM. Positively stained cells were then sorted using a BD Influx, and PI-negative, Hoechst positive, and forward/side scatter parameters were used to identify viable single cells for all FACS enrichments. Sorted cells were collected into sort media (DMEM, 5% FBS) in cooled siliconized microcentrifuge tubes (Fisher Scientific; 02-681-320). For isolation of RNA, cells were microfuged at 2500 rpm for 5 minutes with soft braking and the isolated cell pellet was lysed in RNAzol (Sigma R4533).
Instrument	BD Influx
Software	The software used to operated the FACS machine and sort cells was BD FACS(TM) Software. Data was analyzed using FlowJo version 10.1.
Cell population abundance	For the bulk RNA sequencing of Hic1/td.Tomato+ cells from brain, a sample of sorted cells was run on the flow cytometer to examine purity. The post-sort sample consisted of 98% Hic1/tdTomato+ cells.

For the single-cell RNA sequencing experiment, Hic1/tdTomato+ cells were sorted twice and positively identified as tdTomato + through single-cell RNA sequencing.

Gating strategy

For the bulk sort of Hic1/tdTomato+ cells from brain, cells were gated by FSC/SSC. Selected cells were gated by FSC(parr)Width1 x FSC(perr) to gate our doublets. From the gated singlet population, viable (PI-negative) Hic1/tdTomato+ cells were gated and partitioned into CD45/CD31/Ter119-negative and positive subsets. The CD45/CD31/Ter119-negative subset was isolated for downstream RNA sequencing.

For the single-cell analysis of Hic1/tdTomato+ cells from photothrombotic stroke and contalateral brain hemisphere regions, cells were gated by FSC/SSC. Doublets were excluded on the basis of FSC(parr)Width4 x FSC(perr). Nucleated (Hoechst-mid) cells were selected and from this population, viable (PI-negative) Hic1/tdTomato+ cells were selected. CD31/Ter119+ cells were excluded from this population and cells were then separated into CD45+Hic1/tdTomato- and CD45-Hic1/tdTomato+ cells populations. Each population of cells was collected and used for downstream single-cell RNA sequencing.

☒ Tick this box to confirm that a figure exemplifying the gating strategy is provided in the Supplementary Information.